Atomic Transitions and Population Control by Laser Frequency Scanning Speed and Magnetic Field

Artur Aleksanyan

UNIVERSITÉ BOURGOGNE FRANCHE-COMTÉ
Laboratoire Interdisciplinaire Carnot de Bourgogne – UMR CNRS 6303

NATIONAL ACADEMY OF SCIENCES OF ARMENIA
Institute for Physical Research

ATOMIC TRANSITIONS AND POPULATION CONTROL BY LASER FREQUENCY SCANNING SPEED AND MAGNETIC FIELD

by

Artur ALEKSANYAN

A Thesis in Physics
Submitted for the Degree of Doctor of Philosophy

Date of defense: 13 September 2022

Jury

Mrs Elena BEKHTEREVA	Professor Tomsk, LMS – TPU	Examiner – President of Jury
Mr Atom MURADYAN	Professor Yerevan, YSU	Referee
Mrs Olga GROMOVA	Assoc. Professor Tomsk, LMS – TPU	Referee
Mr Claude LEROY	Professor Dijon, ICB – UBFC	Supervisor
Mr Emil GAZAZYAN	Doctor of Physics Ashtarak, IPR – NAS	Supervisor

Laboratoire Interdisciplinaire Carnot de Bourgogne – UMR CNRS 6303, Université Bourgogne Franche-Comté, 9 Avenue A. Savary 21078 Dijon, France

Institute for Physical Research – National Academy of Sciences of Armenia, 0203 Ashtarak-2, Armenia

Abstract

Atomic Transitions and Population Control by Laser Frequency Scanning Speed and Magnetic Field

In this thesis the influence of laser radiation and external uniform magnetic field on alkali-metal atomic vapor is studied. We focused on three topics. In the first part, we examined atomic population control in an M-type system to demonstrate that such systems can serve as universal three-bit logical devices. The second part concerns an experiment of atomic spectroscopy. From the fluorescence spectra recorded for stationary, transient and non-stationary interaction regimes, we were able to extract important parameter values which are the relaxation rate of the lower energy levels to the equilibrium isotropic state, the diffusion coefficient in a buffered vapor cell, and the corresponding collisional cross section. In addition, optimal temporal conditions are obtained to provide efficient control of the atomic population. In the last chapter, an interesting application of a magnetic field interacting with alkali-metal atoms is presented. Theoretically and numerically, the transitions between magnetic sublevels of alkaline atoms in the Zeeman and Paschen-Back regimes are examined. We obtained magnetic-field values canceling transitions which only depend on the fundamental physical and atomic constants. These values in the case of an appropriate experimental determination can serve as standards of magnetometry.

Résumé

Transitions Atomiques et Contrôle de la Population par Fréquence de Balayage Laser et Champ Magnétique

Dans cette thèse, l'influence du rayonnement laser et du champ magnétique externe uniforme sur la vapeur atomique de métal alcalin est étudiée. Nous nous sommes concentrés sur trois sujets. Dans la première partie, nous avons examiné le contrôle de la population atomique dans un système de type M pour démontrer que de tels systèmes peuvent servir de dispositifs logiques universels à trois bits. La deuxième partie concerne une expérience de spectroscopie atomique. A partir des spectres de fluorescence enregistrés pour les régimes d'interaction stationnaires, transitoires et non stationnaires, nous avons pu extraire des valeurs de paramètres importantes qui sont le taux de relaxation des niveaux d'énergie inférieurs à l'état isotrope d'équilibre, le coefficient de diffusion dans une cellule avec gaz tampon, et la section efficace de collision correspondante. De plus, des conditions temporelles optimales sont obtenues pour fournir un contrôle efficace de la population atomique. Dans le dernier chapitre, une application intéressante d'un champ magnétique interagissant avec des atomes de métaux alcalins est présentée. Théoriquement et numériquement, les transitions entre les sous-niveaux magnétiques des atomes alcalins dans les régimes Zeeman et Paschen-Back sont examinées. Nous avons obtenu des valeurs de champ magnétique annulant les transitions qui ne dépendent que des constantes physiques et atomiques fondamentales. Ces valeurs dans le cas d'une détermination expérimentale appropriée peuvent servir d'étalons de magnétométrie.

Contents

List of Figures

List of Tables

List of Abbreviations

CCNOT	controlled controlled NOT	19
CSWAP	controlled SWAP	19
STIRAP	stimulated Raman adiabatic passage	20
b-STIRAP	bright-state stimulated Raman adiabatic passage	20
RAP	rapid adiabatic passage	28
TOF	time of flight	43
SA	saturated absorption	54
dSR	derivative of selective reflection	58
SO	spin-orbit	59
SR	selective reflection	78
SNR	signal-to-noise ratio	88

Chapter 1

Introduction

1.1 Description of the thesis

This thesis is devoted to physical systems where quantum physics is the necessary theoretical formalism needed to be used: atomic systems. Today, lasers are not only applied to investigate quantum (atomic) systems, but also to manipulate and steer properties and processes in these media. In past decades, the most intense studied processes on alkali atoms are Faraday effect [1, 2] (the rotation of the plane of polarization of light), Hanle effect [3–5] (reduction in the polarization of light), Dicke effect [6, 7] (narrowing of spectral lines in dense alkali vapor), increase of the resonance interaction time in a buffered vapor cell [8–10], magneto-optical processes [11–13], atomic beam splitting [14–16], etc. Except of these effects and processes, the research of resonance interaction [17] opened a way for the construction of lasers based on alkali vapors [18, 19], for a development of very precise and wide-range optical magnetometers [13, 20–23], and also brought a huge contribution in quantum informatics, for instance the construction of optical quantum memory devices [24, 25], logical gates [26, 27], etc. Today, in addition to classical (mm- or cm-size) atomic vapor cells, the study of effects raised in a nanocell [28–30] is very interesting and important because it allows us to use sub-Doppler resolution in the investigation of the phenomena and processes.

Atomic systems become very complicate objects to study as soon as one wants to enter into the hyperfine structure of the atoms. Moreover, the Schrödinger equation is not enough sufficient to examine with a high degree of precision the interaction of this hyperfine structure with external fields as for instance magnetic and electric fields responsible of the Zeeman, Paschen-Back and Stark effects. The high precision of the measurements in the last decades implies to implement sophisticated mathematical and physical tools as Liouville equation, von Neumann formalism, Dirac equation, etc., within more and more powerful computers in order to perform numerical simulations as precise as the measurements.

The first part of this thesis deals with transfer of populations. This part is at the interface of physics and computer sciences. Briefly summarized, the issue could be shortened as: “How much, how far can we replace material components of a computer by optical devices?”. More precisely in this part of the thesis we want to demonstrate that atoms and population

transfer between hyperfine levels of these atoms are equivalent to logical devices. In order to have calculable and solvable equations, based on the density matrix theory, the atoms used to modeling a possible implementation of these full atomic logical devices are the ones of the first column of the atomic table due to hydrogen-like electronic structure.

The second part of the thesis relates more directly to real experiments on these alkaline atoms. The fluorescence spectra have been obtained and analyzed in a dynamic transient process. Among many information, data, measures that can be extracted from these experiments, it worth to notice the followings: determination of relaxation rates, how to control population in these atomic systems, measure of the populations of the excited atomic states. As the most satisfactory result of our experiments would be to have an efficient atomic population control, the main goal of this chapter is to determine as precise as possible the most optimal temporal conditions for that.

The last chapter introduces and develops a very interesting application of a magnetic field interacting with these alkali atoms. Indeed, by studying atomic M-system in the first chapter we understood that the Zeeman splitting is an easy way to obtain M-like systems. By varying the intensity of the magnetic field we have seen a variation of the transition probability when lighting these alkali atoms with a polarized laser field. Intriguingly, we observed theoretically complete annihilation of some transitions for very precise values of the magnetic field. Thus we have wanted to know more about the theoretical description of this phenomenon and indeed we have been able in the case of $n\ ^2S_{1/2} \rightarrow k\ ^2P_{1/2}$ transitions to obtain formulas giving the values of these particular B-fields and furthermore in more complicated cases, all the values of B-field have been exactly determined by numerical simulation. This allows us to envisage the reciprocal effect annihilation of a transition for a very precise value of the B-field means this value can be used as a standard for the calibration of a magnetometer.

The main objectives of the thesis

- To investigate a mechanism of complete population transfer in five level M-type system without each transition exact resonances and to propose realistic schemes of Toffoli and Fredkin gate implementation on five level atomic system.
- To develop a theoretical model and experimentally record the spectra in a transient regime of ^{87}Rb and ^{85}Rb atomic vapor fluorescence, and from the theoretical simulation to be able to determine fitting parameters, such as the relaxation rate and the diffusion coefficient.
- To solve all types (π, σ^+ and σ^-) of modified transfer coefficients which have a cancellation. For $n\ ^2S_{1/2} \rightarrow k\ ^2P_{1/2}$ transitions to solve analytically and for more complicated cases (i.e. for rubidium 87 and 85 isotopes $5\ ^2S_{1/2} \rightarrow 5\ ^2P_{3/2}$ and $5\ ^2S_{1/2} \rightarrow 6\ ^2P_{3/2}$ transitions) to solve numerically. Furthermore, to propose realistic experiment to determine hyperfine transition cancellations, where the obtained values can be used to calibrate wide-range magnetometers and improve the involved quantities' accuracy.

The main statements of the thesis

- Full population transfer in five level M-type atomic system using laser frequency scanning methods or various laser pulse sequences.
- Realization of Toffoli and Fredkin universal reversible atomic gates on alkali-metal vapor.
- Rubidium vapor fluorescence spectra in a transient regime caused by laser frequency scanning at various scanning speeds.
- A new method to determine rubidium vapor ground state relaxation rate, the diffusion coefficient and respective collisional cross section of a buffered cylindrical cell.
- Magnetic-field values for which dipole allowed transitions intensity between magnetic sublevels becomes zero. These values can serve to decrease the uncertainty of involved physical quantities and as standards to calibrate magnetometers.

Scientific novelty and practical importance

- In this thesis a method to make a complete population transfer is proposed without the exact resonances of the atomic transitions. A possible scheme to implement reversible atomic Toffoli and Fredkin gates is proposed. The considered method and atomic gate implementation can be realized using the electronic terms and magnetic sublevels of an alkali atom and can lead to the experimental development of atomic logical devices and to the mentioned above atomic gates for quantum processors.
- Method of determination of the ground state relaxation rate to the equilibrium isotropic state, the diffusion coefficient in a buffered vapor cell, and the corresponding collisional cross section is proposed based on the consideration of the atomic vapor fluorescence spectra in a non-stationary regime. Also it is possible to determinate appropriate temporal conditions for efficient heralded control of atomic population in a multilevel system. We may expect, that the results can be used for the enhancement of efficiency of photochemical reactions, development of new schemes of sensitive optical magnetometers, development of elements for quantum communication systems, and for other applications.
- For the first time, a systematic analysis of all cancellations of optical transitions between magnetic sublevels of hyperfine levels are considered. For simplest cases, which are $n\,^2S_{1/2} \rightarrow k\,^2P_{1/2}$ transitions, unique analytical formula for the magnetic-field value canceling transitions is obtained, which means that the uncertainty of the magnetic-field value depends only on the uncertainties of the physical quantities included in the formula. For more complicated cases involved in this thesis, that is for ^{85}Rb and ^{87}Rb isotopes $5\,^2S_{1/2} \rightarrow 5\,^2P_{3/2}$ and $5\,^2S_{1/2} \rightarrow 6\,^2P_{3/2}$ transitions, the study is done using numerical methods. These two different transitions require different laser wavelengths. The first one, ~ 795 nm, is the characteristic wavelength of cheap and widely available semiconductor red laser, which makes extremely easy the reproduction of the experiment by any experimental team. Another laser wavelength is ~ 422 nm (blue laser) and the experimental investigation of the transition cancellations will be completely new, because these transitions are not well studied, even frequency differences of fine and hyperfine

structures are not precisely measured. Wide-range magnetic-field values can serve as a tool to calibrate magnetometers and improve the accuracy of the involved physical quantities, such as frequency differences, Bohr magneton, Landé factors, etc.

1.2 Structure of the thesis

The dissertation consists of a list of figures, list of tables, list of abbreviations, a first chapter **"Introduction"**, a second chapter **"Implementation of Universal Logical Atomic Gates"**, a third chapter **"Rubidium Vapor Fluorescence in a Transient Interaction Regime"** and a fourth one **"New Standard Magnetic Field Values Determined by Transition Cancellations Between Magnetic Sublevels of Alkali Vapor"**. After these chapters and before a relevant bibliography, in the part called **"Conclusion and Outlook"** we provide the main results obtained in the thesis and discuss about further researches.

Chapters

The ***Chapter 1*** **"Introduction"** formulates the relevance of the work, goals of the research, scientific novelty and practical value of the thesis, as well as the main provisions for the defense.

In the ***Chapter 2*** **"Implementation of Universal Logical Atomic Gates"**, we consider a particular case of the atomic levels of the alkali atoms: a five-level M-type system. This M-system could be a natural one or can be created by the magnetic field due to the Zeeman effect. In the first part of this chapter we studied the way of a complete population transfer based on the technique of linear scanning of the laser field frequency near the resonance of the corresponding transition. The obtained results were also compared with the results obtained by the method based on the adiabatic population transfer of atomic levels. In the second part the simple realization of three-bit Toffoli and Fredkin programmable atomic gates on a five-level atom is demonstrated. The scheme is based on an adiabatic transfer of the populations of atomic levels. It should be mentioned, that the results were obtained using numerical methods.

Chapter 3 **"Rubidium Vapor Fluorescence in a Transient Interaction Regime"** is devoted to another type of interaction: we study the modification of the fluorescence spectra of a room-temperature atomic rubidium vapor in the region of ^{87}Rb and ^{85}Rb D_2 lines while changing the temporal rate of linear (triangular) scanning of laser radiation frequency. An increase in the ramping speed over a certain value (10^6 MHz/s) results in essential modification of magnitudes of individual atomic transitions, different on rising and falling slopes, which characterize transition from a steady state interaction regime to a transient one.

In the ***Chapter 4*** **"New Standard Magnetic-Field Values Determined by Transition Cancellations Between Magnetic Sublevels of Alkali Vapor"**, we study the behavior of ^{87}Rb and ^{85}Rb atomic vapor in a cell under the influence of a wide range of magnetic field values (from 0 to 10000 G). We have analyzed the magnetic field dependence of intensities of all the $5\,^2S_{1/2} \rightarrow 5\,^2P_{1/2,3/2}$ and $5\,^2S_{1/2} \rightarrow 6\,^2P_{1/2,3/2}$ optical transitions between magnetic sublevels of hyperfine levels, excited with π, σ^+ and σ^- polarized light. Magnetic field values canceling $5\,^2S_{1/2} \rightarrow 5\,^2P_{1/2}$ and $5\,^2S_{1/2} \rightarrow 6\,^2P_{1/2}$ transitions are given by analyt-

ical expressions. For the $5\,^2S_{1/2} \rightarrow 5\,^2P_{3/2}$ and $5\,^2S_{1/2} \rightarrow 6\,^2P_{3/2}$ transitions, magnetic field values are investigated using numerical methods. The accuracy of these values is limited by the precision of some of the involved physical quantities. Also we addressed the experimental implementation feasibility and its possible outcome.

Publications

On the topic of the dissertation, six articles are published in international peer-reviewed journals:

- [31] A. Y. Aleksanyan and E. A. Gazazyan, "Realization of the Programmable Logical Atomic Gate," *J. Contemp. Phys.*, vol. 53, pp. 205–211, Jul 2018.
- [32] A. Aleksanyan, S. Shmavonyan, E. Gazazyan, A. Khanbekyan, H. Azizbekyan, M. Movsisyan, and A. Papoyan, "Fluorescence of rubidium vapor in a transient interaction regime," *J. Opt. Soc. Am. B*, vol. 37, no. 1, pp. 203–210, Jan 2020.
- [33] A. Aleksanyan, R. Momier, E. Gazazyan, A. Papoyan, and C. Leroy, "Transition cancellations of ^{87}Rb and ^{85}Rb atoms in a magnetic field," *J. Opt. Soc. Am. B*, vol. 37, no. 11, pp. 3504–3514, Nov 2020.
- [34] R. Momier, A. Aleksanyan, E. Gazazyan, A. Papoyan, and C. Leroy, "New standard magnetic field values determined by cancellations of ^{85}Rb and ^{87}Rb atomic vapors $5\,^2S_{1/2} \rightarrow 6\,^2P_{1/2,\,3/2}$ transitions," *J. Quant. Spectrosc. Radiat. Transfer*, vol. 257, p. 107371, Dec 2020.
- [35] A. Y. Aleksanyan, "Effective Full Population Transfer in M-System Using Scanning Technique," *J. Contemp. Phys.*, vol. 56, pp. 6–12, Apr 2021.
- [36] A. Aleksanyan, R. Momier, E. Gazazyan, A. Papoyan, and C. Leroy, "Cancellation of D_1 line transitions of alkali-metal atoms by magnetic-field values," *Phys. Rev. A*, vol. 105, p. 042810, Apr 2022.

Approbation of the work

The results presented in the dissertation were reported at the following conferences:

- A. Aleksanyan and E. Gazazyan. *Implementation of programmable logical atomic gate.* Laser Physics 2017 International Conference (LP2017). At: Institute for Physical Research, NAS of RA, Ashtarak, Armenia, (2017).
- A. Aleksanyan, S. Shmavonyan, E. Gazazyan, A. Khanbekyan, H. Azizbekyan, M. Movsisyan, and A. Papoyan. *Fluorescence of ^{85}Rb and ^{87}Rb vapor in a transient interaction regime.* Laser Physics 2019 International Conference (LP2019). At: Institute for Physical Research, NAS of RA, Ashtarak, Armenia, (2019).
- A. Aleksanyan, E. Gazazyan, C. Leroy, and G. Grigoryan. *Total transfer of population*

in multi-level system by chirped frequency. 7th International Symposium on Optics & its Applications (OPTICS-2019), Yerevan, Armenia, (2019).

- A. Aleksanyan, R. Momier, E. Gazazyan, A. Papoyan, and C. Leroy. *Alkali atom transition cancellations within magnetic field.* 52nd Conference of the European Group on Atomic Systems, Online (VI-EGAS52), (2021).
- S. Petrosyan, A. Aleksanyan, and E. Gazazyan. *Amplification of Light Signal on V-type Atomic System.* 52nd Conference of the European Group on Atomic Systems, Online (VI-EGAS52), (2021).
- A. Aleksanyan, R. Momier, E. Gazazyan, A. Papoyan, and C. Leroy. *Magnetic field values canceling alkali atoms' transitions.* 14th European Conference on Atoms Molecules and Photons (ECAMP14), Vilnius, Lithuania, (2022).
- R. Momier, A. Aleksanyan, A. Sargsyan, A. Tonoyan, M. Auzinsh, D. Sarkisyan, A. Papoyan, and C. Leroy. *Magnetometry with a nanometric-thin K vapor cell.* 14th European Conference on Atoms Molecules and Photons (ECAMP14), Vilnius, Lithuania, (2022).

The results were also presented at the annual reports of the Institute for Physical Research of National Academy of Sciences, Armenia, discussed at the Theoretical Physics Laboratory's seminars of the same institution, and at the Laboratoire Interdisciplinaire Carnot de Bourgogne at the University of Bourgogne, France and also during joint seminars between these institutions.

I was to participate in international conferences of physics, planned and funded by ICB-Dijon-France and IPR-Ashtarak-Armenia, but the Covid-19 pandemic banned all these conferences.

Workload

The content of the thesis is presented on 110 pages, it contains 36 figures, 23 tables and 158 references.

Chapter 2

Implementation of Universal Logical Atomic Gates

2.1 Introduction

The classical theory of information science began in 1936 when Turing [37] and Church [38], independently of each other, published their papers on the nature of computations. In 1961, Landauer showed that any irreversible computation leads to an inevitable dissipation of energy [39] and an additional heating of the components.

In recent decades, quantum computing has developed very rapidly, but the problem associated with the creation of quantum memory devices is still relevant [40–43]. Another problem is the design of the given coherent superposition states of atoms in a macroscopic volume [44–46], which is necessary to create logical gates [47–49]. One of the promising solutions to the above problems is the recording and reproduction of optical quantum information based on the electromagnetically induced transparency of the atomic media [50–53].

The only alternative to overcome the "Landauer limit" [54] is the use of computations with the reversible gates. The examples of reversible gates are the Toffoli and Fredkin gates [40]. The three-bit Toffoli gate (the CCNOT gate) has three inputs and three outputs. Two bits are the static ones (the control bits, columns 1 and 2 of Table 2.1), and the third bit (the target bit, column 3 of Table 2.1) changes if and only if the static bits have the value of 1. But in the three-bit Fredkin gate (the CSWAP gate), the first bit is a static (the control bit, column 1 of Table 2.2), and the second and third bits (the target bits, columns 2 and 3 of Table 2.2) are swapped when the first bit has the value of 1. The schemes of these gates are depicted on Figure 2.1. Both gates are universal, that is, using only one type of these gates, any reversible logic scheme can be constructed. Owing to the properties of reversibility and universality, the Toffoli and Fredkin gates play an important role not only in the classic but also in the quantum computations.

Table 2.1: Truth table of CCNOT gate.

Input			Output		
0	0	0	0	0	0
0	0	1	0	0	1
0	1	0	0	1	0
0	1	1	0	1	1
1	0	0	1	0	0
1	0	1	1	0	1
1	1	0	1	1	1
1	1	1	1	1	0

Table 2.2: Truth table of CSWAP gate.

Input			Output		
0	0	0	0	0	0
0	0	1	0	0	1
0	1	0	0	1	0
0	1	1	0	1	1
1	0	0	1	0	0
1	1	0	1	0	1
1	0	1	1	1	0
1	1	1	1	1	1

Figure 2.1: (a) Toffoli and (b) Fredkin reversible gate schemes. The black circles stand for the control bits, and crosses for the target bits.

The possibility of realization of the Toffoli gate on a three-level atomic Λ-system using short pulses whose duration is less than the relaxation times in the system was demonstrated in [55]. The adiabatic population transfer was done using the methods of stimulated Raman adiabatic passage (STIRAP) [45, 56–59] and bright-state stimulated Raman adiabatic passage (b-STIRAP) [53, 59, 60], which make the Λ-system completely reversible. With the duration of the laser pulses $\sim 10^{-10}$ s, the same pulse sequence can result in the transfer of population from one ground state to another and back without losses.

The coherent cyclic population transfer can be implemented also in the multilevel systems [56]. This makes it possible to realize an optical reversible universal logic gate in such systems. One such model of the Toffoli gate was considered in [61]. The main difficulty for the experimental realization of the models proposed in [55, 61] is that the laser pulses were used as control bits, and the populations of atomic levels as a target bit. In addition, these studies did not take into account the relaxation processes resulting in the dissipation and dephasing of the coherences induced in the media.

In this chapter another method of a complete population transfer and a simple realization of programmable atomic gates on the five-level atom (M-system) are demonstrated. The method for the complete population transfer is based on the technique of linear scanning of the laser field frequency close to the resonant frequency of the corresponding transition. Moreover, the comparison of the complete population transfer obtained using the scan technique with the

results obtained by the method based on pulse sequences is made. The realization of the programmable logical atomic gates is based on a cyclical adiabatic population transfer. A generalization of the STIRAP and b-STIRAP methods on a five-level M-system is considered for the pulses of arbitrary duration, taking into account all the relaxation processes. The proposed models of optical reversible universal logic elements can serve as a basis for the design of a reversible optical processor operating on the cyclic transfer of atomic populations.

2.2 Density matrix theory and overview of some techniques and approximations

In this section we are going to discuss a bit about the theory of density matrix, about laser field - atomic system interaction in the case of Λ-system with some common approximations in laser physics (Electric Dipole and Rotating Wave Approximations), Apart from that, we will briefly take a look at a few well-known techniques, which allow us to perform effective adiabatic population transfer between the levels of atomic systems.

2.2.1 Density matrix theory

In this subsection we will briefly discuss the density matrix theory. More detailed information is available in Ref. [62]. In classical mechanics, at every moment of time t, the dynamics of a system is known if all the positions and momenta of all the particles are given. Often we are dealing with a lot of particles and only the averages of the mentioned above quantities are known. It means that we do not have a complete information about the system, so the methods of statistical mechanics must be applied. As we are interested in quantum systems, it means that complete information about the considered system is not available in any case because of Heisenberg's uncertainty principle. In addition to this, the "maximum possible information" in quantum physics has a more strict meaning than in classical physics. Not all the observables can be measured at the same time with precision, so we need to understand what means "maximum possible information" in quantum mechanics.

It is well known, that two quantities can be simultaneously and precisely measured only if the two operators corresponding to these quantities commute. Thus, if operators Q_1 and Q_2 commute, it is possible to find states (defining a common basis) corresponding to operators Q_1 and Q_2 with certain eigenvalues q_1 and q_2. In the same way, if operator Q_3 commutes with both Q_1 and Q_2 operators, it is possible to find states (i.e. a common basis) where Q_1, Q_2 and Q_3 have eigenvalues q_1, q_2 and q_3 respectively, and so on. The eigenvalues can give precisely the system classification if these eigenvalues make it possible to unambiguously distinguish the states of the system. The largest set of mutually commuting observables give the "maximum possible information" about the system. But if there exist an observable, which operator does not commute with the operators of the set of Q_1, Q_2, ... observables, at least one of the observables will have uncertainty. So, it is not possible to give more complete specification of the quantum system.

In general, "maximum possible information" is given by the q_1, q_2, ... eigenvalues of a commuting set of observables Q_1, Q_2, ..., which are measured. The system is specified by the state vector $|q_1, q_2, \ldots\rangle$. Doing the same experiment, one will obtain the same results again.

Pure states represent the maximum information (the limit of precise observation) that we can have, which are permitted by Heisenberg's uncertainty principle, are the quantum mechanical analogues of classical invariants or constants of motion from which all the mechanical characteristics of the particles are known (i.e. all positions and momenta).

To get deeper, now we will consider two sets of observables. The first set is Q_1, Q_2, ... with eigenstates $|\psi\rangle = |q_1, q_2, \ldots\rangle$, and the second one is Q_1', Q_2', ... with eigenstates $|\phi\rangle = |q_1', q_2', \ldots\rangle$. Here at least one of the operators Q_i' does not commute with the first set. Assuming that the basis states $\left(|\phi_n\rangle\right)$ are orthonormal and complete, let us represent our system by the state vector $|\psi\rangle$ and write it as a superposition of the eigenstates of Q_1', Q_2', ...:

$$|\psi\rangle = \sum_n a_n |\phi_n\rangle , \tag{2.1}$$

where the index n distinguishes the different eigenstates. The normalization will be done in the following way:

$$\langle\psi|\psi\rangle = \sum_n |a_n|^2 = 1, \tag{2.2}$$

where $|a_n|^2$ is the probability that a measurement will find the system in the n^{th} eigenstate.

Now we will consider a mixture of independently prepared states $|\psi_n\rangle$. The density operator is as follows

$$\rho = \sum_n W_n |\psi_n\rangle \langle\psi_n| , \tag{2.3}$$

where W_n are statistical weights. We need to choose a convenient set of basis states to express the density operator in matrix form. Let us denote them as $|\phi_1\rangle$, $|\phi_2\rangle$, ... From the relation (2.1) we obtain

$$|\psi_n\rangle = \sum_{m'} a_{m'}^{(n)} |\phi_{m'}\rangle \quad \text{and} \quad \langle\psi_n| = \sum_m a_m^{(n)*} \langle\phi_m| , \tag{2.4}$$

and relation (2.3) can be written in the following form:

$$\rho = \sum_{nm'm} W_n a_{m'}^{(n)} a_m^{(n)*} |\phi_{m'}\rangle \langle\phi_m| . \tag{2.5}$$

Then applying orthonormality conditions on the matrix elements of the right hand side of the operator (2.5), we obtain

$$\langle\phi_i| \rho |\phi_j\rangle = \sum_n W_n a_i^{(n)} a_j^{(n)*}. \tag{2.6}$$

As $|\phi_n\rangle$ basis states were used, formula (2.6) gives the elements of the density matrix in the $|\phi_n\rangle$ representation.

W_n is the probability to find the system in the state $|\psi_n\rangle$, and the probability that $|\psi_n\rangle$ can

be found in the state $|\phi_m\rangle$ is $\left|a_m^{(n)}\right|^2$. By the diagonal element $\rho_{m,m}$, the probability of finding the system in the state $|\phi_m\rangle$ is given:

$$\rho_{m,m} = \sum_n W_n \left|a_m^{(n)}\right|^2 . \tag{2.7}$$

Just to remind, the trace of any matrix is constant and thus independent of the representation:

$$\mathrm{Tr}(\rho) = \sum_i \rho_{i,i} = \sum_i \sum_n W_n \left|a_i^{(n)}\right|^2 = 1. \tag{2.8}$$

The trace of the product of ρ and the operator Q will gives the average value of this operator:

$$\langle Q \rangle = \sum_{mm'} \sum_n W_n a_{m'}^{(n)} a_m^{(n)*} \langle \phi_m | Q | \phi_{m'} \rangle = \sum_{mm'} \langle \phi_{m'} | \rho | \phi_m \rangle \langle \phi_m | Q | \phi_{m'} \rangle = \mathrm{Tr}(\rho Q) \tag{2.9}$$

Relation (2.9) indicates that the expectation value of an operator, which is an information of the system we want to extract, implies to determine the density matrix.

Taking the time derivative of the density operator (2.3), we obtain

$$\frac{d\rho}{dt} = \sum_n W_n \left(\frac{d}{dt} |\psi_n\rangle \langle \psi_n| + |\psi_n\rangle \frac{d}{dt} \langle \psi_n| \right). \tag{2.10}$$

From the Schrödinger equation

$$i\hbar \frac{d|\psi_n\rangle}{dt} = H |\psi_n\rangle \tag{2.11}$$

and its adjoint, Eq. (2.10) becomes:

$$i\hbar \frac{d\rho}{dt} = [H, \rho], \tag{2.12}$$

where $[H, \rho] = H\rho - \rho H$ is the commutator between the Hamiltonian H and the density matrix ρ. This equation is called Liouville equation, which is a more comfortable way to include the statistical distribution than the Schrödinger equation.

2.2.2 Lindblad equation

Until this moment we have not considered the interaction of the system with its environment, which brings to the dissipation of energy, causing decay and phase randomization. This interaction consideration is important to understand a lot of fundamental phenomena, like the spontaneous emission of light from excited atoms, or the performance of many quantum technological devices, like the laser. For more details, see Ref. [63] and Ref. [64].

Taking into account dissipation processes, such as spontaneous decay, collisions, etc. (that

is, we consider an open system), Eq. (2.12) transforms into the Lindblad master equation:

$$i\hbar\frac{d\rho}{dt} = [H,\rho] + i\hbar\cdot\sum_{n,m=1}^{N^2-1} h_{n,m}\left(A_n\rho A_m^\dagger - \frac{1}{2}\{A_m^\dagger A_n,\rho\}\right). \tag{2.13}$$

Here $\{A_m\}$ is a basis of orthonormal Hilbert-Schmidt operators acting on the Hilbert space [65] of the N-dimensional system. The second term of the right hand side of Eq. (2.13) is usually called the dissipator, the term $h_{n,m}$ in the dissipator is the Fourier transform of the homogeneous reservoir correlation functions, is positive by Bochner's theorem [66] and hence h can be diagonalized. If the matrix h is zero, then the mentioned above equation reduces to the Liouville equation. The anticommutator is defined as $\{A_m^\dagger A_n,\rho\} = A_m^\dagger A_n\rho + \rho A_m^\dagger A_n$.

With a unitary transformation u, the matrix h can be diagonalized:

$$u^\dagger h u = \begin{bmatrix} \lambda_1 & 0 & \cdots & 0 \\ 0 & \lambda_2 & \cdots & 0 \\ \vdots & \vdots & \ddots & \vdots \\ 0 & 0 & \cdots & \lambda_{N^2-1} \end{bmatrix}. \tag{2.14}$$

In the result, the eigenvalues λ_i are non-negative. Defining another orthonormal operator basis by $L_i = \sum_{j=1}^{N^2-1} u_{j,i}A_j$, the Lindblad equation will have a diagonal form and will be:

$$i\hbar\frac{d\rho}{dt} = [H,\rho] + i\hbar\cdot\sum_{i=1}^{N^2-1} \lambda_i\left(L_i\rho L_i^\dagger - \frac{1}{2}\{L_i^\dagger L_i,\rho\}\right). \tag{2.15}$$

Operators L_i are called the systems' Lindblad or jump operators.

We stress that the physical assumptions underlying the Lindblad form of the master equation are the Born (weak coupling) [63], Markov (memoryless) [67] and Rotating Wave [68] approximations. The next subsection is devoted to the consideration of some of these approximations and some well-known techniques of population transfer in the case of Λ-type atomic system.

2.2.3 Brief analysis of adiabatic passages using Electric Dipole and Rotating Wave Approximations

We will briefly review the relevant physics of coherent-adiabatic interactions between lasers and quantized media. The latter could be atoms or molecules in the gas phase, as well as appropriate "atom-like" solid media. Coherent interactions rely on the fact that a laser exhibits a strong electromagnetic field which, together with the internal electromagnetic field of the quantum system interacts with the electronic subsystem of the latter. This modifies the quantized level structure of the atom and also the population distributions among the quantum states (as well as the coherences between the quantum states). As we can control the level structure and

population distribution in the medium, we have an access to steer many physical properties or processes of the system. We note that not only the strength of the radiation field, but also the coherence properties plays a role here. Thus, quantum interference may enhance or suppress properties and processes in the coherently-driven medium.

STIRAP and b-STIRAP techniques: This technique already exhibits a well-established tool to manipulate population distributions of atomic and molecular medium in the gas phase [45, 59]. STIRAP relies on the adiabatic interaction of two near-resonant laser pulses with a three-level Λ–type system [see Figure 2.2].

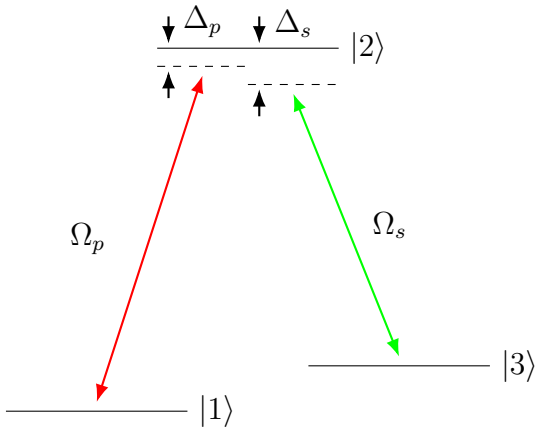

Figure 2.2: Scheme of Λ-type atomic system levels.

The Hamiltonian of our system could be represented as

$$H = H_0 + H_1, \tag{2.16}$$

where H_0 is the Hamiltonian of the free atom without external fields and H_1 describes the perturbation due to the applied laser field. In the terms of eigenstates of free Hamiltonian $|n\rangle$, the H_0 may be written as:

$$H_0 = \begin{pmatrix} \hbar\omega_1 & 0 & 0 \\ 0 & \hbar\omega_2 & 0 \\ 0 & 0 & \hbar\omega_3 \end{pmatrix}. \tag{2.17}$$

According to the Figure 2.2, the external electric field could be written as the sum of applied two laser field electric components:

$$E = E_p \cos\left(\omega_p t - \mathbf{k_p r}\right) + E_s \cos\left(\omega_s t - \mathbf{k_s r}\right). \tag{2.18}$$

As the magnetic field components of the lasers are very weak compared to the electric field ones (by an order $1/c^2$), it is relevant not to take them into account. When we can neglect the spatial phase shift of the wave over the effective atomic space, this approximation is called the Electric Dipole Approximation. Below we will derive a simple explanation about that. For a more deep discussion one can see references [69, 70]. The **kr** terms on the right side

of Eq. (2.18) are $2\pi r/\lambda_{p,s}$, where $\lambda_{p,s}$ the applied laser wavelengths are. As in this thesis we examine alkali atoms, for the energy levels involved in our studies $r \sim r_a$, where $r_a^{\mathrm{Cs}} \approx 0.265$ nm is the atomic radius of Caesium. It should be noted, that $r_a^{\mathrm{Na}} < r_a^{\mathrm{K}} < r_a^{\mathrm{Rb}} < r_a^{\mathrm{Cs}}$. Caesium van der Waals radius is $r_{\mathrm{vdW}} = 0.343$ nm and covalent radius is $r_{\mathrm{cov}} = 0.244$ nm. For optical transitions the laser wavelength is in visible or near-infrared range ($\lambda_{p,s}^{\mathrm{Cs}} \approx 852$ nm) and $\overline{r}/\lambda_{p,s} = \dfrac{0.265 \text{ nm}}{852 \text{ nm}} \approx 3 \times 10^{-4} \ll 1$. Thus the term $\mathbf{kr}$ of Eq. (2.18) can be neglected and it becomes

$$E = E_p \cos\omega_p t + E_s \cos\omega_s t = \frac{E_p}{2}\left(e^{i\omega_p t} + e^{-i\omega_p t}\right) + \frac{E_s}{2}\left(e^{i\omega_s t} + e^{-i\omega_s t}\right). \tag{2.19}$$

With d the dipole moment operator and $U(t) = e^{iH_0 t/\hbar}$ the time evolution operator, the perturbation Hamiltonian $H_1 = -dE$ will be

$$UH_1U^\dagger = -E\begin{pmatrix} 0 & d_{1,2}e^{-i(\omega_2-\omega_1)t} & 0 \\ d_{2,1}e^{i(\omega_2-\omega_1)t} & 0 & d_{2,3}e^{i(\omega_2-\omega_3)t} \\ 0 & d_{3,2}e^{-i(\omega_2-\omega_3)t} & 0 \end{pmatrix}. \tag{2.20}$$

The exponential parts of the $UH_1U^\dagger$ non-zero matrix elements have

$$e^{\pm i(\omega_2-\omega_{1,3}+\omega_{p,s})t} + e^{\pm i(\omega_2-\omega_{1,3}-\omega_{p,s})t} = e^{\pm i(\omega_2-\omega_{1,3}-\omega_{p,s})t}\left[1 + e^{\pm 2i\omega_{p,s}t}\right] \tag{2.21}$$

form, with the obvious assumptions [see Figure 2.2] that $\omega_1 \approx \omega_3$ and $\omega_p \approx \omega_s$. Let us analyze the term $1 + e^{\pm 2i\omega_{p,s}t}$. For a time of detection, or a time of interaction or any characteristic time T_c, the average value of this term is:

$$\overline{1 + e^{\pm 2i\omega_{p,s}t}} = \frac{1}{T_c}\int_0^{T_c}\left[1 + e^{\pm 2i\omega_{p,s}t}\right]dt = 1 \mp i\frac{1}{2\omega_{p,s}T_c}\left[e^{\pm 2i\omega_{p,s}T_c} - 1\right]. \tag{2.22}$$

Now we want to understand when the value of right hand side of the Eq. (2.22) is approximately equal to one. After decomposition we will obtain:

$$\overline{1 + e^{\pm 2i\omega_{p,s}t}} = 1 \pm \frac{1}{\omega_{p,s}T_c}\left[\frac{\pm\sin 2\omega_{p,s}T_c - i\left(\cos 2\omega_{p,s}T_c - 1\right)}{2}\right]. \tag{2.23}$$

Thus $\overline{1 + e^{\pm 2i\omega_{p,s}t}} = 1 \pm \dfrac{1}{\omega_{p,s}T_c} \cdot z$ with $0 \leq |z| \leq 1$. Taking for instance the wavelength of the optical transitions of Caesium $\lambda_{p,s}^{\mathrm{Cs}} \approx 852$ nm, and considering the case where the characteristic time T_c is an experimental time, it gives $4.5\times10^{-16} \leq \dfrac{1}{\omega_{p,s}T_c} \leq 4.5\times10^{-1}$ for 10^{-15} s $\leq T_c \leq 1$ s. This means that as long as the physical phenomena observed are not of femtosecond order, approximating the average value $\overline{1 + e^{\pm 2i\omega_{p,s}t}}$ by 1 is an excellent approximation called the Rotating Wave Approximation (abbreviated RWA in the literature, see for instance Ref. [68]).

Consequently, the non-zero matrix elements (2.21) verify:

$$e^{\pm i(\omega_2-\omega_{1,3}+\omega_{p,s})t}+e^{\pm i(\omega_2-\omega_{1,3}-\omega_{p,s})t}=e^{\pm i(\omega_2-\omega_{1,3}-\omega_{p,s})t}\left[1+e^{\pm 2i\omega_{p,s}t}\right]\approx e^{\pm i(\omega_2-\omega_{1,3}-\omega_{p,s})t}. \quad (2.24)$$

Coming back to Schrödinger representation and after combining with the Hamiltonian of free atom, we will obtain

$$H=-\frac{\hbar}{2}\begin{pmatrix}0 & \Omega_p & 0\\ \Omega_p & -2\Delta_p & \Omega_s\\ 0 & \Omega_s & -2\delta\end{pmatrix}, \quad (2.25)$$

where $\Omega_p=\dfrac{E_p\left|d_{1,2}\right|}{\hbar}$ and $\Omega_s=\dfrac{E_s\left|d_{3,2}\right|}{\hbar}$ are the Rabi frequencies of the pump and Stokes laser fields respectively, $\delta=\Delta_p-\Delta_s$ is the two-photon detuning, and $\Delta_p=\omega_2-\omega_1-\omega_p$ and $\Delta_s=\omega_2-\omega_3-\omega_s$ are single-photon detunings. When $\Delta_p=\Delta_s$, then the two-photon detuning δ is zero.

The bare states $|1\rangle$, $|2\rangle$ and $|3\rangle$ are no more eigenstates of the strongly driven system, so we have to pass to others eigenstates:

$$\begin{aligned}|a^0\rangle&=\cos\Theta\,|1\rangle-\sin\Theta\,|3\rangle\,,\\ |a^+\rangle&=\sin\Phi\left(\sin\Theta\,|1\rangle+\cos\Theta\,|3\rangle\right)+\cos\Phi\,|2\rangle\,,\\ |a^-\rangle&=\cos\Phi\left(\sin\Theta\,|1\rangle+\cos\Theta\,|3\rangle\right)-\sin\Phi\,|2\rangle\,,\end{aligned} \quad (2.26)$$

where Φ and Θ are the mixing angles. The tangents of mixing angles, depending on the time are

$$\begin{aligned}\tan 2\Phi(t)&=\frac{\Omega(t)}{\Delta},\\ \tan\Theta(t)&=\frac{\Omega_p(t)}{\Omega_s(t)},\end{aligned} \quad (2.27)$$

where we denoted $\Omega(t)=\sqrt{\Omega_p^2(t)+\Omega_s^2(t)}$.

We call the state $|a^0\rangle$ the "dark" state. From Eq. (2.26) it is obvious, that the "dark" state does not include any contribution of $|2\rangle$, thus it does not suffer from the fluorescence decay. In contrast, the "bright" states $|a^\pm\rangle$ include decay of state $|2\rangle$.

Let us to examine the "dark" state. It should be mentioned, that the laser pulses are delayed in time. When $\cos\Theta\to 1$, the state $|a^0\rangle$ corresponds to the initial state $|1\rangle$. To obtain this, we need to provide the following: $\Omega_s\gg\Omega_p$ (i.e. strong Stokes laser pulse compared with the pump pulse). If $\sin\Theta\to 1$, the state $|a^0\rangle$ corresponds to the final state $|3\rangle$. This requires $\Omega_p\gg\Omega_s$ (i.e. strong pump laser pulse compared with the Stokes pulse). A pulse sequence "Stokes preceding pump" transfers the system directly from the $|1\rangle$ to the $|3\rangle$ via the dark state $|a^0\rangle$ [see Figure 2.3]. This is the essence of the STIRAP technique.

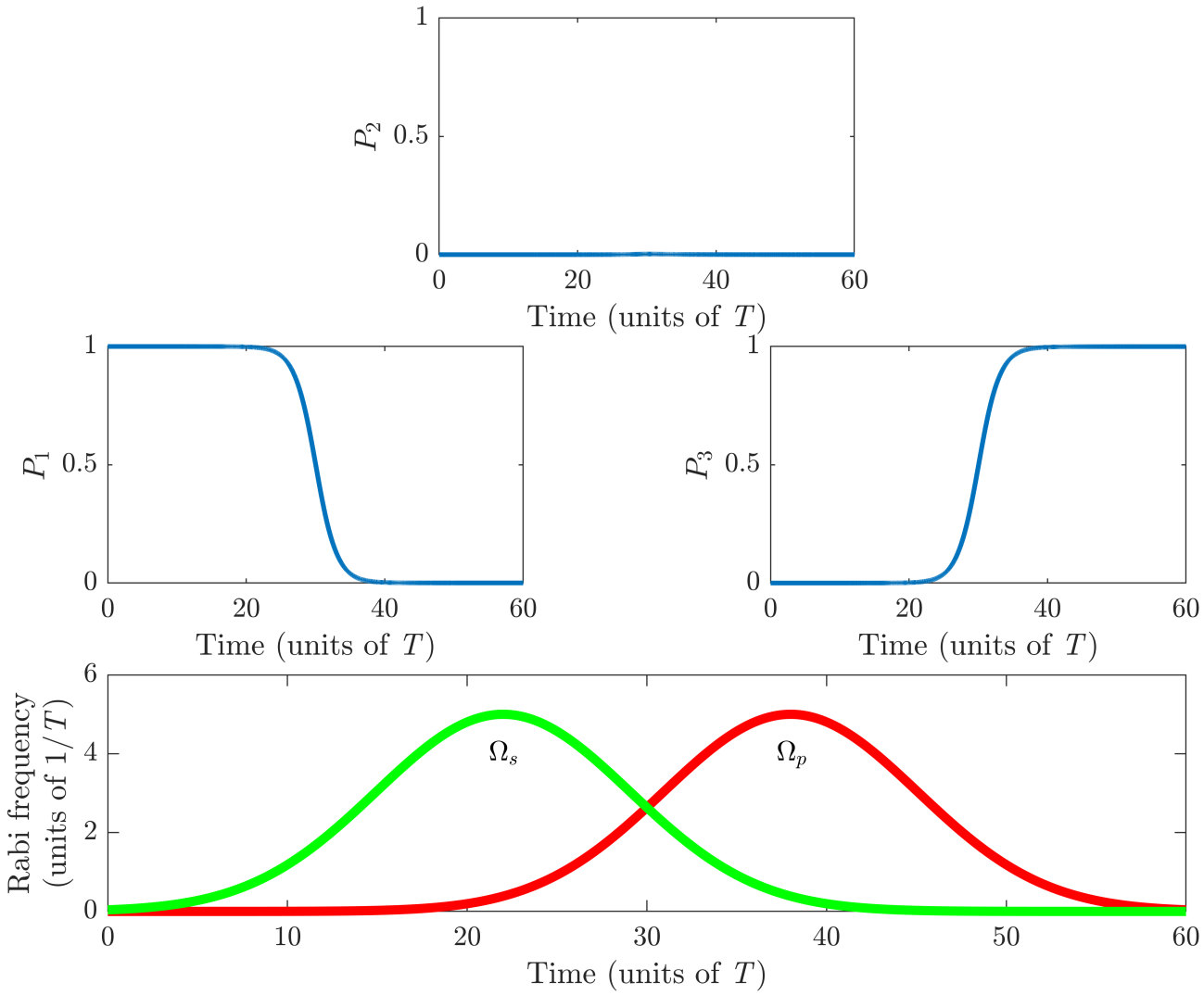

Figure 2.3: Population transfer via the "dark" state. To obtain this result we used the following parameter values: $\Delta = 5$, $\Omega_p = \Omega_s = 5$, and the peaks of pulses correspond to the values $t_s = 22$ and $t_p = 38$. All parameters are normalized to the average pulse duration T.

Efficient population transfer is also possible via the "bright" states (b-STIRAP technique). State $|a^+\rangle$ initially should correspond to the state $|1\rangle$ (i.e. $\sin\Theta \to 1$). To be able to carry out population transfer we need to provide the following conditions: $\Delta \gg \Omega_s$ and $\Delta \gg \Omega_p$. In other words the detuning of the system should be large compared to the pulses, and the pump laser pulse should exceed the Stokes pulse many times. At the end of the process the state $|a^+\rangle$ should correspond to the state $|3\rangle$ ($\cos\Theta \to 1$). To complete this we need to have more stronger Stokes pulse than a pump pulse: $\Omega_s \gg \Omega_p$. It follows, that a sequence "the Stokes pulse following the pump pulse" transfers the population of the system from state $|1\rangle$ to state $|3\rangle$ via the "bright" state $|a^+\rangle$. During this process some transient population is stored on the state $|2\rangle$. The fraction of transient population is given by $\cos\Phi$ term. If the detuning Δ is large enough and the lifetime of the state $|2\rangle$ is many times long compared with the interaction time, the efficiency of the b-STIRAP technique approaches the efficiency of the STIRAP technique.

RAP technique: Another adiabatic process than STIRAP has a huge interest in laser-based physics. The technique of rapid adiabatic passage (RAP) [71] relies on the interaction

of a two-level system with a resonant pump laser pulse and an intense, off-resonant Stark laser pulse. The latter drives dynamic Stark shifts in the medium. RAP permits complete transfer of atomic populations between two quantum states, and also permits strong enhancement of nonlinear optical processes in the coherently-driven medium [72].

The effects of spatial dispersion, caused by finite sizes of the interaction region, on coherent processes such like STIRAP or RAP are by far not completely studied. Any resonant medium of finite size is spatially inhomogeneous (i.e. it exhibits spatial dispersion). This dispersion is most prominently displayed in a gaseous medium due to thermal motion of atoms. By collisions with the cell walls, atoms lose their excitation and only after traveling some distance in the radiation field they "forget" the collision. This propagation distance (averaged over all thermal atomic velocities) defines the typical scale of spatial dispersion. In a simple two-level model the relevant scale is determined in [73].

2.3 Basic equations describing M-type system of an alkali atom

Let us consider a five-level atomic system that interacts with four pulses of Gaussian shape and of arbitrary duration. The frequency of each pulse is close to the resonance frequency of an atomic transition.

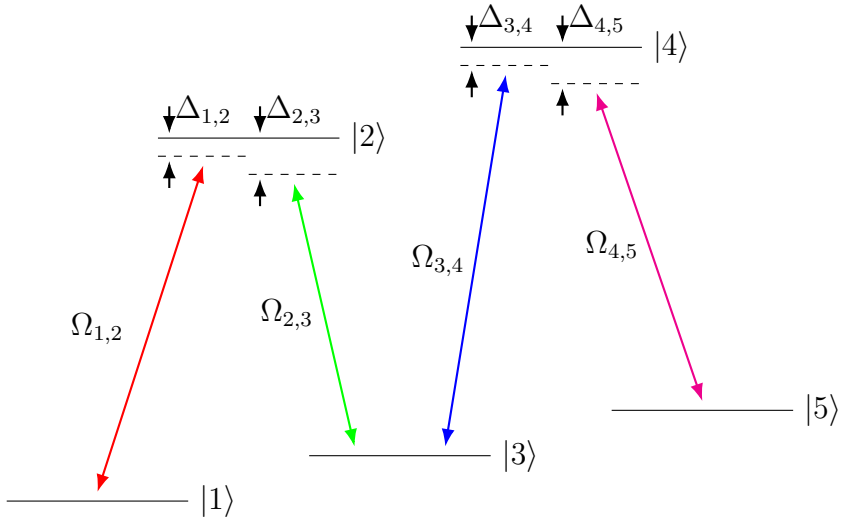

Figure 2.4: Scheme of atomic levels in the M-system.

With the use of the Lindblad operator Λ, the Lindblad equation (2.12) is usually written in the more compact form:

$$\frac{d\rho}{dt} = -\frac{i}{\hbar}[H, \rho] + \Lambda(\rho). \tag{2.28}$$

The Lindbladian Λ, also called Lindblad superoperator, models the environmental conditions that make up the open quantum system such as dephasing and relaxation.

The interaction Hamiltonian of the scheme depicted in Figure 2.4 has the following form:

$$H(t) = \begin{pmatrix} 0 & \Omega_{1,2}e^{-i\Delta_{1,2}t} & 0 & 0 & 0 \\ \Omega_{2,1}e^{i\Delta_{2,1}t} & 0 & \Omega_{2,3}e^{i\Delta_{2,3}t} & 0 & 0 \\ 0 & \Omega_{3,2}e^{-i\Delta_{3,2}t} & 0 & \Omega_{3,4}e^{-i\Delta_{3,4}t} & 0 \\ 0 & 0 & \Omega_{4,3}e^{i\Delta_{4,3}t} & 0 & \Omega_{4,5}e^{i\Delta_{4,5}t} \\ 0 & 0 & 0 & \Omega_{5,4}e^{-i\Delta_{5,4}t} & 0 \end{pmatrix}. \tag{2.29}$$

Here $\Delta_{i,j}$ are the time-dependent one-photon detunings defined as $\Delta_{1,2} = \frac{E_2 - E_1}{\hbar} - \omega_L^{(1,2)}(t)$, $\Delta_{2,3} = \frac{E_2 - E_3}{\hbar} - \omega_L^{(2,3)}(t)$, $\Delta_{3,4} = \frac{E_4 - E_3}{\hbar} - \omega_L^{(3,4)}(t)$ and $\Delta_{4,5} = \frac{E_4 - E_5}{\hbar} - \omega_L^{(4,5)}(t)$, where E_i is the energy of the i^{th} atomic level, and $\omega_L^{(i,j)}$ denotes the frequency of laser pulses of Gaussian form. Multi-photon detunings are expressed through one-photon detunings as follows:
i) two-photon detunings are

$$\begin{aligned} \Delta_{1,3}(t) &= \Delta_{1,2}(t) - \Delta_{2,3}(t), \\ \Delta_{2,4}(t) &= -\Delta_{2,3}(t) + \Delta_{3,4}(t), \\ \Delta_{3,5}(t) &= \Delta_{3,4}(t) - \Delta_{4,5}(t), \end{aligned} \tag{2.30}$$

ii) three-photon detunings are

$$\begin{aligned} \Delta_{1,4}(t) &= \Delta_{1,2}(t) - \Delta_{2,3}(t) + \Delta_{3,4}(t), \\ \Delta_{2,5}(t) &= -\Delta_{2,3}(t) + \Delta_{3,4}(t) - \Delta_{4,5}(t), \end{aligned} \tag{2.31}$$

iii) and the only four-photon detuning has the following form:

$$\Delta_{1,5}(t) = \Delta_{1,2}(t) - \Delta_{2,3}(t) + \Delta_{3,4}(t) - \Delta_{4,5}(t). \tag{2.32}$$

$\Omega_{i,j} = \Omega_{j,i}^*$ are the Rabi frequencies of the corresponding pulses (Figure 2.4). In the matrix form, the Lindblad operator [74] can be written as

$$\Lambda(\rho) = \begin{pmatrix} \Gamma_{2,1}\rho_{2,2} & \gamma_1\rho_{1,2} & 0 & \gamma_2\rho_{1,4} & 0 \\ \gamma_1\rho_{2,1} & 2\gamma_1\rho_{2,2} & \gamma_1\rho_{2,3} & (\gamma_1+\gamma_2)\,\rho_{2,4} & \gamma_1\rho_{2,5} \\ 0 & \gamma_1\rho_{3,2} & \Gamma_{2,3}\rho_{2,2} + \Gamma_{4,3}\rho_{4,4} & \gamma_2\rho_{3,4} & 0 \\ \gamma_2\rho_{4,1} & (\gamma_1+\gamma_2)\,\rho_{4,2} & \gamma_2\rho_{4,3} & 2\gamma_2\rho_{4,4} & \gamma_2\rho_{4,5} \\ 0 & \gamma_1\rho_{5,2} & 0 & \gamma_2\rho_{5,4} & \Gamma_{4,5}\rho_{4,4} \end{pmatrix}, \tag{2.33}$$

where $\gamma_1 = -\frac{\Gamma_{2,1} + \Gamma_{2,3}}{2}$, $\gamma_2 = -\frac{\Gamma_{4,3} + \Gamma_{4,5}}{2}$ and $\Gamma_{i,j}$ is the natural linewidth of the $i \to j$ spontaneous emission transition. So, the system of the equations for five level M-system will

consist of 15 first order differential equations, which are the followings:

$$
\begin{cases}
\dot{\rho}_{1,1} = i\left(\Omega_{1,2}\rho_{1,2} - \Omega_{1,2}\rho_{2,1}\right) + \Lambda_{1,1}(\rho), \\
\dot{\rho}_{1,2} = i\left(\Delta_{1,2}\rho_{1,2} + \Omega_{1,2}\rho_{1,1} - \Omega_{1,2}\rho_{2,2} + \Omega_{2,3}\rho_{1,3}\right) + \Lambda_{1,2}(\rho), \\
\dot{\rho}_{1,3} = i\left(\Delta_{1,3}\rho_{1,3} - \Omega_{1,2}\rho_{2,3} + \Omega_{2,3}\rho_{1,2} + \Omega_{3,4}\rho_{1,4}\right) + \Lambda_{1,3}(\rho), \\
\dot{\rho}_{1,4} = i\left(\Delta_{1,4}\rho_{1,4} - \Omega_{1,2}\rho_{2,4} + \Omega_{3,4}\rho_{1,3} + \Omega_{4,5}\rho_{1,5}\right) + \Lambda_{1,4}(\rho), \\
\dot{\rho}_{1,5} = i\left(\Delta_{1,5}\rho_{1,5} - \Omega_{1,2}\rho_{2,5} + \Omega_{4,5}\rho_{1,4}\right) + \Lambda_{1,5}(\rho), \\
\dot{\rho}_{2,1} = \dot{\rho}^*_{1,2}, \\
\dot{\rho}_{2,2} = i\left(-\Omega_{1,2}\rho_{1,2} + \Omega_{1,2}\rho_{2,1} + \Omega_{2,3}\rho_{2,3} - \Omega_{2,3}\rho_{3,2}\right) + \Lambda_{2,2}(\rho), \\
\dot{\rho}_{2,3} = i\left(-\Delta_{2,3}\rho_{2,3} + \Omega_{2,3}\rho_{2,2} - \Omega_{2,3}\rho_{3,3} - \Omega_{1,2}\rho_{1,3} + \Omega_{3,4}\rho_{2,4}\right) + \Lambda_{2,3}(\rho), \\
\dot{\rho}_{2,4} = i\left(\Delta_{2,4}\rho_{2,4} - \Omega_{2,3}\rho_{3,4} - \Omega_{1,2}\rho_{1,4} + \Omega_{3,4}\rho_{2,3} + \Omega_{4,5}\rho_{2,5}\right) + \Lambda_{2,4}(\rho), \\
\dot{\rho}_{2,5} = i\left(\Delta_{2,5}\rho_{2,5} - \Omega_{2,3}\rho_{3,5} - \Omega_{1,2}\rho_{1,5} + \Omega_{4,5}\rho_{2,4}\right) + \Lambda_{2,5}(\rho), \\
\dot{\rho}_{3,1} = \dot{\rho}^*_{1,3}, \\
\dot{\rho}_{3,2} = \dot{\rho}^*_{2,3}, \\
\dot{\rho}_{3,3} = i\left(-\Omega_{2,3}\rho_{2,3} + \Omega_{2,3}\rho_{3,2} + \Omega_{3,4}\rho_{3,4} - \Omega_{3,4}\rho_{4,3}\right) + \Lambda_{3,3}(\rho), \\
\dot{\rho}_{3,4} = i\left(\Delta_{3,4}\rho_{3,4} + \Omega_{3,4}\rho_{3,3} - \Omega_{3,4}\rho_{4,4} - \Omega_{2,3}\rho_{2,4} + \Omega_{4,5}\rho_{3,5}\right) + \Lambda_{3,4}(\rho), \\
\dot{\rho}_{3,5} = i\left(\Delta_{3,5}\rho_{3,5} - \Omega_{3,4}\rho_{4,5} - \Omega_{2,3}\rho_{2,5} + \Omega_{4,5}\rho_{3,4}\right) + \Lambda_{3,5}(\rho), \\
\dot{\rho}_{4,1} = \dot{\rho}^*_{1,4}, \\
\dot{\rho}_{4,2} = \dot{\rho}^*_{2,4}, \\
\dot{\rho}_{4,3} = \dot{\rho}^*_{3,4}, \\
\dot{\rho}_{4,4} = i\left(-\Omega_{3,4}\rho_{3,4} + \Omega_{3,4}\rho_{4,3} + \Omega_{4,5}\rho_{4,5} - \Omega_{4,5}\rho_{5,4}\right) + \Lambda_{4,4}(\rho), \\
\dot{\rho}_{4,5} = i\left(-\Delta_{4,5}\rho_{4,5} + \Omega_{4,5}\rho_{4,4} - \Omega_{4,5}\rho_{5,5} - \Omega_{3,4}\rho_{3,5}\right) + \Lambda_{4,5}(\rho), \\
\dot{\rho}_{5,1} = \dot{\rho}^*_{1,5}, \\
\dot{\rho}_{5,2} = \dot{\rho}^*_{2,5}, \\
\dot{\rho}_{5,3} = \dot{\rho}^*_{3,5}, \\
\dot{\rho}_{5,4} = \dot{\rho}^*_{4,5}, \\
\dot{\rho}_{5,5} = i\left(-\Omega_{4,5}\rho_{4,5} + \Omega_{4,5}\rho_{5,4}\right) + \Lambda_{5,5}(\rho).
\end{cases}
\tag{2.34}
$$

2.4 Implementation of the atomic logical device

In this section, the possibility of a complete atomic population transfer from state $|1\rangle$ to state $|5\rangle$ [see Figure 2.4] in different regimes combined with scanning the frequency of laser pulses at the corresponding transitions, taking into account relaxation processes is numerically investigated. The comparison of population transfer using the frequency scanning technique with the results obtained using methods in which there is no scanning is carried out. Two types of scanning are considered. In the first case, the scanning of the atomic transition frequency is synchronized with the laser pulse, i.e. a certain transition is in resonance when the laser pulse has the biggest Rabi frequency. In the second case there is no synchronization, i.e. the frequency scanning of the atomic transition is fixed and does not depend on Rabi frequency.

Figure 2.5 shows the population dynamics when the atom interacts with four laser pulses

of a same duration and are switched on simultaneously. Moreover, two of them ($\Omega_{1,2}$ and $\Omega_{3,4}$) have a big, and the rest ($\Omega_{2,3}$ and $\Omega_{4,5}$) have a small Rabi frequency. Obviously there is no difference between synchronous and asynchronous scanning when all pulses are switched on at the same time.

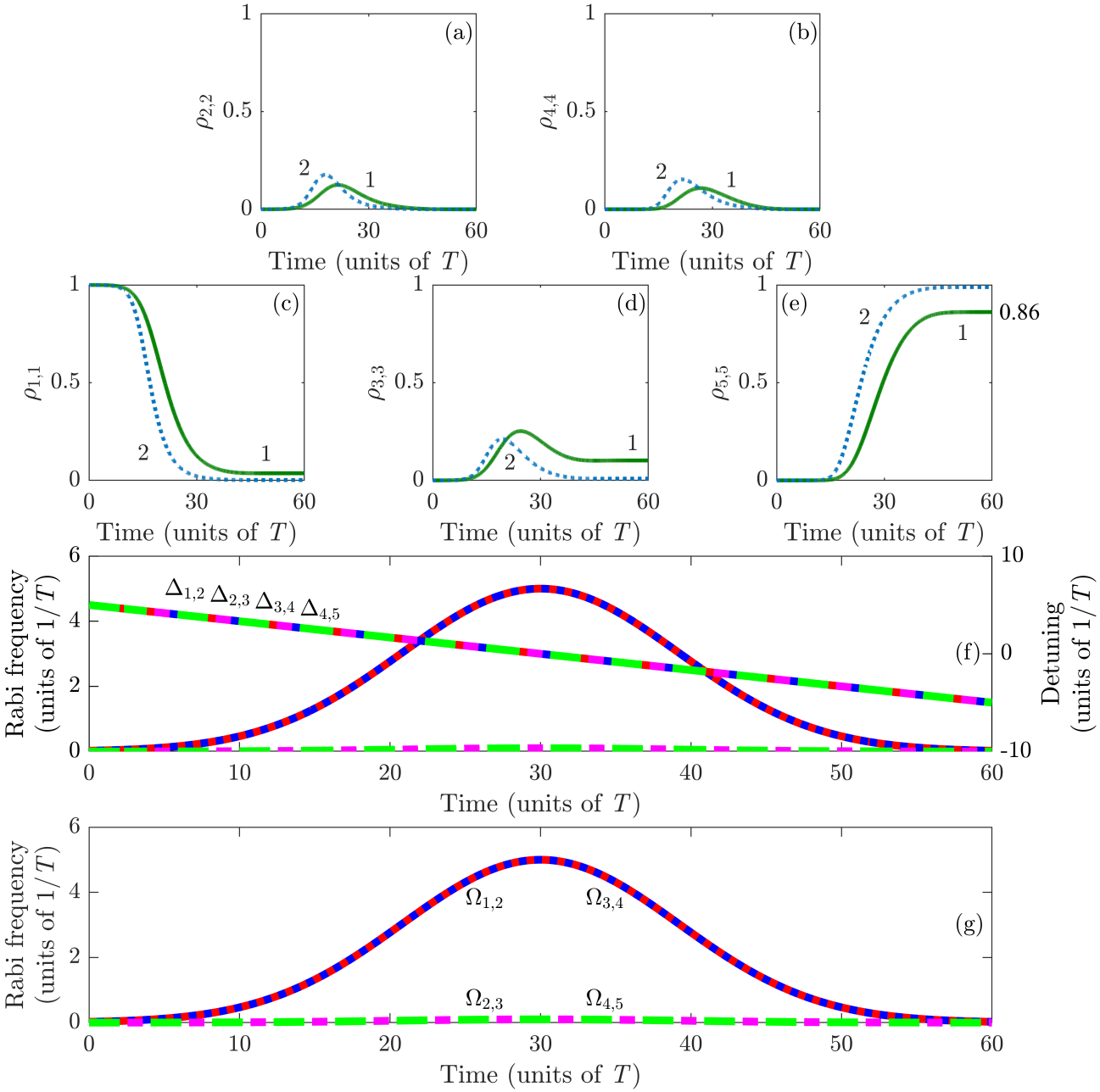

Figure 2.5: Comparison of the population dynamics of atomic levels (a, b, c, d, e): curves 1 without scanning (g) and curves 2 with scanning (f). The following values for the parameters in numerical calculations were used: $\Omega_{1,2} = \Omega_{3,4} = 5$, $\Omega_{2,3} = \Omega_{4,5} = 0.01$, $\delta = 5$ and $\Gamma_{i,j} = 0.5$. The peaks of all pulses correspond to the values $t_1 = t_2 = t_3 = t_4 = 30$. All parameters are normalized to the total scan time T.

On Figure 2.5 (c) and Figure 2.5 (e), continuous curve 1 describes the population transfer dynamics when scanning is not applied and, obviously the detuning for each transition from the corresponding resonant frequency is fixed: $\Delta_{1,2} = \Delta_{2,3} = \Delta_{3,4} = \Delta_{4,5} = 5$. Dotted curve

2 shows the dynamics of population transfer [59], when scanning is combined with the pulse regime and the detuning changes according to

$$\Delta_{n,n+1}(t) = \delta - \frac{2\delta}{T} \cdot t, \tag{2.35}$$

where δ is the scan amplitude and T is the total scan time. As can be seen from Figure 2.5, when scanning is applied, a complete transfer of populations occurs, and without scanning it is possible to transfer to state $|5\rangle$ only about 86 % of the entire population.

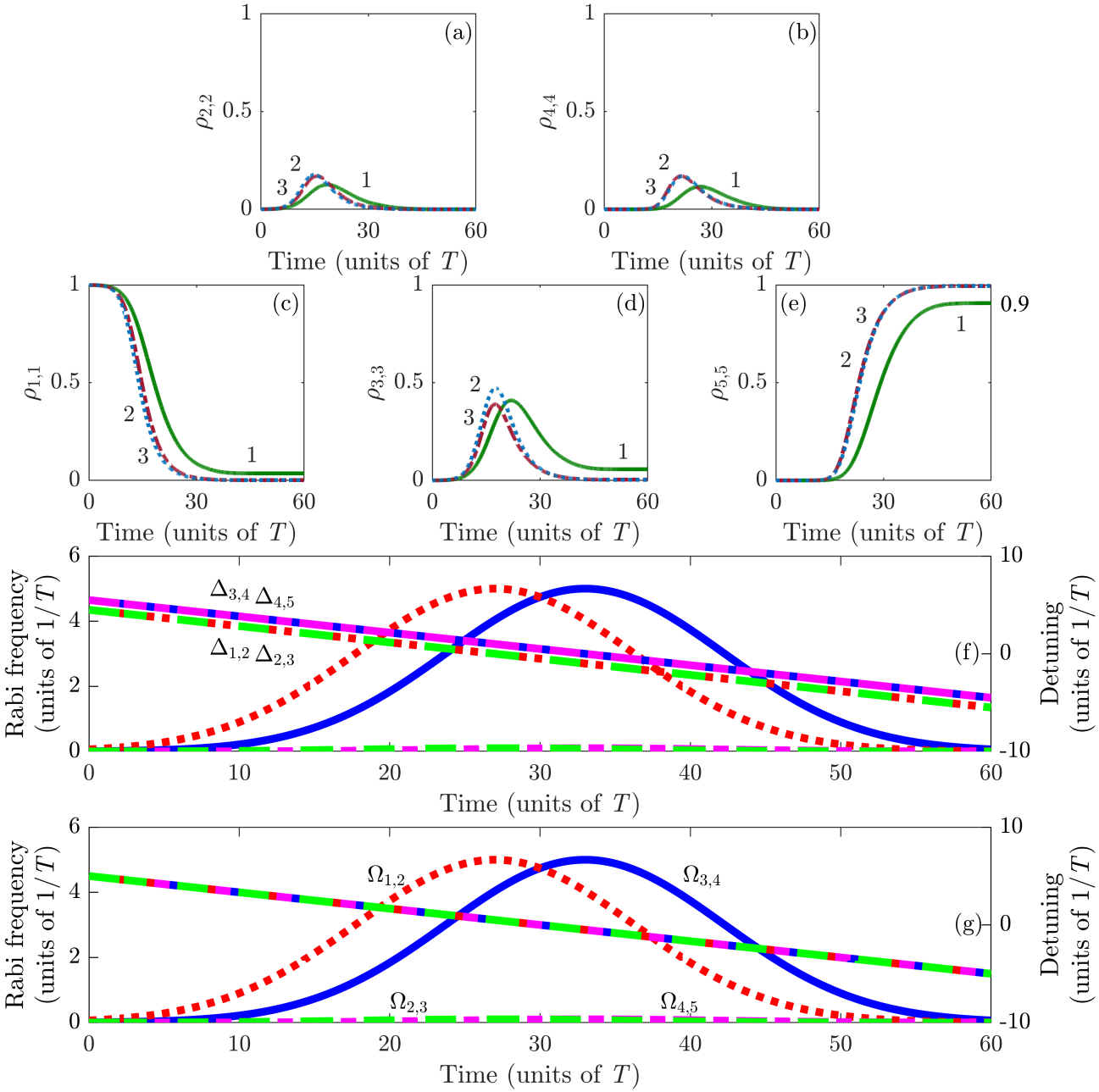

Figure 2.6: Comparison of the population dynamics of atomic levels (a, b, c, d, e): curves 1 without scanning, curves 2 with synchronous scanning (f) and curves 3 with asynchronous scanning (g). For the obtained results: $\Omega_{1,2} = \Omega_{3,4} = 5$, $\Omega_{2,3} = \Omega_{4,5} = 0.01$, $\delta = 5$ and $\Gamma_{i,j} = 0.5$. The peaks of pulses correspond to the values $t_1 = t_2 = 27$ and $t_3 = t_4 = 33$. All parameters are normalized to the total scan time T.

Figure 2.6 shows the dynamics of the transfer of atomic populations upon interaction with four pulses, of which one pair, $\Omega_{2,3}$ and $\Omega_{4,5}$, lags slightly behind the other pair $\Omega_{1,2}$ and $\Omega_{3,4}$ in time. In this case, there is a clear difference between synchronous and asynchronous scanning, that is, during synchronous scanning, the atom is never in three- and four-photon resonances. However, these detunings are small, and a complete transfer of populations from state $|1\rangle$ to state $|5\rangle$ takes place.

On Figure 2.6 (c) and Figure 2.6 (e), continuous curve 1 describes the dynamics of population transfer when there is no scanning and the atom is in exact two-photon resonances: $\Delta_{1,2} = \Delta_{2,3} = \Delta_{3,4} = \Delta_{4,5} = 5$. Dotted curve 2 shows the result for synchronous scanning and detuning can be written in the following form:

$$\Delta_{n,n+1}(t) = \delta - \frac{2\delta}{T} \cdot t - t_n + \frac{T}{2}, \tag{2.36}$$

where t_n corresponds to the time at which the corresponding laser pulse has the maximum Rabi frequency. Dashed curve 3 (asynchronous scanning) is obtained when the detuning corresponds to formula (2.35). One can mention, that the results for synchronous and asynchronous scanning are the same, and a complete transfer of populations can be performed. Without scanning, only about 90 % of the entire population can be transferred to state $|5\rangle$.

On Figure 2.7 and Figure 2.8, sub-figures (c) and (e), continuous curve 1 shows the population dynamics that was obtained using Gaussian pulses without scanning. Dotted curve 2 and dashed curve 3 show the population dynamics obtained using the same Gaussian pulses combined with scanning. Curve 2 corresponds to synchronous scanning, which is shown on sub-figure (f), and curve 3 is obtained in the case of asynchronous scanning (g). For the curve 1 the detunings have the following values: $\Delta_{1,2} = \Delta_{3,4} = 5$ and $\Delta_{2,3} = \Delta_{4,5} = -5$. For the curve 2 the detunings can be represented as follows:

$$\Delta_{n,n+1}(t) = (-1)^{n+1} \cdot \left(\delta - \frac{2\delta}{T} \cdot t - t_n + \frac{T}{2} \right), \tag{2.37}$$

and curve 3 corresponds to the following formula for the detuning:

$$\Delta_{n,n+1}(t) = (-1)^{n+1} \cdot \left(\delta - \frac{2\delta}{T} \cdot t \right) \tag{2.38}$$

with $n = 1, 2, 3, 4$.

Figure 2.7 shows the dynamics of population transfer using a counter-intuitive sequence of pulses, where $\Omega_{2,3}$, $\Omega_{1,2}$ and $\Omega_{4,5}$, $\Omega_{3,4}$ are pair pulses. This configuration of laser pulses, when scan technique is not applied, results to a transfer of 46 % of the initial population. The use of counter-intuitive configurations, which are combined with synchronous scanning, leads to a complete transfer of populations from state $|1\rangle$ to state $|5\rangle$, and with asynchronous scanning, 95 % of the population can be transferred.

On Figure 2.7 (f), the atom is in two-photon resonances for a short time, but despite this, the scanning technique allows efficient population transfer, and in asynchronous scanning

[see Figure 2.7 (g)] the transition frequencies corresponding to $\Omega_{2,3}$ and $\Omega_{3,4}$, are in single-photon resonances when certain Rabi frequencies are relatively low, which leads to a deterioration in population transfer, compared to the case when synchronous scanning was used.

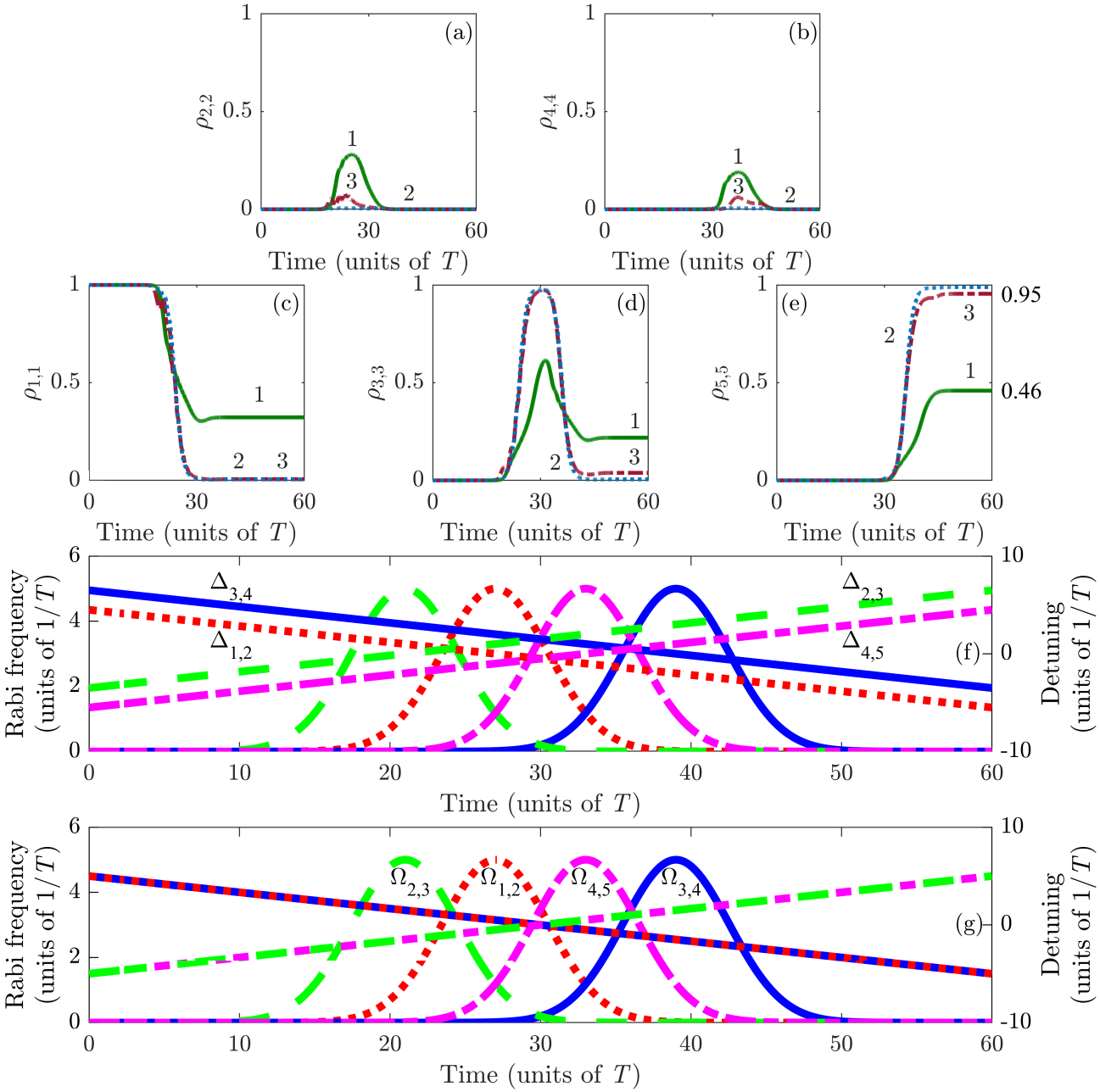

Figure 2.7: Comparison of the population dynamics of atomic levels (a, b, c, d, e): curves 1 without scanning, curves 2 with synchronous scanning (f), curves 3 with asynchronous scanning (g). Values of the parameters are the following: $\Omega_{1,2} = \Omega_{2,3} = \Omega_{3,4} = \Omega_{4,5} = 5$. The peaks of pulses correspond to the values $t_1 = 27$, $t_2 = 21$, $t_3 = 39$, $t_4 = 33$, $\delta = 5$ and $\Gamma_{i,j} = 0.5$. All parameters are normalized to the total scan time T.

Figure 2.8 shows the dynamics of population transfer upon interaction with two long-duration pulses and a relatively low Rabi frequency ($\Omega_{2,3}$, $\Omega_{3,4}$), and with two short-duration pulses and a high Rabi frequency ($\Omega_{1,2}$, $\Omega_{4,5}$). When scanning is not applied, we have only 54 % of the population transferred to the state $|5\rangle$. The use of laser pulses, which are combined with

the scanning technique, leads to a complete transfer of population from state $|1\rangle$ to state $|5\rangle$.

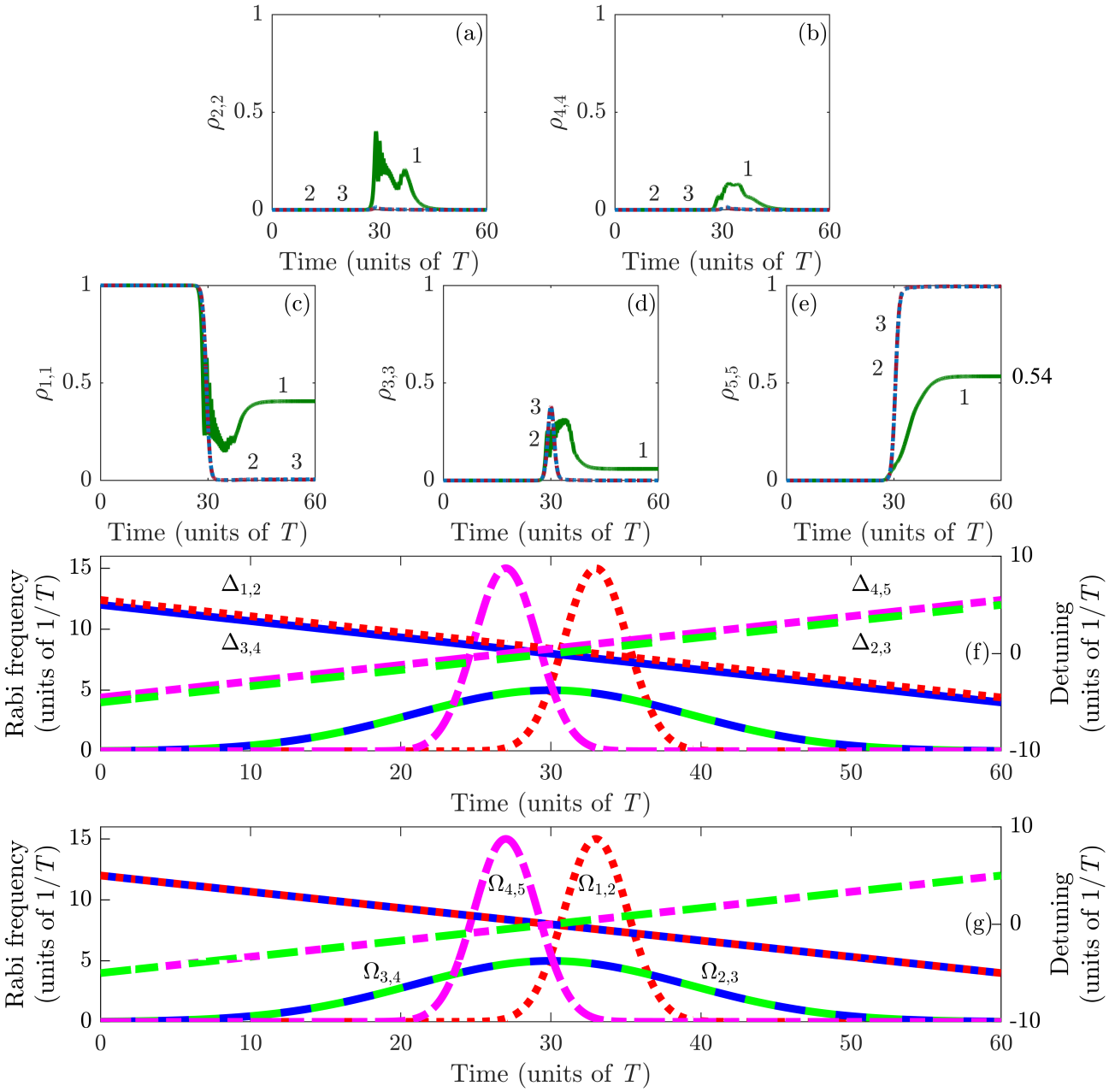

Figure 2.8: Comparison of the population dynamics of atomic levels (a, b, c, d, e): curves 1 without scanning, curves 2 with synchronous scanning (f) and curves 3 with asynchronous scanning (g). For the obtained results: $\Omega_{1,2} = \Omega_{4,5} = 15$, $\Omega_{2,3} = \Omega_{3,4} = 5$, $\delta = 5$ and $\Gamma_{i,j} = 0.5$. The peaks of pulses correspond to the values $t_1 = 27$, $t_2 = t_3 = 30$ and $t_4 = 33$. All parameters are normalized to the total scan time T.

2.5 Implementation of the Toffoli and Fredkin atomic universal logical gates

The figures presented in this section show the results of the numerical solution of the problem for the Toffoli and Fredkin gates. Pulses of the same duration are used. It is important to

note, that we chose the detunings such that single- and three-photon resonant transitions do not exist during the whole process of population transfer, but our system is in two- and four-photon resonances for every moment of the process. It is done to minimize the population of excited levels $|2\rangle$ and $|4\rangle$ in intermediate processes. To implement this kind of gates on alkali atoms' magnetic sublevels, we need to consider non-zero values for $\Lambda_{1,5}(\rho)$ and $\Lambda_{5,1}(\rho)$ [see formula 2.33], which mix the population of the states $|1\rangle$ and $|5\rangle$ over time. We recall that the relaxation matrix is diagonal symmetrical [63], thus values for both elements are the same:

$$\Lambda_{1,5}(\rho) = \Lambda_{5,1}(\rho) = \gamma_1 + \gamma_2 - \frac{\Gamma_{2,1} + \Gamma_{4,5}}{2}. \tag{2.39}$$

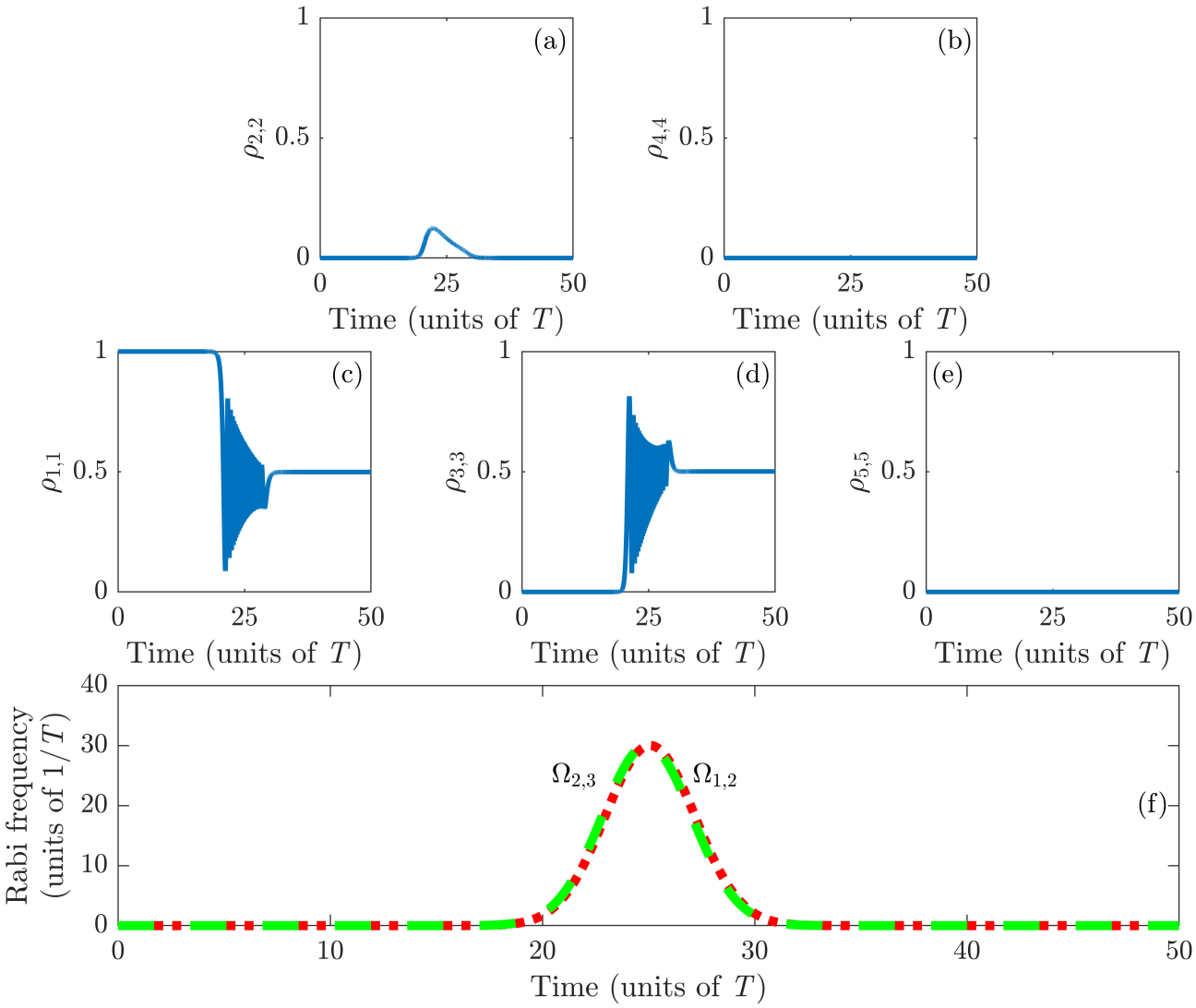

Figure 2.9: Dynamics of the populations of atomic levels (a, b, c, d, e) and the sequence of switching on of laser pulses (f). This sequence of pulses is used to prepare the considered atomic system for the Toffoli and Fredkin gate implementation. All parameters are normalized to the average pulse duration T.

To prepare our system for the reversible Toffoli and Fredkin atomic gate implementation, we need to do a simple operation on the atom. Let us assume, that the atoms' initial distribution of

populations [see Figure 2.9] at the levels $|1\rangle$, $|3\rangle$ and $|5\rangle$ are equal to $\rho_{1,1}(-\infty) = 1$, $\rho_{3,3}(-\infty) = 0$ and $\rho_{5,5}(-\infty) = 0$ respectively. Here we need to use only two pulses: $\Omega_{1,2}$ and $\Omega_{2,3}$, where the first pulse switches on after the second one. These pulses are responsible for the redistribution of populations between the states $|1\rangle$ and $|3\rangle$. At the end of the atom-laser field interaction, the populations of atomic levels are equal to $\rho_{1,1}(+\infty) = 1/2$, $\rho_{3,3}(+\infty) = 1/2$ and $\rho_{5,5}(+\infty) = 0$ (this corresponds to the inputs 1 1 0 of Tables 2.1 and 2.2). So, by doing only this operation we are able to prepare our atomic system for both Toffoli and Fredkin gates implementation. The numerical computations are done using the following values of the parameters: $\Delta_1 = \Delta_2 = 10$, $\Omega_{1,2} = \Omega_{2,3} = 30$, $\Gamma_{i,j} = 0.5$ and $t_1 = 25.07$, $t_2 = 24.93$.

On Figure 2.10, the pulses $\Omega_{2,3}$ and $\Omega_{1,2}$, which are responsible for the redistribution of populations between levels $|1\rangle$ and $|3\rangle$ are first switched on. Then pulses $\Omega_{4,5}$ and $\Omega_{3,4}$, which are responsible for the redistribution of populations between levels $|3\rangle$ and $|5\rangle$ are switched on.

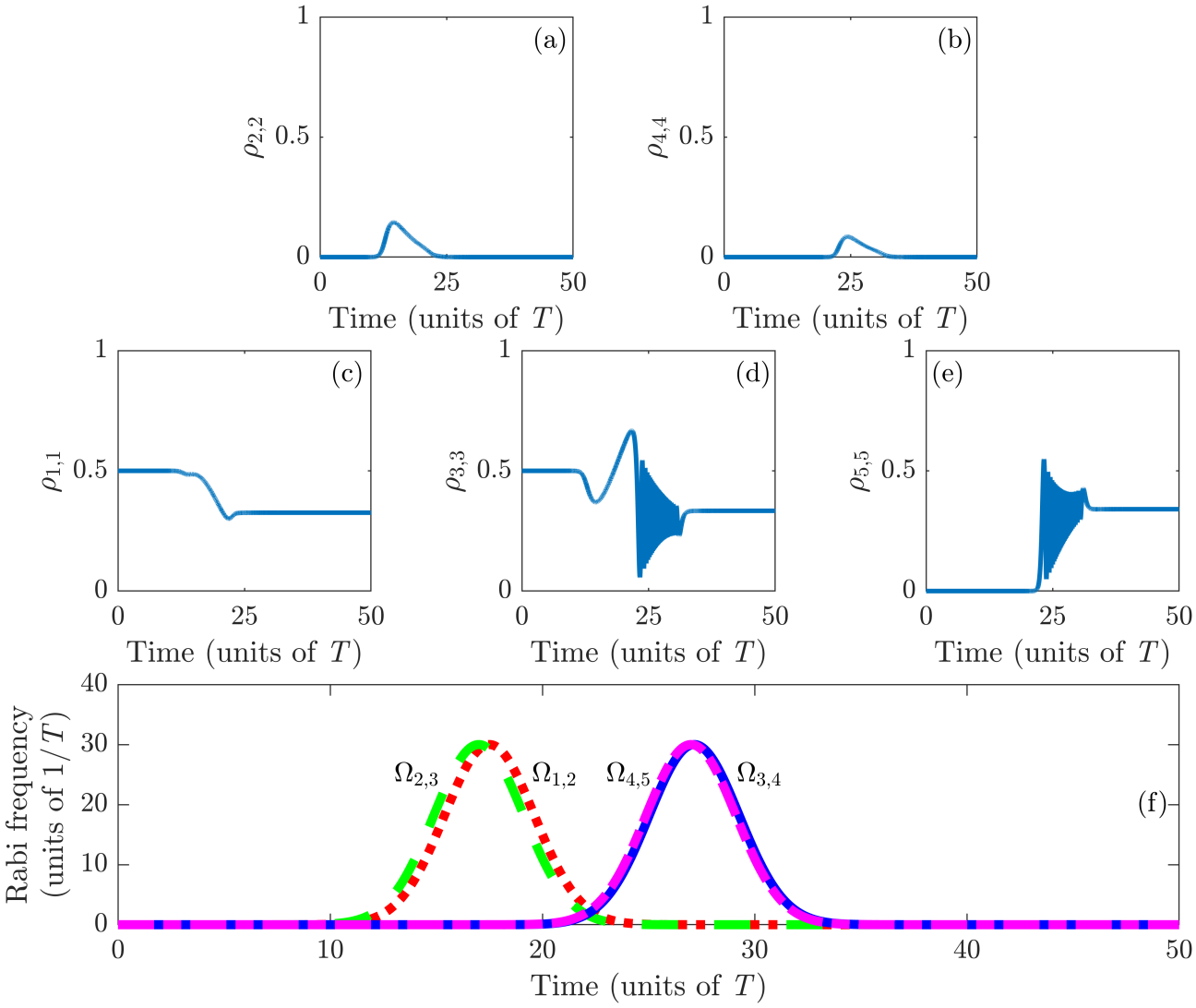

Figure 2.10: Dynamics of the populations of atomic levels (a, b, c, d, e) and the sequence of switching on of laser pulses (f). This corresponds to input 1 1 0 and the output 1 1 1 of the Toffoli gate. All parameters are normalized to the average pulse duration T.

The initial distributions of populations at the levels $|1\rangle$, $|3\rangle$ and $|5\rangle$ are equal to $\rho_{1,1}(-\infty) =$

1/2, $\rho_{3,3}(-\infty) = 1/2$ and $\rho_{5,5}(-\infty) = 0$, respectively (it corresponds to the initial input 1 1 0 of Table 2.1), and at the end of the interaction process, the populations of atomic levels are equal to $\rho_{1,1}(+\infty) = 1/3$, $\rho_{3,3}(+\infty) = 1/3$ and $\rho_{5,5}(+\infty) = 1/3$ (it corresponds to the output 1 1 1 of Table 2.1). The numerical computations were carried out at the following values of the parameters (all parameters are normalized to some average duration T): $\Delta_1 = \Delta_2 = \Delta_3 = \Delta_4 = 10$, $\Omega_{1,2} = \Omega_{2,3} = \Omega_{3,4} = \Omega_{4,5} = 30$, $\Gamma_{i,j} = 0.5$ and $t_1 = 17.5$, $t_2 = 17$, $t_3 = 27.15$, $t_4 = 27$.

To show the reversibility of the Toffoli gate implemented on the alkali atom, we need to consider the population transfer according to the 8^{th} row of the truth table of CCNOT gate [see Table 2.1]. It is obvious, that the laser pulses should be switched on in a reversed order (compared with the sequence of laser pulses depicted on Figure 2.10) to achieve our goal.

On Figure 2.11, the pulses are switched on in the reversed order.

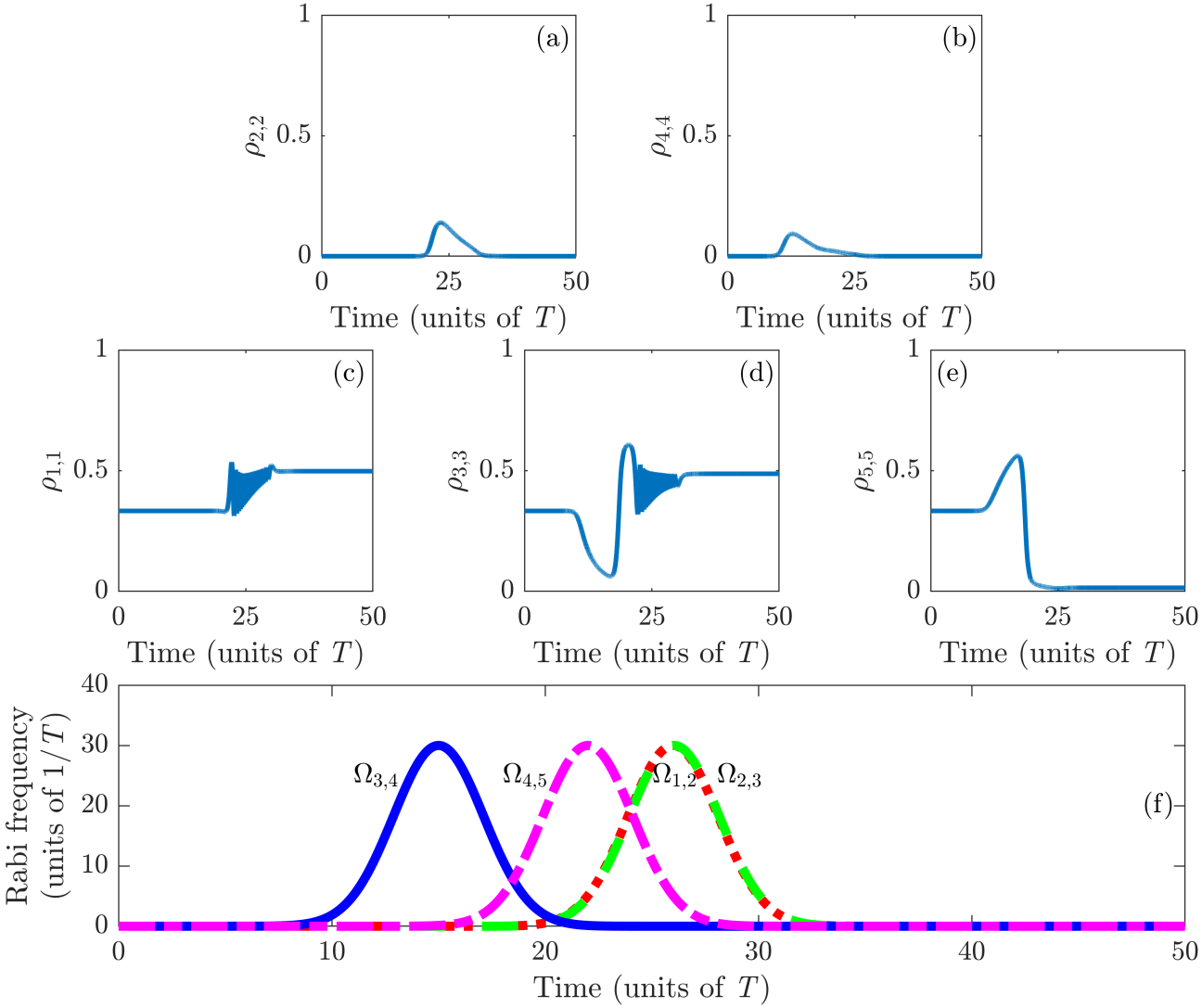

Figure 2.11: Dynamics of the populations of atomic levels (a, b, c, d, e) and the sequence of switching on of laser pulses (f). This corresponds to input 1 1 1 and the output 1 1 0 of the Toffoli gate. All parameters are normalized to the average pulse duration T.

First, the pulses $\Omega_{3,4}$ and $\Omega_{4,5}$ are switched on, which are responsible for the redistribution of populations between the levels $|3\rangle$ and $|5\rangle$. Then the pulses $\Omega_{1,2}$ and $\Omega_{2,3}$ are switched

on, which are responsible for the redistribution of populations between levels $|1\rangle$ and $|3\rangle$. The initial distributions of the populations at the levels $|1\rangle$, $|3\rangle$ and $|5\rangle$ are equal to $\rho_{1,1}(-\infty) = 1/3$, $\rho_{3,3}(-\infty) = 1/3$ and $\rho_{5,5}(-\infty) = 1/3$, respectively (it corresponds to the initial input 1 1 1 of Table 2.1), and at the end of the process we obtain $\rho_{1,1}(+\infty) = 1/2$, $\rho_{3,3}(+\infty) = 1/2$ and $\rho_{5,5}(+\infty) = 0$ (it corresponds to the output 1 1 0 of Table 2.1). For this result, the parameter values are $\Delta_1 = \Delta_2 = \Delta_3 = \Delta_4 = 10$, $\Omega_{1,2} = \Omega_{2,3} = \Omega_{3,4} = \Omega_{4,5} = 30$, $\Gamma_{i,j} = 0.5$; the dimensionless pulse peaks are corresponding to the following values: $t_1 = 26$, $t_2 = 26.05$, $t_3 = 15$, $t_4 = 22$.

From now on we will show the implementation of reversible atomic Fredkin gate on a M-system. As it has one control bit, which corresponds to the state $|1\rangle$, it is simpler to implement this reversible gate. In fact instead of four laser pulses we need only two of them: $\Omega_{3,4}$ and $\Omega_{4,5}$, which are responsible for the redistribution of populations between levels $|3\rangle$ and $|5\rangle$ (so-called the target bits).

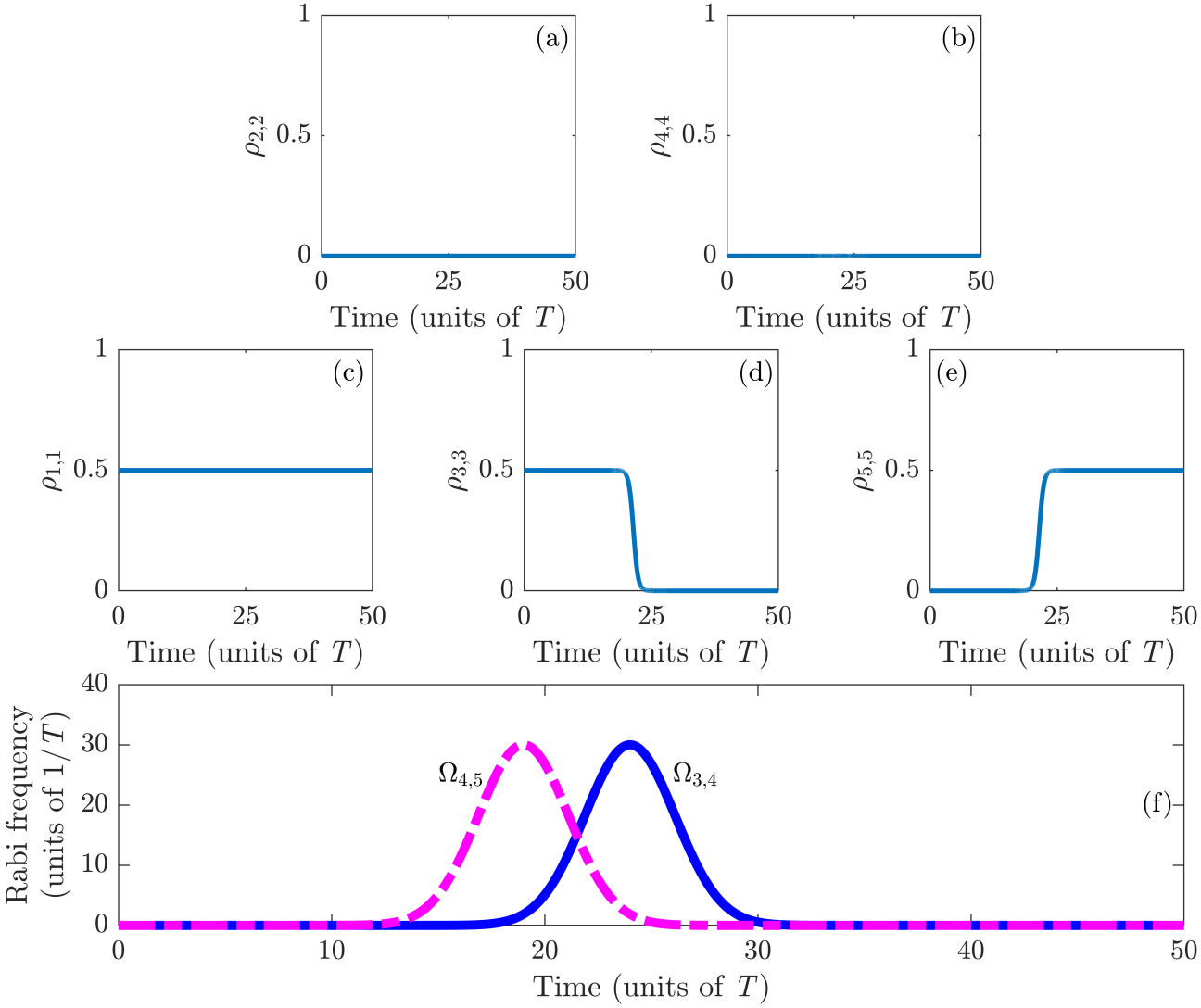

Figure 2.12: Dynamics of the populations of atomic levels (a, b, c, d, e) and the sequence of switching on of laser pulses (f). This corresponds to input 1 1 0 and the output 1 0 1 of the Fredkin gate. All parameters are normalized to the average pulse duration T.

On Figure 2.12, firstly the laser pulse $\Omega_{4,5}$ is switched on, and then the pulse $\Omega_{3,4}$ is turned on. Initial populations of the levels $|1\rangle$, $|3\rangle$ and $|5\rangle$ are $\rho_{1,1}(-\infty) = 1/2$, $\rho_{3,3}(-\infty) = 1/2$ and $\rho_{5,5}(-\infty) = 0$ (it corresponds to the initial input 1 1 0 of Table 2.2). At the end of the interaction process, the populations are equal to $\rho_{1,1}(+\infty) = 1/2$, $\rho_{3,3}(+\infty) = 0$ and $\rho_{5,5}(+\infty) = 1/2$ (it corresponds to the output 1 0 1 of Table 2.2). These results were obtained for the following values of the parameters: $\Delta_3 = \Delta_4 = 10$, $\Omega_{3,4} = \Omega_{4,5} = 30$, $\Gamma_{i,j} = 0.5$, $t_3 = 24$ and $t_4 = 19$.

As in the case of Toffoli gate [see Figures 2.10 and 2.11], here too, to show the implementation of the 7$^{\text{th}}$ row of Table 2.2, we need to use the reverse order of laser pulses applied on the system depicted on Figure 2.12.

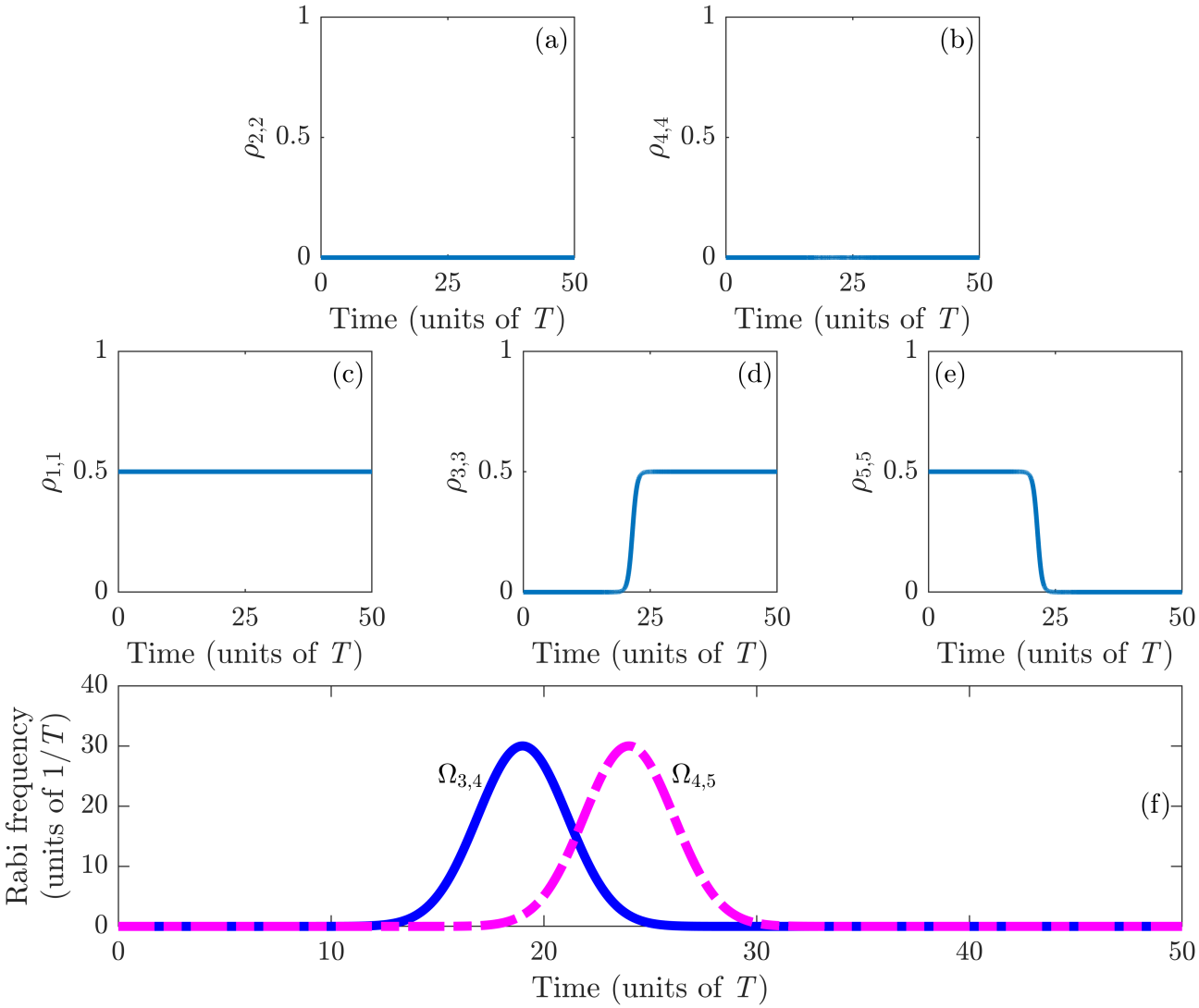

Figure 2.13: Dynamics of the populations of atomic levels (a, b, c, d, e) and the sequence of switching on of laser pulses (f). This corresponds to input 1 1 0 and the output 1 0 1 of the Fredkin gate. All parameters are normalized to the average pulse duration T.

On Figure 2.13, firstly the pulse $\Omega_{3,4}$ is turned on, then the laser pulse $\Omega_{4,5}$ is switched on. The initial population of levels $|1\rangle$, $|3\rangle$, and $|5\rangle$ are equal to $\rho_{1,1}(-\infty) = 1/2$, $\rho_{3,3}(-\infty) = 0$ and $\rho_{5,5}(-\infty) = 1/2$ (it corresponds to the initial input 1 0 1 in Table 2.2), and at the end of the process of interaction, the populations are equal to $\rho_{1,1}(+\infty) = 1/2$, $\rho_{3,3}(+\infty) = 1/2$ and

$\rho_{5,5}(+\infty) = 0$ (it corresponds to the output 1 1 0 of Table 2.2). These results are obtained at the following values of parameters: $\Delta_3 = \Delta_4 = 10$, $\Omega_{3,4} = \Omega_{4,5} = 30$, $\Gamma_{i,j} = 0.5$, $t_3 = 19$ and $t_4 = 24$.

2.6 Conclusion

In this chapter the dynamics of atomic population transfer in a five-level M-type system, which interacts with four Gaussian laser pulses is studied in detail. The analysis is based on the non-stationary solution of the equations for the density matrix, which takes into account both the relaxation processes and the various sequences of the switching on of the laser pulses of arbitrary duration. A comparison of the population transfer using different sequences of laser pulses combined with the scanning technique is made. From the obtained results it is obvious that the scanning technique leads to a complete population transfer, despite the fact that the atom may not be in a resonance throughout the entire interaction time. In other words, it is not necessary to know the exact resonance of a certain atomic transition and to tune the laser for it, but it is only necessary to tune the laser close to the resonance frequency of the atomic transition. The proposed method, which allows us to make a full population transfer in a very simple way, can serve as a base in the construction of atomic logical devices. The possibility of realization of programmable logic gates is demonstrated using the different sequences of laser pulses. The realization of logic gates is based on the reversible cyclic transfer of atomic populations. It is shown that with the use of short pulses (up to values $\Gamma T \sim 1$) the reversibility of population transfer is preserved.

The considered scheme can be experimentally realized, for example, on atomic sublevels of alkali-metals in a magnetic field or on the electronic terms of an atom. As this chapter is purely theoretical, thus giving orienting, indicative values for experimenters can make this chapter more clear for the realization of logical atomic devices from the experimental point of view. For example in the case of ^{87}Rb, using a laser pulse of 25 ns duration the Rabi frequency value is equal to the natural linewidth of this isotope: $2\pi \times 6.06$ MHz, which is an acceptable value.

The results obtained in this chapter are partly published in references [31] and [35].

Chapter 3

Rubidium Vapor Fluorescence in a Transient Interaction Regime

3.1 Introduction

Resonant interaction of narrow-linewidth cw laser radiation with atomic vapors of alkali-metals has been intensely studied in the past decades, driven by fundamental interest and emerging important applications. Most of these studies deal with a steady state regime of interaction of atomic ensemble with resonant light required for establishment of the relevant processes.

To the best of our knowledge, there are just a few works on atomic spectroscopy with cw excitation radiation where transient resonant interaction processes are studied. Particularly, theoretical and experimental investigations of processes under dynamic excitation of atomic media with modulated cw laser radiation were done for nonlinear magneto-optical processes [75], saturation spectroscopy [76], four-wave mixing [77], and coherent population trapping [78, 79]. Analytical solutions of temporal evolution of populations in optically pumped atoms were obtained in Ref. [80]. Besides transient processes imposed by temporally modulated laser radiation, dynamic effects were studied also for spatial Ramsey schemes, such as dark Raman resonances caused by interference [81].

When laser radiation frequency is tuned to an atomic transition, the atom can undergo many cycles of absorption and emission that eventually lead to establishment of the steady-state atomic response. There are two main factors that determine interaction time of an individual atom with the laser field in conventional atomic spectroscopy experiments. First, the interaction time can be limited by a time of flight (TOF) of an atom through a laser beam. For the room-temperature alkali vapor, the mean atomic velocity is $\sim$ 200 m/s, and for the 1 mm diameter laser beam, the TOF of an atom crossing the laser beam at a 90° angle is $\tau_{\mathrm{TOF}} = 5$ µs. Second, the interaction time can be determined by the temporal rate of linear scanning of laser radiation frequency employed in many experiments. For example, when scanning the $\Delta\omega_L = 2\pi \times 10$ GHz frequency interval around the resonance line by applying triangular modulation pulses with repetition frequency of $f_s = 50$ Hz, the interaction time of

an individual atom with $\gamma_{\text{nat}} = 2\pi \times 6.07$ MHz natural linewidth is

$$\tau_s = \frac{\gamma_{\text{nat}}}{2 f_s \Delta\omega_L} \approx 6\ \mu\text{s}. \tag{3.1}$$

In most spectroscopic experiments, the scanning is slow enough, so that the interaction time is restricted by a flight time.

Besides the above-mentioned physical limitations, the resonant interaction of atom with the laser field is governed by the laser electric field amplitude $\boldsymbol{E}$ and atomic transition dipole moment $\boldsymbol{d_{i,j}}$, characterized by a Rabi frequency $\Omega_{i,j} = \dfrac{\boldsymbol{d_{i,j}}\boldsymbol{E}}{\hbar}$. The corresponding experimental (measurable) parameter is laser radiation intensity I_L:

$$I_L = \frac{1}{2}\epsilon_0 nc|\boldsymbol{E}|^2 = \frac{\epsilon_0 nc\hbar^2\Omega_{i,j}^2}{d_{i,j}^2}, \tag{3.2}$$

where ϵ_0 is the vacuum permittivity, and n is the refractive index. Taking into account possible detuning Δ of the laser radiation frequency from the atomic transition (including also the spectral linewidth of laser radiation when it exceeds γ_{nat}), generalized (effective) Rabi frequency should be considered [68]:

$$\widetilde{\Omega}_{i,j} = \sqrt{\Omega_{i,j}^2 + \Delta^2}. \tag{3.3}$$

The study of transient effects in resonant interaction of cw laser radiation with atomic media is of practical interest for two reasons. First, as seen from the abovementioned, it can be used for determination of experimental parameters such as relaxation rates. Second, dynamic transient processes can be utilized for heralded control of population in atomic systems, resembling excitation by π and $\pi/2$ pulses in a Rabi cycle. Studies of transient processes involving fluorescence spectra are of particular interest, since the fluorescence can serve as a direct measure of population of excited atomic states.

In this chapter, we present the results of theoretical and experimental studies of Rb D_2 line fluorescence spectra while changing the rate of linear scanning of laser radiation frequency by four orders of magnitude. Fluorescence signal is merely dependent on the population of excited atomic states, exhibiting linear dependence; moreover, as compared with absorption spectra, the fluorescence spectra appear on a zero-background level, which facilitates treatment and simulation of the measurement results. Our primary aim was to determine the most appropriate temporal conditions for efficient atomic population control. Also, we were aimed at determination of important relaxation parameters of the atomic system based on the fitting of experimental results by our theoretical model.

3.2 Theoretical model, describing ^{85}Rb and ^{87}Rb atom D_2 line − laser field interaction

We employ a density matrix model written in the Chapter 2, Section 2.2 to simulate the resonant fluorescence on hyperfine transitions ^{85}Rb $F_g = 2, 3 \rightarrow F_e = 1, 2, 3, 4$ and ^{87}Rb

$F_g = 1, 2 \rightarrow F_e = 0, 1, 2, 3$ of the atomic D_2 line [see Figure 3.1 (a)], developed upon excitation of the atomic system by laser radiation with a frequency scanned across the hyperfine transitions manifold [see the system diagram in Figure 3.1 (b)].

For this system, the time-dependent Liouville-von Neumann equation reads

$$\frac{d\rho}{dt} = -\frac{i}{\hbar}[H, \rho] - R(\rho), \tag{3.4}$$

where ρ is 6×6 dimensional density matrix with diagonal elements $\rho_{i,i}(t)$ representing the population of $|i\rangle$-th state, and off-diagonal elements $\rho_{i,j}(t)$ representing coherences linked with $|i\rangle \rightarrow |j\rangle$ transitions, H is the Hamiltonian of the system, and $R(\rho)$ is the relaxation matrix. As we deal with the non-stationary (transient) interaction regime caused by fast frequency scanning, we consider a time-dependent problem. The initial condition for Eq. (3.4) is $\rho_{1,1}(0) + \rho_{2,2}(0) = 1$. Taking into account the magnetic sublevels manifold, the initial ground state populations are $\rho_{1,1}(0) = 5/12$, $\rho_{2,2}(0) = 7/12$ for ^{85}Rb, and $\rho_{1,1}(0) = 3/8$, $\rho_{2,2}(0) = 5/8$ for ^{87}Rb [82, 83].

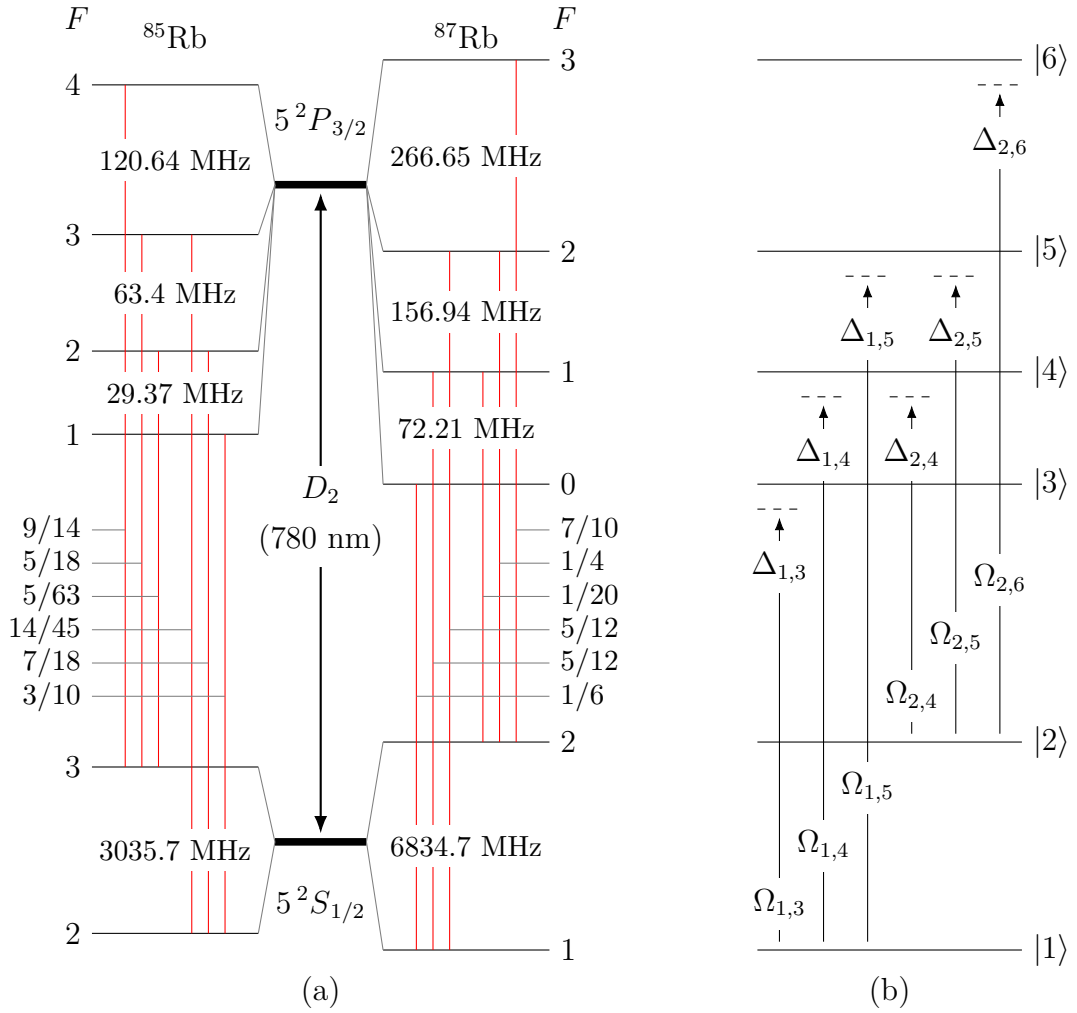

Figure 3.1: a) Hyperfine structure of rubidium D_2 line and individual optical transitions for ^{85}Rb [82] and ^{87}Rb [83] with indicated relative strengths. b) Scheme of the theoretical model with notations of the parameters.

The time-dependent Hamiltonian has the following form:

$$H(t) = \begin{pmatrix} 0 & 0 & \Omega_{1,3}e^{-i\Delta_{1,3}t} & \Omega_{1,4}e^{-i\Delta_{1,4}t} & \Omega_{1,5}e^{-i\Delta_{1,5}t} & 0 \\ 0 & 0 & 0 & \Omega_{2,4}e^{-i\Delta_{2,4}t} & \Omega_{2,5}e^{-i\Delta_{2,5}t} & \Omega_{2,6}e^{-i\Delta_{2,6}t} \\ \Omega_{1,3}e^{i\Delta_{1,3}t} & 0 & 0 & 0 & 0 & 0 \\ \Omega_{1,4}e^{i\Delta_{1,4}t} & \Omega_{2,4}e^{i\Delta_{2,4}t} & 0 & 0 & 0 & 0 \\ \Omega_{1,5}e^{i\Delta_{1,5}t} & \Omega_{2,5}e^{i\Delta_{2,5}t} & 0 & 0 & 0 & 0 \\ 0 & \Omega_{2,6}e^{i\Delta_{2,6}t} & 0 & 0 & 0 & 0 \end{pmatrix}, \quad (3.5)$$

where $\Omega_{i,j} = \dfrac{\boldsymbol{d_{i,j}E}}{\hbar}$ are the matrix elements of the Rabi frequency with $d_{i,j}$ the matrix elements of the dipole moment for the respective transitions [82,83], E is the amplitude of classical electric field interacting with the atomic media of ^{85}Rb and ^{87}Rb, $\Delta_{i,j}$ are one-photon detunings of the scanning laser field from atomic resonances and are a function of time. For periodic triangular temporal modulation of the laser radiation frequency, we can write

$$\Delta_{i,j} = \Delta^0_{i,j} + \frac{\Delta}{\pi}\arcsin(\cos 2\pi f_s t), \quad (3.6)$$

where Δ is the spectral range of scanning, f_s is the triangular modulation frequency, $i = 1, 2$, and $j = 3, 4, 5, 6$ [see Figure 3.1 (b)]. Employing this modulation, the radiation frequency will linearly increase/decrease in time, so that the laser field will be consecutively in resonance with all the groups of transitions: ^{87}Rb $F_g = 2 \to F_e = 1, 2, 3$, ^{85}Rb $F_g = 3 \to F_e = 2, 3, 4$, ^{85}Rb $F_g = 2 \to F_e = 1, 2, 3$ and ^{87}Rb $F_g = 1 \to F_e = 0, 1, 2$, in direct (rising frequency) and reverse (falling frequency) orders.

The relaxation matrix $R(\rho)$ involves all the relaxation processes in the system:

$$R(\rho) = \begin{pmatrix} \Gamma^{(1,1)} & (\gamma_0+\gamma_{tot})\rho_{1,2} & \gamma_{tot}\rho_{1,3} & \gamma_{tot}\rho_{1,4} & \gamma_{tot}\rho_{1,5} & \gamma_{tot}\rho_{1,6} \\ (\gamma_0+\gamma_{tot})\rho_{2,1} & \Gamma^{(2,2)} & \gamma_{tot}\rho_{2,3} & \gamma_{tot}\rho_{2,4} & \gamma_{tot}\rho_{2,5} & \gamma_{tot}\rho_{2,6} \\ \gamma_{tot}\rho_{3,1} & \gamma_{tot}\rho_{3,2} & \Gamma^{(3,3)} & \gamma_{tot}\rho_{3,4} & \gamma_{tot}\rho_{3,5} & \gamma_{tot}\rho_{3,6} \\ \gamma_{tot}\rho_{4,1} & \gamma_{tot}\rho_{4,2} & \gamma_{tot}\rho_{4,3} & \Gamma^{(4,4)} & \gamma_{tot}\rho_{4,5} & \gamma_{tot}\rho_{4,6} \\ \gamma_{tot}\rho_{5,1} & \gamma_{tot}\rho_{5,2} & \gamma_{tot}\rho_{5,3} & \gamma_{tot}\rho_{5,4} & \Gamma^{(5,5)} & \gamma_{tot}\rho_{5,6} \\ \gamma_{tot}\rho_{6,1} & \gamma_{tot}\rho_{6,2} & \gamma_{tot}\rho_{6,3} & \gamma_{tot}\rho_{6,4} & \gamma_{tot}\rho_{6,5} & \Gamma^{(6,6)} \end{pmatrix}, \quad (3.7)$$

where the following notations are used:

$$\begin{aligned} \Gamma^{(1,1)} &= \gamma_0(\rho_{1,1} - \rho^0_{1,1}) - \Gamma_{3,1}\rho_{3,3} - \Gamma_{4,1}\rho_{4,4} - \Gamma_{5,1}\rho_{5,5}, \\ \Gamma^{(2,2)} &= \gamma_0(\rho_{2,2} - \rho^0_{2,2}) - \Gamma_{4,2}\rho_{4,4} - \Gamma_{5,2}\rho_{5,5} - \Gamma_{6,2}\rho_{6,6}, \\ \Gamma^{(3,3)} &= (\Gamma_{3,1} + \gamma_0)\rho_{3,3}, \\ \Gamma^{(4,4)} &= (\Gamma_{4,1} + \Gamma_{4,2} + \gamma_0)\rho_{4,4}, \\ \Gamma^{(5,5)} &= (\Gamma_{5,1} + \Gamma_{5,2} + \gamma_0)\rho_{5,5}, \\ \Gamma^{(6,6)} &= (\Gamma_{6,2} + \gamma_0)\rho_{6,6}. \end{aligned}$$

Here $\Gamma_{i,j}$ is the natural decay rate of the corresponding excited state; γ_0 is the relaxation rate of the lower energy levels to the equilibrium isotropic state [79]; γ_{tot} is the total broadening rate comprising radiative damping, collisional broadening, laser radiation linewidth, and inhomogeneous (Doppler) broadening making a dominant contribution ($\gamma_{tot} \approx \gamma_{\mathrm{Dop}}$). All the rate values used in theoretical calculations have been normalized to the natural decay rate for the Rb D_2 line: $\gamma_{\mathrm{nat}} = 2\pi \times 6.07$ MHz.

The time-dependent fluorescence spectra are then calculated numerically using the following formula [83]

$$\Phi(t) = \sum_{i=3,4,5,6} \sum_{j=1,2} \Gamma_{i,j} \rho_{i,i}(t), \tag{3.8}$$

where $\rho_{i,i}(t)$ are the solutions of Eq. (3.4).

3.3 Experiment and numerical simulation

Experimental measurements were done on a simple setup schematically depicted in Figure 3.2. Collimated linearly polarized radiation from a free-running single-frequency diode laser (maximum power 25 mW; spectral linewidth 15 MHz) with 2 mm beam diameter was directed into a glass cell (135 mm long, 20 mm diameter, no antirelaxation coating, no added buffer gas) with a side arm containing natural rubidium.

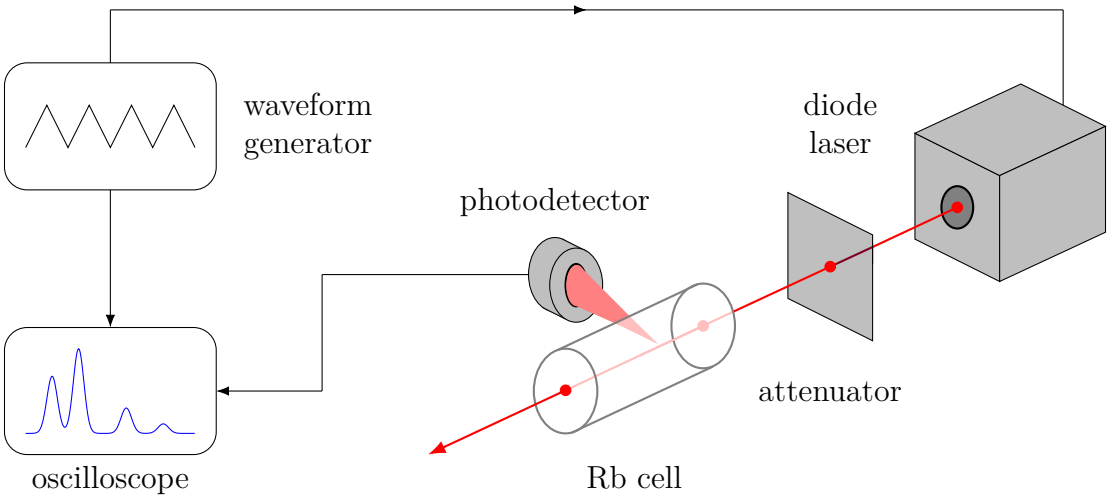

Figure 3.2: Schematic drawing of the experimental setup.

The choice of a free-running laser was conditioned by the necessity for fast linear frequency scanning, which, unlike external piezoelectric-driven cavity diode lasers, is easily realizable by modulation of an injection current. The cell was kept at a room temperature (22°C), which corresponds to the number density of rubidium atoms $N_{\mathrm{Rb}} = 5 \times 10^9$ cm^{-3}. A fast linear photodetector was placed at 90° to the laser beam propagation direction, closer to the entrance window.

In order to scan the laser radiation frequency across the spectral region of atomic D_2 line, covering Doppler-overlapped hyperfine transition groups ^{87}Rb $F_g = 2 \rightarrow F_e = 1, 2, 3$, ^{85}Rb $F_g =$

$3 \rightarrow F_e = 2, 3, 4$, ^{85}Rb $F_g = 2 \rightarrow F_e = 1, 2, 3$, and ^{87}Rb $F_g = 1 \rightarrow F_e = 0, 1, 2$ (typically 11 GHz range), the laser diode injection current was modulated by periodic triangular pulses from Siglent SDG5082 waveform generator. The scanning rate and frequency range were controlled by changing the generator frequency and amplitude, respectively. It was possible to fine-tune the laser radiation frequency by applying a bias (offset) to the generator signal. Fluorescence signal from the photodetector (photodiode with operational amplifier) was recorded by a digital storage oscilloscope Tektronix TDS3032B. The maximum used scanning frequency was limited by the temporal response of the photodetector ($\tau_{\mathrm{det}} \approx 5$ µs).

The scanning time (period) itself cannot be considered as a physical parameter, since the resonant interaction time of an individual atom with laser radiation depends also on the spectral range covered by scanning. A real physical meaning should be attributed to the scanning rate defined as $S = \partial\omega/\partial t$. In addition, the interaction time is also affected by the homogeneous broadening width and laser radiation linewidth. For this reason, to facilitate interpretation of the results, only two experimental parameters were varied throughout our measurements: laser radiation power P_L and triangular modulation frequency f_s. The spectral range $\Delta\omega_s = 2\pi \times 11.12$ GHz was kept invariable both on descending (ω_-) and ascending (ω_+) wings. Moreover, the frequency positions of hyperfine transitions in the scanning spectral range were kept unchanged, independently of f_s value. In these conditions the scanning rate can be determined by simple rescaling of modulation (scanning) frequency:

$$S = \frac{\partial\omega}{\partial t} = \frac{\Delta\omega_s}{\tau_\pm} = 2\Delta\omega_s f_s, \tag{3.9}$$

where $\tau_\pm$ is the scanning time on the ascending and descending wings of modulation signal ($\tau_+ = \tau_-$). Experimental measurements were done for thirteen values of f_s, from 1 Hz to 10 kHz [see Table 3.1]. The table contains also corresponding values of $\tau_\pm$ and $S/2\pi$.

Table 3.1: Linkage between the temporal parameters of the experiment.

No.	f_s (Hz)	$\tau_\pm$ (ms)	$S/2\pi$ (MHz/µs)
1	1	500	0.02224
2	2.5	200	0.0556
3	5	100	0.1112
4	10	50	0.2224
5	25	20	0.556
6	50	10	1.112
7	100	5	2.224
8	250	2	5.56
9	500	1	11.12
10	1000	0.5	22.24
11	2500	0.2	55.6
12	5000	0.1	111.2
13	10000	0.05	222.4

The recorded spectra are combined in Figure 3.3. The three column panels represent the results for three values of P_L (1, 5, and 20 mW). In each panel, the spectra recorded for different values of f_s are shifted vertically from each other for visual convenience, preserving a unique vertical scale for the whole graph. First (left) and second (right) halves of the spectrum correspond to falling and rising laser radiation frequency, respectively.

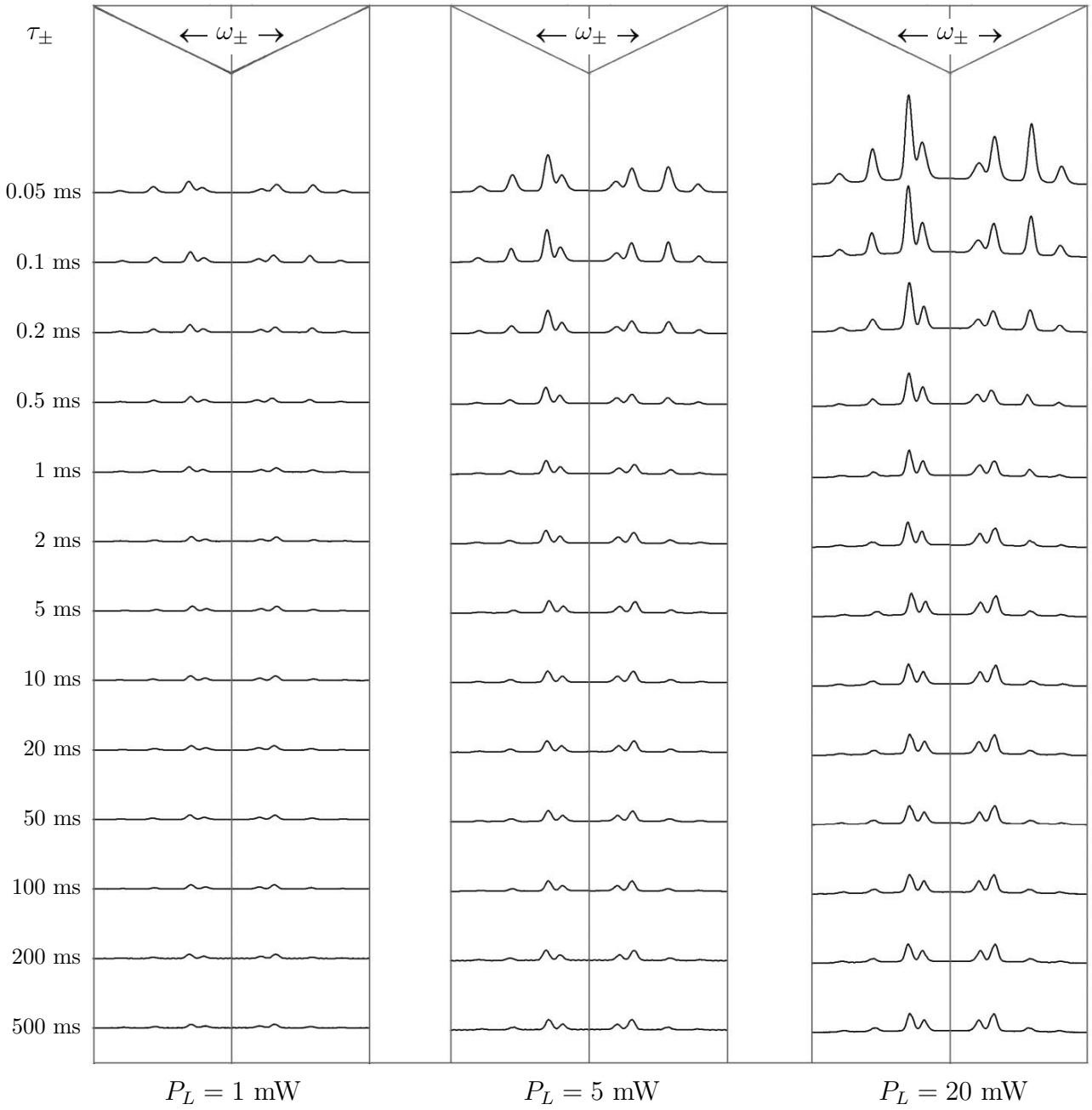

Figure 3.3: Fluorescence spectra recorded at thirteen values of scanning rate for three values of laser power: $P_L = 1,\ 5,$ and 20 mW. $\tau_\pm$ indicates rising (right half) and falling (left half) laser frequency scan times. The scanning spectral range is 11.12 GHz, covering ^{87}Rb $F_g = 2 \rightarrow F_e = 1, 2, 3$, ^{85}Rb $F_g = 3 \rightarrow F_e = 2, 3, 4$, ^{85}Rb $F_g = 2 \rightarrow F_e = 1, 2, 3$, and ^{87}Rb $F_g = 1 \rightarrow F_e = 0, 1, 2$ transition groups (in order of rising frequency; see right halves of each panel). Spectra are shifted vertically at equal distances; the same vertical scale is applied for all the spectra.

The following observations can be drawn from these graphs. For $P_L = 1$ mW, spectra with ω_- and ω_+ scans exhibit mirror symmetry, and the shapes of spectra do not change significantly when changing $\tau_\pm$. Mirror asymmetry in ω_-/ω_+ scans appears for $P_L = 5$ mW with the decrease in scanning time, over certain values of $\tau_\pm$. This asymmetry establishes earlier, and becomes more pronounced for $P_L = 20$ mW. However, the symmetry tends to recover again when reaching the shortest attainable scan times. Finally, in the slow scanning limit (steady state interaction regime), hyperfine transition groups ^{85}Rb $F_g = 2 \to F_e = 1, 2, 3$ and ^{87}Rb $F_g = 1 \to F_e = 0, 1, 2$ consisting of "open" (non-cycling) components are strongly suppressed, notably for high laser power. Decrease in the scanning time results in gradual enhancement of fluorescence on these transitions.

Numerical simulation of the obtained experimental results has been done using the theoretical model described in Section 3.2. The simulated fluorescence spectra were plotted by using Eq. (3.8), with $\rho_{i,i}(t)$ found from solving Eq. (3.4). The values of physical and optical parameters characterizing the Rb atomic D_2 line system (transition dipole matrix elements, frequency positions, decay rates, etc.) were taken from Refs. [82,83]. Simulation of linear scanning by symmetric triangular pulses was done using Eq. (3.6). Two fitting parameters were used throughout the simulation: the laser electric field amplitude E (see the reasoning in Section 3.4), and the relaxation rate of the ground energy levels to the equilibrium state γ_0. The results of numerical simulation are in a good agreement with the experimental results. Comparison of theoretical and experimental spectra for three values of the scanning rate is presented in Figure 3.4. The best fitting of spectral lineshapes throughout the whole range of exploited scanning frequencies and incident laser powers has been obtained for $\gamma_0 = 1.03(\pm 0.1) \times 10^{-3}\gamma_{\text{nat}}$.

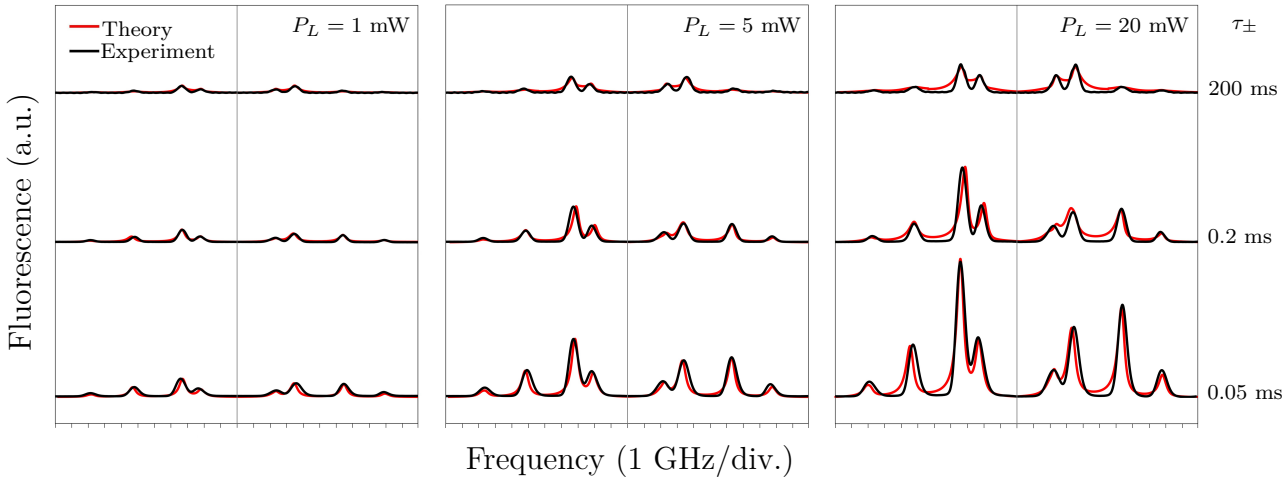

Figure 3.4: Comparison of theoretical (red lines) and experimental (black lines) fluorescence spectra for 3 values of the laser radiation power and 3 values of the scanning rate.

Quantitative dependences of the fluorescence peak signals from scanning time (separately, for descending ω_- and ascending ω_+ scans) derived from the spectra shown in Figure 3.3 are presented in Figure 3.5, along with corresponding theoretical modeling curves. As one can clearly see from these graphs, establishment of a steady state interaction regime correspond-

ing to scan-time-independent (horizontal) trace on the graphs, is strongly dependent on laser radiation power, but also somewhat varies for different transition groups. The most drastic changes occur for the groups containing V-type cycling transitions: ^{85}Rb $F_g = 3 \rightarrow F_e = 2, 3, 4$ and ^{87}Rb $F_g = 2 \rightarrow F_e = 1, 2, 3$, where a deep well is formed at a certain value of τ_- for ω_+ scanning direction, while for the opposite direction, ω_- fluorescence grows monotonically with the decrease in τ_+. Monotonic growth when decreasing scan time is observed also for the transition groups ^{85}Rb $F_g = 2 \rightarrow F_e = 1, 2, 3$ and ^{87}Rb $F_g = 1 \rightarrow F_e = 0, 1, 2$, independently of the sense of scanning. No expected saturation of this growth was observed at the largest values of f_s attainable in our experiment. At the same time, it can be seen that as the scanning speed increases, the peak fluorescence values for scanning with falling and rising frequencies tend to approach each other.

3.4 Discussion and emerging results

The observed dynamics of the fluorescence spectra when changing the scanning conditions is caused mainly by the optical pumping [84]. In this process, taken into account by our theoretical model, the atom absorbing the laser photon on "open" (non-cycling) atomic transitions ($F_g = 1, 2 \rightarrow F_e = 1, 2$ for ^{87}Rb and $F_g = 2, 3 \rightarrow F_e = 2, 3$ for ^{85}Rb) is driven to the excited state with possible consequent spontaneous emission to the other hyperfine sublevel of the ground state, which does not interact with the laser radiation. The efficiency of this process depends on both the laser intensity and atom-light interaction time.

For slow enough scanning of the laser radiation frequency, allowing establishment of a steady-state atom-light interaction regime, the time period between successive resonances is longer than the ground-state relaxation time (the population is "thermalized" to equilibrium condition), and the amplitude for each particular transition group remains invariable, independent of scanning conditions [see the lower spectra in Figure 3.5]. The situation changes for the transient regime, when increasing the scanning rate to a value for which coherence or redistribution of population established during the resonant interaction with a particular hyperfine transition is partly preserved by the time of resonance with the neighboring transition. As a result, the ground-state population and, hence, also absorption and fluorescence, are affected by population redistribution occurring during the previous resonance. This "memory effect" causes modification of magnitudes of individual fluorescence components depending on the scanning rate and direction.

As one can expect, the further increase in scanning rate (beyond the values explored in the present experiment) should eventually result in equalization of the fluorescence peaks for the rising and falling frequency scans, as no significant redistribution of population due to the optical pumping can be developed because of an extremely short interaction time. In parallel, the fluorescence signal amplitude should decline for the same reason: eventually, only one cycle of absorption and emission can occur at the highest scanning rates. These considerations are supported by the results of numerical modeling [see simulation curves in Figure 3.5 for frequency scanning time below 10^{-5} s].

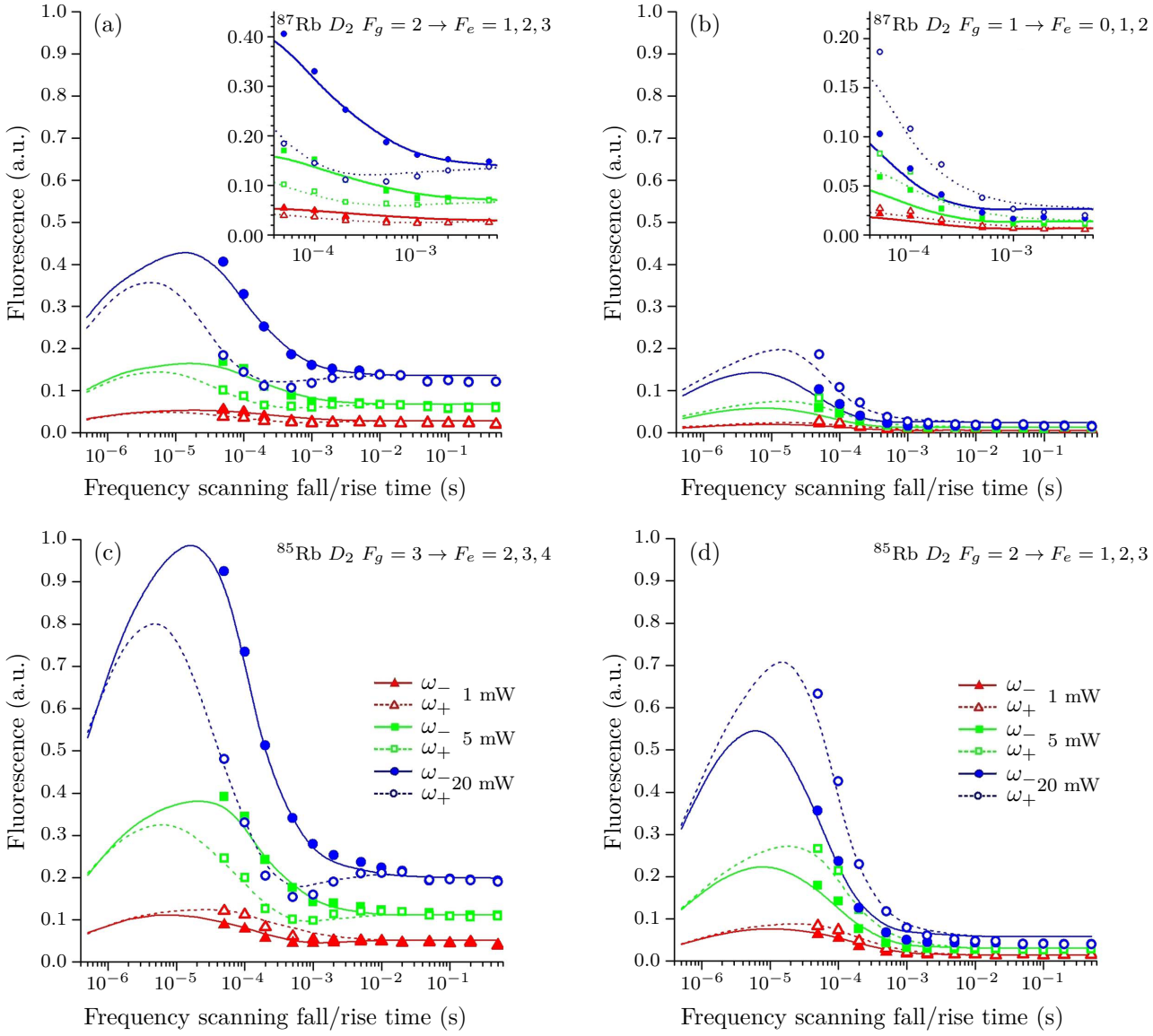

Figure 3.5: Dependence of the fluorescence peak intensity on the laser frequency scanning rate for the four hyperfine transition groups of Rb D_2 line, recorded at three values of P_L. Lines: theory; symbols: experiment. Dashed lines/open symbols and solid lines/solid symbols correspond to scanning with falling and rising frequency (ω_- and ω_+), respectively. Insets in (a) and (b) show zoomed plots in the region of $\tau_\pm = 4 \times 10^{-5} - 6 \times 10^{-3}$ s.

For extremely fast scanning rates, when the atom-light interaction time becomes comparable to the natural decay time ($\sim$ 30 ns), one can expect to observe behavior intrinsic to a pulsed excitation regime, such as nutation referred to as the Rabi oscillation between the ground and excited states. However, we should note that each individual atom with a certain velocity (frequency shift) and position in the laser beam (Rabi frequency) will contribute to such a process with random frequency and phase, so that the overall oscillatory signal will be averaged and damped, even if the photodetector bandwidth is appropriate.

The theoretical model used in this chapter allows to reproduce experimental results, which indicates that all the involved physical processes are adequately addressed. Throughout the

modeling, we have used known spectroscopic parameters for Rb D_2 line system, except for two quantities that were free-fitting parameters, namely, (i) the effective amplitude of the laser electric field E dependent on laser radiation power P_L, and (ii) the relaxation rate of the lower energy levels to the equilibrium isotropic state γ_0. Necessity to fit the value of E, which enters in expression for the Rabi frequency $\Omega_{i,j} = d_{i,j}E/\hbar$, comes from uncertainty of the distribution of laser radiation intensity across the beam and its broad spectral linewidth, which exceeds the Rb natural linewidth.

A much more important fitting parameter is the ground-state relaxation rate γ_0, which characterizes the particular vapor cell used in the experiment. The value of γ_0 comprises contributions from population relaxation time T_1 (relevant for our study) and coherence relaxation time T_2. As this parameter remains unchanged throughout the experimental measurements, it can be determined unambiguously by the best fitting of all the experimental spectra recorded for different temporal and power conditions. The obtained fitted value $\gamma_0 \approx 1.03 \times 10^{-3}\gamma_{\text{nat}} \approx 2\pi \times 6.25$ kHz is close by the order of magnitude to the expected value for the conditions of our experiment.

Indeed, in the absence of a buffer gas and antirelaxation coating, the value of relaxation rate γ_0 should be determined by the flight of optically pumped atoms to the cell walls where they undergo spin–exchange collisions. The contribution from Rb-Rb pairwise collisions has to be completely ruled out because of a small value of the cross section (1.9×10^{-14} cm^2 [85]) and very low vapor density. As shown in Ref. [86], the spin-exchange binary collisions in comparable experimental conditions yield only $\sim\ 2\pi \times 25$ Hz contribution. In our experiment, the mean atomic velocity $\overline{v} = \sqrt{8k_BT/\pi m_a} = 265$ m/s (k_B is Boltzmann constant, T is cell temperature, m_a is atomic mass). A rough estimate for the atom departing from the laser beam normally towards the wall, undergoing spin-exchange collision with 100 % probability, and returning into the beam with the same trace gives $\gamma_0 = 2\pi \times 13.3$ kHz.

More detailed calculations should take into account the angular distribution of atomic velocity, probabilistic nature of relaxation caused by the atom-wall collision, as well as self-diffusion of atoms in a vapor. All these factors lead to the decrease in the estimated value, as demonstrated by Franzen [see Ref. [87]]. In the conditions of our experiment, the mean free path of Rb atoms $\lambda = 1/\sqrt{2}N\sigma_{\text{self}}$, where N is the number density of atoms, and σ_{self} is the total interatomic collision cross section, substantially exceeds geometric dimensions of the cell. Indeed, with $N = 5 \times 10^9$ cm^{-3} and $\sigma_{\text{self}} = 1.397 \times 10^{-13}$ cm^2 [88], we get $\lambda \approx 10$ m. This estimate indicates that we can consider ballistic trajectories of atoms towards cell walls, excluding as irrelevant the self-diffusion in the vapor.

Elaborated expressions for determination of the ground-state population relaxation time T_1 (and hence, relaxation rate γ_0) in a high-vacuum cell, in which interatomic collisions are irrelevant, are presented in Ref. [89], where this relaxation time is identified with the mean TOF of the atoms between two collisions with the walls. Following these calculations, for a cylindrical cell with diameter d and length l, the ground-state relaxation rate is expressed as

$$\gamma_0 = 2\pi \times \frac{1}{T_1} = 2\pi \times \frac{\overline{v}S}{4V} = 2\pi \times \frac{\overline{v}(l + d/2)}{ld}, \tag{3.10}$$

where V and S are the cell volume and surface area, respectively. For the conditions of our experiment, Eq. (3.10) yields $\gamma_0 = 2\pi \times 14.2$ kHz, which is 2.3 times bigger than the value obtained from the fitting.

This difference can be attributed to the presence of residual buffer gas (unidentified contamination) in the cell, which can lead to the decrease in the estimated value, as first shown by Franzen [87]. For a cylindrical cell with diameter d [cm] and length l [cm], the relaxation rate of optically pumped Rb atoms caused by diffusion to the cell walls γ_{0D} [Hz] can be expressed in the following form [86, 90]:

$$\begin{aligned} \gamma_{0D} &= 2\pi \times \left[\left(\frac{\mu}{d/2} \right)^2 + \left(\frac{\pi}{l} \right)^2 \right] D, \\ D &= D_0 \frac{p_0}{p} \left(\frac{T}{T_0} \right)^{3/2}, \end{aligned} \tag{3.11}$$

where $\mu = 2.405$ is the first zero of the Bessel function [91], D [cm^2/s] is the diffusion coefficient dependent on pressure and temperature, D_0 is the diffusion constant at normal conditions (pressure $p_0 = 760$ Torr, temperature $T_0 = 273$ K), and p and T are the pressure and temperature of the cell, respectively. Taking the values for the present work $d = 2$ cm, $l = 13.5$ cm, $\gamma_{0D} \approx \gamma_0 = 2\pi \times 6.25$ kHz, we obtain for the diffusion coefficient $D \approx 1070$ cm^2/s.

Assuming that our homemade cell was not properly pumped out or that over time (20 years from the date of manufacturing), some air leaked through the welded junctions, we may suppose that the most realistic residual buffer gas is nitrogen (N_2). The contribution from known helium permeation through the cell walls is negligible in this case because of low partial pressure in the air (~ 4 mTorr). As one can find from Ref. [90], the diffusion constant for N_2-buffered Rb vapor is $D_0 = 0.144$ cm^2/s, and from the second expression of Eq. (3.11) for $T = 295$ K, we obtain $p \approx 0.11$ Torr, which seems realistic.

We should note that if we know the type and pressure of the buffer gas X, this result can be further explored for determination of another important spectroscopic parameter that is a cross section σ_{buf} of elastic velocity-changing Rb-X atomic collisions. The latter can be calculated in the frame of Chapman-Enskog theory, following the expression presented, e.g., in Ref. [92]:

$$\sigma_{\text{buf}} = \frac{3}{8pD} \sqrt{\frac{\pi \left(k_B T \right)^3}{2m_r}}, \tag{3.12}$$

where m_r is the reduced mass of the interacting particles. Exploring this equation for $p = 0.11$ Torr, $D = 1070$ cm^2/s, $T = 295$ K, and reduced mass of Rb-N_2 atomic pair $m_r = 3.52 \times 10^{-23}$ g, we obtain the cross section for Rb-N_2 collisions $\sigma_{\text{buf}} = 4.06 \times 10^{-15}$ cm^2, which is in very good agreement with the value 3.93×10^{-15} cm^2 reported in Ref. [88].

The presence of a buffer gas in the cell can be easily checked by implementing the saturated absorption (SA) experiment: addition of > 0.5 Torr of a foreign gas leads to nearly complete suppression of sub-Doppler features in the SA spectrum because of velocity-changing collisions [93]. The SA measurement done with our cell has not revealed any noticeable distinc-

tion in appearance of a Doppler pedestal and lineshapes of velocity-selective optical pumping and crossover resonances as compared with a buffer-free reference cell, which indicates that the residual buffer gas pressure is below the critical level.

The obtained results can be used for the realization of a heralded control of atomic level population in alkali-metal vapor by implementing frequency modulation of cw lasers in a non-stationary (transient) regime of resonant interaction. The control will be realized by means of changing the shape, duration, and delay of the sequence of generated pulses. It is expected that the results of these studies can be used for the enhancement of efficiency of photochemical reactions, development of new schemes of sensitive optical magnetometers, development of elements for quantum communication systems, and for other applications.

3.5 Conclusion

Summarizing, we have studied the evolution of fluorescence spectra of a room-temperature rubidium vapor in the region of the atomic D_2 line while changing the linear (triangular) scanning rate of exciting cw laser radiation frequency, exploring changeover from steady-state to the transient interaction regime. The general aim of this chapter was to quantitatively study temporal dynamics of fluorescence based on an extremely simple experiment.

In the low scanning rate limit, the spectral lineshape and magnitude of fluorescence across the hyperfine transitions manifold are independent of the speed and direction of frequency scanning, evidencing the steady-state atom-radiation field interaction regime. In this regime, the interaction time is determined by the mean TOF of atoms through the laser beam. Increase in the scanning rate above $\sim$ 2 MHz/µs (for the conditions of our experiment) results in gradual modification of the amplitudes of fluorescence peaks, different for different transitions and dependent on the scanning direction and speed, manifesting the onset of the transient interaction regime. In this regime, the interaction time is caused by the temporal period when the scanned laser field is in resonance with atomic transition. The maximum asymmetry in fluorescence peak amplitudes for rising and falling frequency scanning is obtained at the rate of $\sim$ 20-60 MHz/µs. The symmetry tends to recover again at a higher scanning rate.

Theoretical modeling taking into consideration all the relevant physical processes exhibits good agreement with the experimental results. Due to this consistency, it is possible to retrieve some important parameters of the experiment, in particular, the relaxation rate of the lower energy levels to the equilibrium isotropic state γ_0, the diffusion coefficient D in a buffered vapor cell, and the corresponding collisional cross section σ. The obtained results can also be used for determination of appropriate temporal conditions for efficient heralded control of atomic population in a multilevel system, by implementing a frequency-modulated cw laser as an effective source of controllable pulsed radiation.

After this work, presented here-before, we have continued to study it and used machine learning methods to determine the value of the fitting parameter γ_0 from the experimentally registered fluorescence spectra [see Ref. [94]]. Using machine learning methods for this kind of physical problems is justified because in general they allow predicting fitting parameters

from the spectra registered for systems with another configuration (e.g. another laser power, laser scanning frequency, isotopes abundance, geometrical characteristics of the cell) than the one on which the "learning" process is done. This type of physical problems are classified as a typical regression problem. We used linear and nonlinear machine learning methods, as they are the most promising ones for processing and predicting the behavior of the physical system. An optimal regression model was built, which is characterized by high accuracy and short modeling time.

The results obtained in this chapter are published in Ref. [32]. The experiment was carried out in the Optics Laboratory at Institute for Physical Research, National Academy of Sciences of Armenia. The participants of the experiment were all the co-authors of the aforementioned article.

Chapter 4

New Standard Magnetic-Field Values Determined by Transition Cancellations Between Magnetic Sublevels of Alkali Vapor

4.1 Introduction

Laser spectroscopy of atomic vapors of alkali-metals (Li, Na, K, Rb, Cs) is widely used in atomic physics and numerous emerging applications, including Bose-Einstein condensate, quantum information, optical metrology, laser and sensor technologies, etc. [32, 95–99]. Interest in such single-electron atomic media is caused by the simplicity of the energy levels and the presence of strong optical transitions in the visible and near infrared, for which narrow-linewidth cw lasers are widely available. In recent decades, various magneto-optical processes in vapors of alkali-metals have been intensively investigated, which is in particular due to interest in the development of new schemes of optical magnetometry [22, 100, 101].

Among these processes is modification of the frequency and intensity of optical transitions between individual magnetic sublevels of the hyperfine structure of atoms in a magnetic field. It is well known that in an external magnetic field B, the initially degenerate atomic energy levels are split into magnetic sublevels (Zeeman splitting) [3, 102, 103]. The corresponding linear shift of atomic transition frequencies with B-field holds till it becomes comparable with the hyperfine splitting. With the further increase of the B-field, the transition frequencies strongly deviate from the linear behavior [104, 105]. Also, significant changes occur for atomic transition probabilities [106]. Further increase of the B-field results in re-establishment of linear frequency dependence and stabilization of the transition probabilities (hyperfine Paschen-Back regime) [107, 108].

The experimental observation of the above modifications, especially for relatively weak magnetic fields ($\lesssim 1000$ G), is strongly complicated due to the thermal motion of atoms in the vapor: individual transitions between the magnetic sublevels are Doppler-broadened (hundreds

of MHz), and they overlap under a wide Doppler profile. This complexity can be overcome by using sub-Doppler spectroscopy methods (for instance SA) or appropriate devices, for instance optical nanocells [109–111]. It is important to note that in addition to a significant decrease in the inhomogeneous broadening of transitions, the spectroscopy of nanocells (e.g. derivative of selective reflection (dSR) technique [109, 112–115]) also allows one to preserve the linear response of the medium (the magnitude of the atomic signal is directly proportional to the transition probability) [116].

In recent years, a number of papers have been published devoted to the study of the behavior of atomic transitions in a wide range of magnetic field spanning from the Zeeman to hyperfine Paschen-Back regime (G to kG scale) [117–121]. Along with the experiment, theoretical models have been developed, giving very good agreement with the measurement results. Among other results, strong transitions that are forbidden by the selection rules at zero magnetic field (magnetically-induced transitions), as well as significant suppression of the initially allowed transitions were observed exploiting different polarizations of the exciting laser radiation [122, 123].

Our theoretical model is used to determine polarization configurations and magnetic-field values, which outright cancel or maximize the transition intensities between individual magnetic sublevels of alkali atoms (i.e. drive the transition probability to zero or possible maximum). The cancellation theory is valid for $n\ ^2S_{1/2} \rightarrow k\ ^2P_{1/2,3/2}$ transitions, where $k = n$, $n+1$, $n+2$, $n+3$, ... is the principal quantum number of the excited $^2P_{1/2}$ and $^2P_{3/2}$ state. Nevertheless, there is a restriction on k: The Zeeman degenerated $k\ ^2P_{1/2,3/2}$ states should not be overlapped with other states for the magnetic-field values starting from zero up to the maximum considered one. We were able to extract a unique formula for the magnetic-field values canceling some transitions while leading to the maximum of others. Particularly, in this chapter we consider the cancellation or maximization of transition intensities of stable and long-lived alkali-atom isotopes. But for ^{85}Rb and ^{87}Rb isotopes we considered $5\ ^2S_{1/2} \rightarrow 5\ ^2P_{1/2,3/2}$ (D_1 and D_2 lines accordingly) and $5\ ^2S_{1/2} \rightarrow 6\ ^2P_{1/2,3/2}$ transitions. For these transitions all the quantum numbers (with the exception of the principal quantum number) and all the Landé factors are the same, but also a lot of significant differences exist. The first important difference is the laser wavelength. For the D_1 and D_2 lines the laser wavelength is $\sim$ 795 nm and $\sim$ 780 nm respectively, while the laser wavelengths are $\sim$ 422 nm and $\sim$ 420 nm for $5\ ^2S_{1/2} \rightarrow 6\ ^2P_{1/2,3/2}$ transitions. Another difference is the overall transition strength. From the point of view of theoretical calculations the only difference between these two type of transitions is the energy differences of the excited states. For the $5\ ^2S_{1/2} \rightarrow 5\ ^2P_{3/2}$ and $5\ ^2S_{1/2} \rightarrow 6\ ^2P_{3/2}$ transitions, the study is done mostly using numerical methods, but in several cases we were able to extract analytical formula depending on the Hamiltonian submatrices sizes. All the magnetic-field values, which cancel the transitions are obtained. This set of values may be used as standards in the magnetometer calibration tasks and to improve the precision of physical constants involved in the model.

The issues related to experimental feasibility of the B-field cancellation of transitions, and outline the possible applications, such as optical mapping of magnetic field and B-field control

of optical information are also addressed.

4.2 Dirac equation and atom - magnetic field interaction

As in this chapter we are going to study transition cancellations and the spectra of an alkali atom under the influence of electromagnetic field, it will be better to start from brief analysis of the well known Dirac equation to order v^2/c^2, which is well describing the atom-electromagnetic field interaction, where the field is described by the potentials $\mathbf{A}$ and V

$$\left[\frac{1}{2m_{el}}\left(\mathbf{p}+\frac{e}{c}\mathbf{A}\right)^2+\frac{e}{m_{el}c}\mathbf{S}\cdot\boldsymbol{\nabla}\times\mathbf{A}-\frac{p^4}{8m_{el}^3c^2}-\frac{e\hbar}{8m_{el}^2c^2}\Delta V \right. \\ \left. -\frac{e}{2m_{el}^2c^2}\mathbf{S}\cdot(\boldsymbol{\nabla}V\times\mathbf{p})-eV\right]\Psi=E\Psi, \quad (4.1)$$

where m_{el} is the electron mass, $\mathbf{p}$ is its impulse, e is its electric charge, c is the light velocity, $\mathbf{A}$ is the vector and V is the scalar potential, $\mathbf{S}=\frac{\hbar}{2}\boldsymbol{\sigma}$ is the electron's spin momentum: $\boldsymbol{\sigma}=\left(\sigma_x,\sigma_y,\sigma_z\right)$ are the Pauli matrices. One can find more details in references [70, 124, 125].

When we consider non-relativistic electron in the gauge $\{\mathbf{A}=0,V\}$, then the Dirac equation (4.1) shortens to

$$H_0\Psi_n\equiv\left[\frac{\mathbf{p}^2}{2m_{el}}-eV\right]\Psi_n=E_n\Psi_n. \quad (4.2)$$

If the atomic states are bounded and the potential is spherical symmetric: $V\equiv V(r)$, from Eq. (4.2) we obtain

$$E_n=-\mathcal{R}\frac{Z^2}{n^2}, \quad (4.3)$$

with $\mathcal{R}=\frac{m_{el}e^4}{8\epsilon_0h^2}\approx 13.6$ eV, the Rydberg constant, Z the atomic number and n the principal quantum number. The scalar potential is $V=Ze/r$ and the spin-orbit (SO) interaction Hamiltonian could be rewritten as

$$H_{SO}=-\frac{e}{2m_{el}^2c^2}\mathbf{S}\cdot(\boldsymbol{\nabla}V\times\mathbf{p})=\frac{Ze^2}{2m_{el}^2c^2r^3}\mathbf{S}\cdot\mathbf{L}, \quad (4.4)$$

where $\mathbf{L}=\mathbf{r}\times\mathbf{p}$ is the angular momentum. H_0+H_{SO} is the electron Hamiltonian bounded to the nucleus of atom. For the energy it will lead to the following formula:

$$E_{SO}=\frac{Z^4e^2\hbar^2}{4a_0^3m_{el}^2c^2}\cdot\frac{J(J+1)-L(L+1)-S(S+1)}{n^3L(L+1/2)(L+1)}, \quad (4.5)$$

where $a_0=\frac{4\pi\epsilon_0\hbar^2}{m_{el}^2e^2}\approx 0.53$ Å is the Bohr radius. Taking into account the expression for the zero-field Hamiltonian [see Eq. (4.2)], the first order relativistic correction $H_R=-\frac{p^4}{8m_{el}^3c^2}$ can

be rewritten as

$$H_R = -\frac{1}{2m_{el}c^2}\left(H_0 + \frac{Ze^2}{r}\right)^2, \tag{4.6}$$

with the energy of the first order relativistic correction:

$$E_R = -E_n^2 \cdot \frac{Z^2e^2}{2m_{el}c^2a_0} \cdot \left(\frac{2n}{L+1/2} - 3\right). \tag{4.7}$$

And the energy of Darwin term, which Hamiltonian $H_D = \frac{e\hbar^2\Delta V}{8m_{el}^2c^2}$ and it brings to the energy shift for the S-states, is

$$E_D = \frac{Z^4e^2\hbar^2}{2n^3m_{el}^2c^2a_0^3}. \tag{4.8}$$

The following is the so-called fine structure Hamiltonian:

$$H_f = H_0 + H_{SO} + H_R + H_D. \tag{4.9}$$

To completely describe the system under the influence of static external magnetic field, we need to consider the Zeeman effect. It arises, when $\mathbf{A} \neq 0$. So, the magnetic Hamiltonian is

$$H_m = \frac{e}{2m_{el}c}\left(\mathbf{p}\cdot\mathbf{A} + \mathbf{A}\cdot\mathbf{p}\right) + \frac{e}{m_{el}c}\mathbf{S}\cdot\boldsymbol{\nabla}\times\mathbf{A}. \tag{4.10}$$

In the case that the magnetic field is constant and uniform (for instance, due to its geometry, this condition is extremely well verified for a nanocell), it follows that

$$\mathbf{A} = \frac{1}{2}\left(\mathbf{B}\times\mathbf{r}\right) \tag{4.11}$$

with $\mathbf{B}$ the magnetic field vector. Taking into account Eq. (4.10) and Eq. (4.11), the Hamiltonian could be expressed as follows:

$$H_m = \frac{\mu_B}{\hbar}\mathbf{B}\left(\mathbf{L} + 2\mathbf{S}\right), \tag{4.12}$$

where $\mu_B = \frac{e\hbar}{2m_{el}c}$ is the Bohr magneton. Drawing parallels with the classical expression of a magnetic dipole in a magnetic field, the magnetic Hamiltonian could be rewritten as

$$H_m = -\boldsymbol{\mu}_\mathbf{L}\cdot\mathbf{B} - \boldsymbol{\mu}_\mathbf{S}\cdot\mathbf{B}, \tag{4.13}$$

where $\boldsymbol{\mu}_\mathbf{L} = -\frac{\mu_B g_L}{\hbar}\mathbf{L}$ and $\boldsymbol{\mu}_\mathbf{S} = -\frac{\mu_B g_S}{\hbar}\mathbf{S}$ are called as magnetic moment operators associated with $\mathbf{L}$ and $\mathbf{S}$ respectively. $g_L = 1$ and $g_S = 2$ are electron orbital and electron spin Landé factors. To obtain more precise value of g_L, we need to take into account the finite mass of the nucleus. So, the expression for the orbital Landé factor [82] is

$$g_L = 1 - \frac{m_{el}}{m_n} \tag{4.14}$$

with m_n the nuclear mass [126] of the atom. Dirac's theory predicted $g_S = 2$, but one should note that in what follows we will use the most known exact values of the Landé factors in the present chapter, as we want to obtain exact analytical relations and precise magnetic-field values canceling transitions.

From now on we choose the direction of the external static magnetic field along z-axis, i.e. $\mathbf{B} = B\hat{\mathbf{e}}_z$. This defines the quantization axis. It is important to note that a lot of formalism describing magnetic Hamiltonian exist [3, 104, 124, 127, 128], but we chose a formulation of Tremblay *et al.* [104]. After applying Wigner-Eckart theorem on the derived formulas and expanding 3-j and 6-j symbols [129–131], for the H_m matrix diagonal elements we obtain

$$\langle J, m_J | \, H_0 + H_m \, | J, m_J \rangle = E_f(J) - \mu_B g_J m_J B \tag{4.15}$$

with g_J the Landé factor of the total electronic angular momentum $\mathbf{J}$ [see Ref. [132]], given by

$$g_J = g_L \frac{J(J+1) - S(S+1) + L(L+1)}{2J(J+1)} + g_S \frac{J(J+1) + S(S+1) - L(L+1)}{2J(J+1)}. \tag{4.16}$$

Non-diagonal elements are different from zero, if $\Delta L = 0$ and $\Delta m_J = 0$:

$$\begin{aligned} \langle J, m_J | \, H_0 + H_m \, | J-1, m_J \rangle &= \langle J-1, m_J | \, H_0 + H_m \, | J, m_J \rangle \\ &= -\frac{\mu_B B}{2} \left(g_L - g_S \right) \left(\frac{J^2 - m_J^2}{J(2J+1)(2J-1)} \right)^{1/2} \\ &\quad \times \left(\frac{\left[(L+S+1)^2 - J^2 \right] \left[J^2 - (L-S)^2 \right]}{J} \right)^{1/2}. \end{aligned} \tag{4.17}$$

Above we did not took into account the electron-nucleus interaction of the atom. It brings to the splitting of the hyperfine structure (so-called hyperfine structure) and is described by the following expression [133]:

$$H_{hf} = A_{hf} \mathbf{I} \cdot \mathbf{J} + B_{hf} \frac{3 \left(\mathbf{I} \cdot \mathbf{J} \right)^2 + \frac{3}{2} \mathbf{I} \cdot \mathbf{J} - IJ \left(I+1 \right) \left(J+1 \right)}{4IJ \left(2I-1 \right) \left(2J-1 \right)}, \tag{4.18}$$

where $\mathbf{I}$ is the nuclear spin, A_{hf} and B_{hf} are the magnetic dipole and the electric quadrupole constants. So, our new magnetic Hamiltonian will be

$$H_m = \frac{\mu_B}{\hbar} B \left(g_L L + g_S S + g_I I \right) \tag{4.19}$$

with g_I nuclear Landé factor. Now we denote our complete Hamiltonian as

$$H \equiv H_f + H_{hf} + H_m, \tag{4.20}$$

which fully describes alkali atom under the influence of external static magnetic field.

In the coupled $|F, m\rangle$ basis the diagonal elements of the Hamiltonian matrix H have the

following form:

$$\langle F, m| H |F, m\rangle = E_{hf}(F) - \mu_B g_F m B, \tag{4.21}$$

where $E_{hf}(F)$ is the energy of the hyperfine F level, g_F is the associated Landé factor [132] expressed as

$$g_F = g_J \frac{F(F+1) - I(I+1) + J(J+1)}{2F(F+1)} + g_I \frac{F(F+1) + I(I+1) - J(J+1)}{2F(F+1)}, \tag{4.22}$$

and m is the magnetic quantum number. Non-diagonal elements are non-zero when $\Delta F = 0$ and $\Delta m = 0$, and are given by

$$\begin{aligned}\langle F-1, m| H |F, m\rangle &= \langle F, m| H |F-1, m\rangle \\ &= -\frac{\mu_B B}{2}(g_J - g_I)\left(\frac{F^2 - m^2}{F(2F+1)(2F-1)}\right)^{1/2} \\ &\quad \times \left(\frac{\left[(J+I+1)^2 - F^2\right]\left[F^2 - (J-I)^2\right]}{F}\right)^{1/2}.\end{aligned} \tag{4.23}$$

The electric dipole component D_q [104, 134] is determined using the following relation:

$$\left|\langle e| D_q |g\rangle\right|^2 = \frac{3\epsilon_0 \hbar \Gamma_e \lambda_{eg}^3}{8\pi^2} a^2[|\psi(F_e, m_e)\rangle ; |\psi(F_g, m_g)\rangle ; q], \tag{4.24}$$

where Γ_e is the natural decay rate, λ_{eg} is the wavelength between the ground and excited states, and $q \equiv \Delta m = 0, \pm 1$ stands respectively for π, $\sigma^{\pm}$ transitions. To distinguish the m values, for the ground and excited states we will use m_g and m_e notations respectively. The modified transfer coefficients read:

$$a[|\psi(F_e, m_e)\rangle ; |\psi(F_g, m_g)\rangle ; q] = \sum_{F'_e, F'_g} c_{F_e F'_e} a(F'_e, m_e; F'_g, m_g; q) c_{F_g F'_g}, \tag{4.25}$$

where $a(F_e, m_e; F_g, m_g; q)$ are the unperturbed transfer coefficients:

$$\begin{aligned}a(F_e, m_e; F_g, m_g; q) &= (-1)^{1+I+J_e+F_e+F_g-m_e}\sqrt{2J_e+1}\sqrt{2F_e+1}\sqrt{2F_g+1} \\ &\quad \times \begin{pmatrix} F_e & 1 & F_g \\ -m_e & q & m_g \end{pmatrix} \begin{Bmatrix} F_e & 1 & F_g \\ J_g & I & J_e \end{Bmatrix},\end{aligned} \tag{4.26}$$

which depend on 3-j (parenthesis) and 6-j (curly brackets) Wigner symbols.

4.3 Alkali-metal atoms $n\,^2S_{1/2} \rightarrow k\,^2P_{1/2}$ transition cancellations theory

The characteristic polynomial of a 3×3 or 4×4 matrix admits analytical expressions for its roots (based on Cardano and Ferrari's formulas [135]), but they are too heavy to be calculated and moreover to be exhibited in the thesis. Thus in order to explain clearly the way we will determine the magnetic-field values, we begin here-after with 2×2 matrices.

It is well known that fine structure is the splitting of the main spectral lines of an atom and is the result of the coupling between the orbital angular momentum $\mathbf{L}$ and spin angular momentum $\mathbf{S}$ of the single optical electron. The total electronic angular momentum can be written as

$$\mathbf{J} = \mathbf{L} + \mathbf{S} \tag{4.27}$$

and the $\mathbf{J}$ quantum number corresponding to the momentum takes

$$|L - S| \leq J \leq L + S \tag{4.28}$$

values with L and S the projections of $\mathbf{L}$ and $\mathbf{S}$ respectively on the quantization axis (the convention that the magnitude of $\mathbf{J}$ is $\hbar\sqrt{J(J+1)}$ and the eigenvalue of J_z is $m_J\hbar$ is used). For $s \rightarrow p$ transitions, for the ground state we have $L = 0$ and $S = 1/2$ and for the excited state $L = 1$ and $S = 1/2$.

Hyperfine structure is the result of the combination between the total electronic angular momentum $\mathbf{J}$ and the total nuclear angular momentum $\mathbf{I}$ of the atom. The total angular momentum $\mathbf{F}$ is the sum of $\mathbf{I}$ and $\mathbf{J}$:

$$\mathbf{F} = \mathbf{I} + \mathbf{J}. \tag{4.29}$$

In this section we are only interested in $n\ ^2S_{1/2} \rightarrow k\ ^2P_{1/2}$ alkali-atom transitions and the value of the total electronic angular momentum magnitude for these transitions is $J = 1/2$. The total atomic angular momentum magnitude takes the following values:

$$I - 1/2 \leq F \leq I + 1/2, \tag{4.30}$$

where I is the magnitude of the total nuclear angular momentum. For all alkali atoms the total nuclear angular momentum is an integer or half-integer quantity. For the F number the following notations will be used:

$$F_{g,e}^{\pm} = I \pm 1/2, \tag{4.31}$$

where indices g and e stand for the ground and excited states respectively.

Within a magnetic field, the considered hyperfine structure energy levels splits into several magnetic sublevels, which are described by magnetic quantum numbers m taking the following

values:

$$-F \leq m \leq F. \tag{4.32}$$

On Figure 4.1, all possible schemes of $n\ ^2S_{1/2} \to k\ ^2P_{1/2}$ transitions are depicted. The following notations are used: n is the principal quantum number, which generally describes the system, $\zeta = E_0(F_g^+) - E_0(F_g^-)$ is the energy difference between ground levels and $\varepsilon = E_0(F_e^+) - E_0(F_e^-)$ is the energy difference between excited levels.

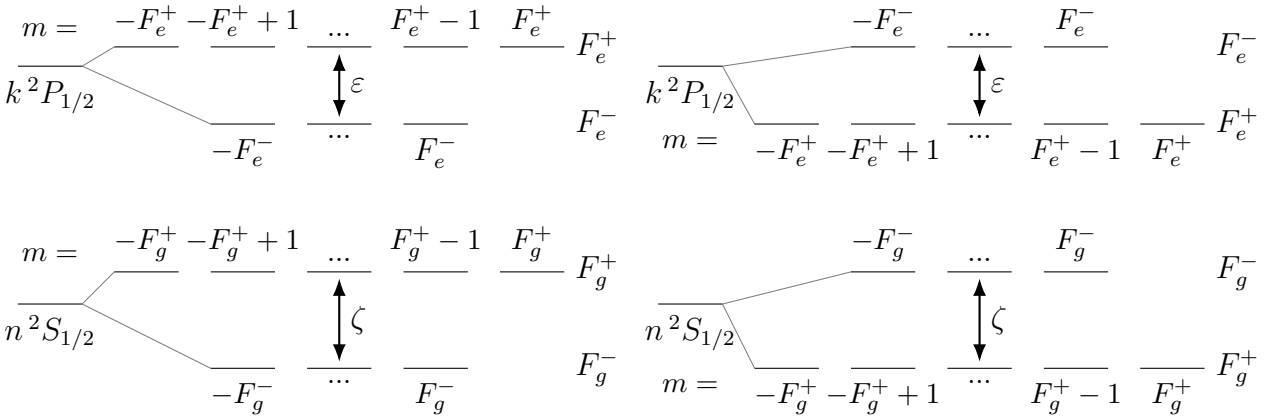

(a) $n\ ^2S_{1/2} \to k\ ^2P_{1/2}$ transitions scheme in a magnetic field, when I is a half-integer quantity.

(b) $n\ ^2S_{1/2} \to k\ ^2P_{1/2}$ transitions scheme in a magnetic field, when I is an integer quantity.

Figure 4.1: Schemes of all possible $n\ ^2S_{1/2} \to k\ ^2P_{1/2}$ transitions within magnetic field.

It should be noted that when I is an integer number the hyperfine structure is inverted.

Couple of pages before, general diagonal and non-diagonal elements of the Zeeman split matrix were mentioned [see relations 4.21 and 4.23]. Taking into account the obtained expressions for total electronic and total atomic angular momenta, these formulae could be written in more simple way. The diagonal elements of the Hamiltonian matrix H are

$$\langle F, m|\, H\, |F, m\rangle = E_0(F) - \mu_B g_F(F_{g,e}^{\pm}) m B, \tag{4.33}$$

Non-diagonal elements can be expressed in the following form:

$$\langle F, m|\, H\, |F-1, m\rangle = \langle F-1, m|\, H\, |F, m\rangle = -\frac{\mu_B}{2}\left(g_J - g_I\right) B \sqrt{1 - \left(\frac{2m}{1+2I}\right)^2}, \tag{4.34}$$

For the ground and excited states

$$g_J^g = g_S \ \text{ and } \ g_J^e = \frac{4g_L - g_S}{3}. \tag{4.35}$$

Taking into account that F quantum numbers for both ground and excited states are the same, in Eq. (4.33) we can use the following formulas for $g_F(F)$:

$$g_F(F_{g,e}^-) = g_I + \frac{g_I - g_J^{g,e}}{1+2I} \ \text{ and } \ g_F(F_{g,e}^+) = \frac{g_J^{g,e} + 2g_I I}{1+2I}. \tag{4.36}$$

For the complete description of $n\ ^2S_{1/2} \to k\ ^2P_{1/2}$ transition cancellations within a magnetic field it is enough to write general 2×2 block matrices for the ground and excited states, where each block matrix corresponds to a given value of m, using Eq. (4.33) and Eq. (4.34). We will not write Hamiltonian elements for the $m = \pm F_{g,e}$ values because they correspond to pure states and the corresponding transitions do not depend on magnetic-field value B. The zero-field energies E_0 have been chosen as references for both ground and excited states lower levels. Below, the matrix H_G describes the ground state and can be written as follows:

$$H_G = \begin{matrix} \\ \langle F_g^+, m_g| \\ \langle F_g^-, m_g| \end{matrix} \overset{\begin{matrix} |F_g^+, m_g\rangle & \qquad & |F_g^-, m_g\rangle \end{matrix}}{\begin{pmatrix} \zeta - \mu_B \dfrac{f_g}{1+2I} m_g B & \dfrac{\mu_B}{2} g_g B \sqrt{1 - \left(\dfrac{2m_g}{1+2I}\right)^2} \\ \dfrac{\mu_B}{2} g_g B \sqrt{1 - \left(\dfrac{2m_g}{1+2I}\right)^2} & -\mu_B \left(g_I + \dfrac{g_g}{1+2I}\right) m_g B \end{pmatrix}}. \tag{4.37}$$

where $g_g = g_I - g_S$ and $f_g = g_S + 2g_I I$. After diagonalization, the eigenvalues of the H_G matrix are given by

$$\Lambda_G^{\pm} = \frac{\zeta - 2\mu_B g_I m_g B}{2} \pm \frac{1}{2} \left(\zeta^2 + \mu_B^2 g_g^2 B^2 + \frac{4\zeta \mu_B g_g m_g B}{1+2I} \right)^{1/2}. \tag{4.38}$$

The eigenkets corresponding to eigenvalues $\Lambda_G^{\pm}$, expressed in terms of unperturbed state vectors $|\psi(F_g, m_g)\rangle = \sum_{F_g'} c_{F_g F_g'} |F_g', m_g\rangle$ are

$$|\psi(F_g^{\pm}, m_g)\rangle = \frac{1}{\sqrt{1+\kappa_{g\pm}^2}} |F_g^+, m_g\rangle + \frac{\kappa_{g\pm}}{\sqrt{1+\kappa_{g\pm}^2}} |F_g^-, m_g\rangle, \tag{4.39}$$

where we denoted

$$\kappa_{g\pm} = \frac{2(1+2I)(\Lambda_G^{\pm} - \zeta) + 2\mu_B f_g m_g B}{\mu_B g_g B \sqrt{(1+2I)^2 - 4m_g^2}}.$$

Similarly, for the excited state, the general 2×2 Hamiltonian block matrix is

$$H_E = \begin{matrix} \\ \langle F_e^+, m_e| \\ \langle F_e^-, m_e| \end{matrix} \overset{\begin{matrix} |F_e^+, m_e\rangle & \qquad & |F_e^-, m_e\rangle \end{matrix}}{\begin{pmatrix} \varepsilon - \mu_B \dfrac{f_e}{(1+2I)} m_e B & \dfrac{\mu_B}{2} g_e B \sqrt{1 - \left(\dfrac{2m_e}{1+2I}\right)^2} \\ \dfrac{\mu_B}{2} g_e B \sqrt{1 - \left(\dfrac{2m_e}{1+2I}\right)^2} & -\mu_B \left(g_I + \dfrac{g_e}{(1+2I)}\right) m_e B \end{pmatrix}}. \tag{4.40}$$

where $g_e = \dfrac{3g_I - 4g_L + g_S}{3}$ and $f_e = \dfrac{4g_L - g_S + 6g_I I}{3}$. The eigenvalues of H_E are

$$\Lambda_E^{\pm} = \frac{\varepsilon - 2\mu_B g_I m_e B}{2} \pm \frac{1}{2} \left(\varepsilon^2 + \mu_B^2 g_e^2 B^2 + \frac{4\varepsilon \mu_B g_e m_e B}{1+2I} \right)^{1/2}, \tag{4.41}$$

and its eigenkets, written in terms of the unperturbed atomic state vectors $\left|\psi\left(F_e, m_e\right)\right\rangle = \sum_{F'_e} c_{F_e F'_e} \left|F'_e, m_e\right\rangle$, are the following:

$$\left|\psi(F_e^{\pm}, m_e)\right\rangle = \frac{1}{\sqrt{1+\kappa_{e\pm}^2}} \left|F_e^{+}, m_e\right\rangle + \frac{\kappa_{e\pm}}{\sqrt{1+\kappa_{e\pm}^2}} \left|F_e^{-}, m_e\right\rangle, \tag{4.42}$$

where we denoted

$$\kappa_{e\pm} = \frac{2(1+2I)(\Lambda_E^{\pm} - \varepsilon) + 2\mu_B f_e m_e B}{\mu_B g_e B \sqrt{(1+2I)^2 - 4m_e^2}}.$$

Taking into account the total electronic angular momenta J_g and J_e quantum numbers for $n\ {}^2S_{1/2} \to k\ {}^2P_{1/2}$ transitions, the unperturbed transfer coefficient $a(F_e, m_e; F_g, m_g; q)$ reads

$$a(F_e, m_e; F_g, m_g; q) = (-1)^{3/2+I+F_e+F_g-m_e} \sqrt{2} \sqrt{2F_e+1} \sqrt{2F_g+1} \times \begin{pmatrix} F_e & 1 & F_g \\ -m_e & q & m_g \end{pmatrix} \begin{Bmatrix} F_e & 1 & F_g \\ 1/2 & I & 1/2 \end{Bmatrix}. \tag{4.43}$$

There are no σ^+ and σ^- transition cancellations (i.e. transfer coefficients are never equal to zero) for any value of the magnetic-field of any alkali-atom isotope. Cancellations occur only for π transitions ($m_g = m_e$). In this section from now on in formulas and equations instead of m_g and m_e we will write m. Let's examine the unperturbed transfer coefficients $a(F_e, m; F_g, m; 0)$. Two of them have the following expression:

$$a(F_e^{\pm}, m; F_g^{\pm}, m; 0) = \pm \frac{2m}{\sqrt{3}\,(1+2I)}. \tag{4.44}$$

For the next two unperturbed coefficients the expression is

$$a(F_e^{\pm}, m; F_g^{\mp}, m; 0) = \frac{1}{\sqrt{3}} \sqrt{1 - \left(\frac{2m}{1+2I}\right)^2}. \tag{4.45}$$

From Eq. (4.25), and formulas (4.44) and (4.45), modified transfer coefficients which have a cancellation are

$$\begin{aligned} a[&\left|\psi(F_e^{\pm}, m)\right\rangle, \left|\psi(F_g^{\pm}, m)\right\rangle, 0] \\ &= \frac{\kappa_{e\pm}}{\sqrt{1+\kappa_{e\pm}^2}}\ a\left(F_e^{-}, m; F_g^{-}, m; 0\right) \frac{\kappa_{g\pm}}{\sqrt{1+\kappa_{g\pm}^2}} \\ &+ \frac{\kappa_{e\pm}}{\sqrt{1+\kappa_{e\pm}^2}}\ a\left(F_e^{-}, m; F_g^{+}, m; 0\right) \frac{1}{\sqrt{1+\kappa_{g\pm}^2}} \\ &+ \frac{1}{\sqrt{1+\kappa_{e\pm}^2}}\ a\left(F_e^{+}, m; F_g^{-}, m; 0\right) \frac{\kappa_{g\pm}}{\sqrt{1+\kappa_{g\pm}^2}} \\ &+ \frac{1}{\sqrt{1+\kappa_{e\pm}^2}}\ a\left(F_e^{+}, m; F_g^{+}, m; 0\right) \frac{1}{\sqrt{1+\kappa_{g\pm}^2}}. \end{aligned} \tag{4.46}$$

The solutions of $a[|\psi(F_e^{\pm},m)\rangle,|\psi(F_g^{\pm},m)\rangle,0]=0$ are

$$B_{\pm}^{\pm}=-\frac{4m\zeta\varepsilon}{\mu_B\left(1+2I\right)\left(g_g\varepsilon+g_e\zeta\right)}. \tag{4.47}$$

The condition on the considered modified transfer coefficients solutions which defines permissible values of magnetic quantum number m depends on nuclear spin:

$$0\leq(-1)^{2I}m\leq I-\frac{1}{2}. \tag{4.48}$$

From the formula (4.47) one can notice that for isotopes having a half-integer nuclear spin, transition cancellations exist for π transitions between levels for which the magnetic quantum number is zero ($m=0$). But as the atomic states are degenerated, it is not possible to observe the cancellations of these transitions.

Modified transfer coefficients $a[|\psi(F_e^{\pm},m)\rangle,|\psi(F_g^{\mp},m)\rangle,0]$ can not be equal to zero, but these quantities have a very interesting behavior. While for certain values of B, transition intensities corresponding to $a[|\psi(F_e^{\pm},m)\rangle,|\psi(F_g^{\pm},m)\rangle,0]$ are zero (transition cancellation), the transition intensities corresponding to $a[|\psi(F_e^{\pm},m)\rangle,|\psi(F_g^{\mp},m)\rangle,0]$ reach their maximum value which corresponds to the intensity of a π transition occurring between pure states (so-called "guiding" atomic transitions [136]). This is ensured by the calculation of the derivative of modified transfer coefficients squared with respect to magnetic field:

$$\frac{\mathrm{d}a^2[|\psi(F_e^{\pm},m)\rangle,|\psi(F_g^{\mp},m)\rangle,0]}{\mathrm{d}B}=0. \tag{4.49}$$

The solution of Eq. (4.49) is exactly formula (4.47) with the condition mentioned in formula (4.48). We call quantities $a[|\psi(F_e^{\pm},m)\rangle,|\psi(F_g^{\mp},m)\rangle,0]$ and $a[|\psi(F_e^{\pm},m)\rangle,|\psi(F_g^{\pm},m)\rangle,0]$ pair-modified transfer coefficients, and transitions corresponding to them pair-transitions. As one can notice, cancellations occur only for transitions obeying $\Delta F=F_e-F_g=0$ and maximum values take place when $\Delta F=F_e-F_g=\pm1$.

4.4 Analysis of stable and long-lived isotopes $n\,^2S_{1/2}\rightarrow k\,^2P_{1/2}$ transition cancellations

In this section we fully analyze D_1 line transition cancellations and maxima of ^{23}Na, ^{39}K, ^{40}K, ^{41}K, ^{85}Rb, ^{87}Rb and ^{133}Cs atoms. In addition, we study ^{85}Rb and ^{87}Rb isotopes $5\,^2S_{1/2}\rightarrow 6\,^2P_{1/2}$ transitions. All the mentioned isotopes except ^{40}K and ^{87}Rb are stable. The half-life of ^{40}K is $1.248(3)\times10^9$ years and that of ^{87}Rb is $49.23(22)\times10^9$ years. It should be noted that we do not study all the possible isotopes of all alkali atoms mainly due to the lack of data on these isotopes and also because their half-life time is too short to envisage an experiment in the close future. However the present theory is still valid to study them.

In Table 4.1 all considered isotope data is given with uncertainties. As one can see, the most imprecise values in general are ε. But for ^{39}K, ^{40}K and ^{41}K frequency differences between

ground state levels are not precisely known. These quantities have the most influence on the size of the uncertainties of the calculated B values.

Table 4.1: Values used to calculate transitions between magnetic sublevels of $n\ ^2S_{1/2}$ and $k\ ^2P_{1/2}$ states with their uncertainties.

Isotope	I	Transition	Values
^{23}Na	3/2	$3\ ^2S_{1/2} \rightarrow 3\ ^2P_{1/2}$ (D_1 line)	$g_L = 0.999\,976\,13$ [137]
			$g_I = -0.000\,804\,610\,80(80)$ [133]
			$\zeta = 1771.626\,1288(10)$ MHz [133]
			$\varepsilon = 188.697(14)$ MHz [138, 139]
^{39}K	3/2	$4\ ^2S_{1/2} \rightarrow 4\ ^2P_{1/2}$ (D_1 line)	$g_L = 0.999\,979\,053\,396\,70(14)*$
			$g_I = -0.000\,141\,934\,89(12)$ [133]
			$\zeta = 461.73(14)$ MHz [140]
			$\varepsilon = 57.696(10)$ MHz [138]
^{40}K	4	$4\ ^2S_{1/2} \rightarrow 4\ ^2P_{1/2}$ (D_1 line)	$g_L = 0.999\,979\,745\,316\,40(14)*$
			$g_I = 0.000\,176\,490(34)$ [133]
			$\zeta = -1285.87(35)$ MHz [140]
			$\varepsilon = -155.31(35)$ MHz [140]
^{41}K	3/2	$4\ ^2S_{1/2} \rightarrow 4\ ^2P_{1/2}$ (D_1 line)	$g_L = 0.999\,980\,393\,902\,46(13)*$
			$g_I = -0.000\,077\,906\,00(8)$ [133]
			$\zeta = 253.99(12)$ MHz [133, 140, 141]
			$\varepsilon = 30.50(16)$ MHz [140]
^{85}Rb	5/2	$5\ ^2S_{1/2} \rightarrow 5\ ^2P_{1/2}$ (D_1 line)	$g_L = 0.999\,993\,54$ [82]
			$g_I = -0.000\,293\,640\,00(60)$ [133]
			$\zeta = 3035.732\,4390(60)$ MHz [133, 142]
			$\varepsilon = 361.58(17)$ MHz [142–144]
^{85}Rb	5/2	$5\ ^2S_{1/2} \rightarrow 6\ ^2P_{1/2}$	$g_L = 0.999\,993\,54$ [82]
			$g_I = -0.000\,293\,640\,00(60)$ [133]
			$\zeta = 3035.732\,4390(60)$ MHz [133, 142]
			$\varepsilon = 117.33(66)$ MHz [145]
^{87}Rb	3/2	$5\ ^2S_{1/2} \rightarrow 5\ ^2P_{1/2}$ (D_1 line)	$g_L = 0.999\,993\,69$ [83]
			$g_I = -0.000\,995\,1414(10)$ [133]
			$\zeta = 6834.682\,610\,904\,290(90)$ MHz [146]
			$\varepsilon = 814.50(13)$ MHz [133, 143, 144]
^{87}Rb	3/2	$5\ ^2S_{1/2} \rightarrow 6\ ^2P_{1/2}$	$g_L = 0.999\,993\,69$ [83]
			$g_I = -0.000\,995\,1414(10)$ [133]
			$\zeta = 6834.682\,610\,904\,290(90)$ MHz [146]
			$\varepsilon = 265.12(66)$ MHz [145]

Continued on next page

Table 4.1 – *Continued from previous page*

Isotope	I	Transition	Landé factors
^{133}Cs	7/2	$6\ ^2S_{1/2} \rightarrow 6\ ^2P_{1/2}$ (D_1 line)	$g_L = 0.999\,995\,87$ [74]
			$g_I = -0.000\,398\,853\,95(52)$ [133]
			$\zeta = 9192.631\,770$ MHz (exact) [74]
			$\varepsilon = 1167.680(30)$ MHz [147, 148]

It should be noted that when the value of I is integer (i.e. ^{40}K in this thesis), the values of ζ and ε should have the minus sign to be in agreement with our notations. For further calculations, for the Bohr magneton and g_S spin Landé factor we used $\mu_B/h = -1.399\,624\,5042(86)$ MHz/G and $g_S = 2.002\,319\,304\,3622(15)$ [149] values respectively. In Ref. [34], where cancellations of rubidium $5\ ^2S_{1/2} \rightarrow 6\ ^2P_{1/2,\,3/2}$ transitions were examined, we noticed that the value of this fundamental constant had just been refined, thus we used the following one: $\mu_B/h = -1.399\,624\,493\,61(42)$ MHz/G [150]. It is important to emphasize that this difference, which only affects one millionth of the Bohr magneton, only causes an infinitesimal modification to the values of the B-field.

In Table 4.1, * stands for the calculated values of g_L using the exact formula of Phillips [151] and values for the isotopes of Audi *et al.* [152]. We noticed that in the paper of Phillips [151] $1/m$ is missing in the second term of the exact formula for g_L.

Below, on Figure 4.2, ^{23}Na, ^{39}K and ^{41}K isotopes D_1 line π transition cancellations are depicted. The total atomic angular momentum magnitude is $F = 1$ for the lower levels of ground and excited states and $F = 2$ for the upper levels. For all these isotopes, transitions cancel only for $m = -1$.

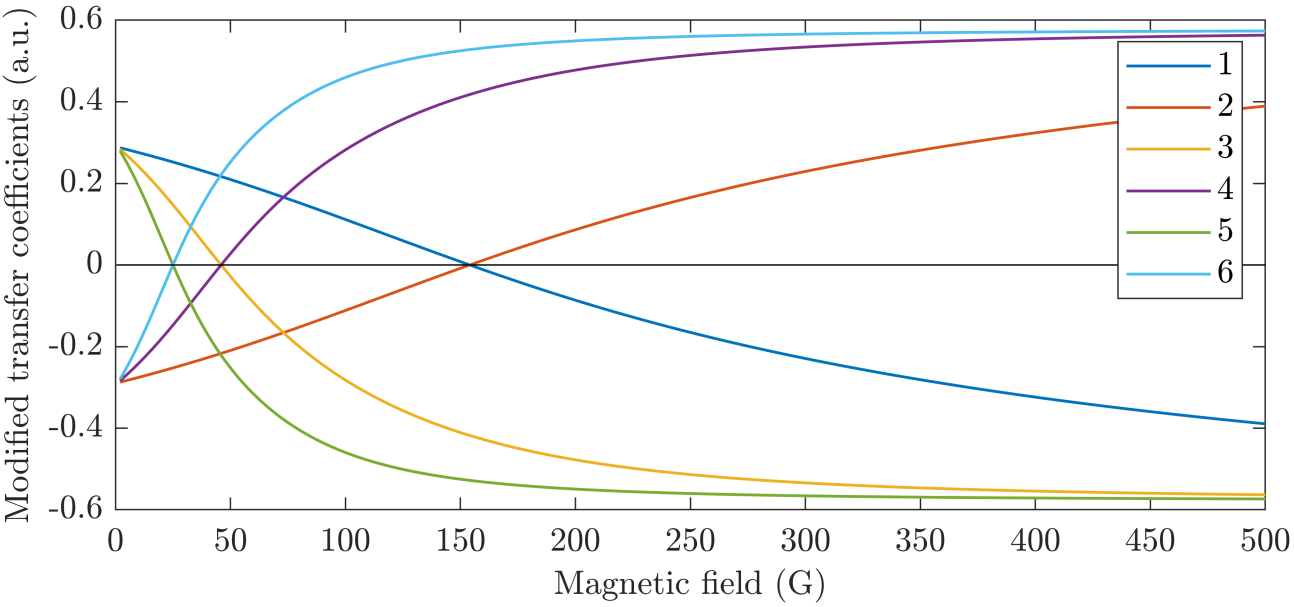

Figure 4.2: ^{23}Na, ^{39}K and ^{41}K isotopes D_1 line π transition modified transfer coefficients for $m = -1$. Numbering given in the inset is defined in Table 4.2.

One can note that $I = 3/2$ also for ^{87}Rb, but to provide a good readability of the thesis we will consider D_1 line and $5\ ^2S_{1/2} \rightarrow 6\ ^2P_{1/2}$ transition cancellations of this isotope together. Obviously all the figures in this chapter, which show transition cancellations, have been drawn without taking into account uncertainties of the involved quantities.

Table 4.2: B-field values canceling transitions of ^{23}Na, ^{39}K and ^{41}K with their uncertainties.

Isotope	No.	F	m	B (G)	B^* (G)
^{23}Na	1	1	-1	153.2007(86)	153.2007024(11)
	2	2	-1	153.2007(86)	153.2007024(11)
^{39}K	3	1	-1	44.991(10)	44.9915(37)
	4	2	-1	44.991(10)	44.9915(37)
^{41}K	5	1	-1	24.042(95)	24.0418(30)
	6	2	-1	24.042(95)	24.0418(30)

In Table 4.2 all B-field values which cancel D_1 line transitions of ^{23}Na, ^{39}K and ^{41}K are calculated. The numbers in the second column refer to the labeling of Figure 4.2, the third column shows the values of the total angular momentum magnitude for both ground and excited states. The fourth column indicates between which magnetic sublevels the transition occurs and the fifth column displays calculated values of B-field with their uncertainties, which are a consequence of the physical quantities uncertainties involved in the calculations. The B^* value in the sixth column is obtained by ignoring the uncertainty on ε. This calculation has been made in order to show how precise the B values that cancel the transitions can be determined if the uncertainty on ε could be reduced. As immediate consequence, one sees the importance to determine experimentally an improved, i.e. more precise, value of ε. From this very precisely known ε value, it becomes clear that B^* can be useful for the calibration of magnetometers.

For ^{40}K the total atomic angular momentum magnitude is $F = 9/2$ for the lower levels of ground and excited states and $F = 7/2$ for the upper levels. Transition cancellations are observed for $m = 7/2$, $m = 5/2$, $m = 3/2$ and $m = 1/2$. In Table 4.3 all B-field values which cancel transitions of ^{40}K D_1 line are calculated.

Table 4.3: B-field values canceling transitions of ^{40}K with their uncertainties.

Isotope	No.	F	m	B (G)	B^* (G)
^{40}K	1	9/2	7/2	190.20(33)	190.204(13)
	2	7/2	7/2	190.20(33)	190.204(13)
	3	9/2	5/2	135.85(24)	135.8602(98)
	4	7/2	5/2	135.85(24)	135.8602(98)
	5	9/2	3/2	81.51(15)	81.5161(59)
	6	7/2	3/2	81.51(15)	81.5161(59)
	7	9/2	1/2	27.171(48)	27.1720(19)
	8	7/2	1/2	27.171(48)	27.1720(19)

On Figure 4.3, modified transfer coefficients for all π transitions which have a cancellation are depicted.

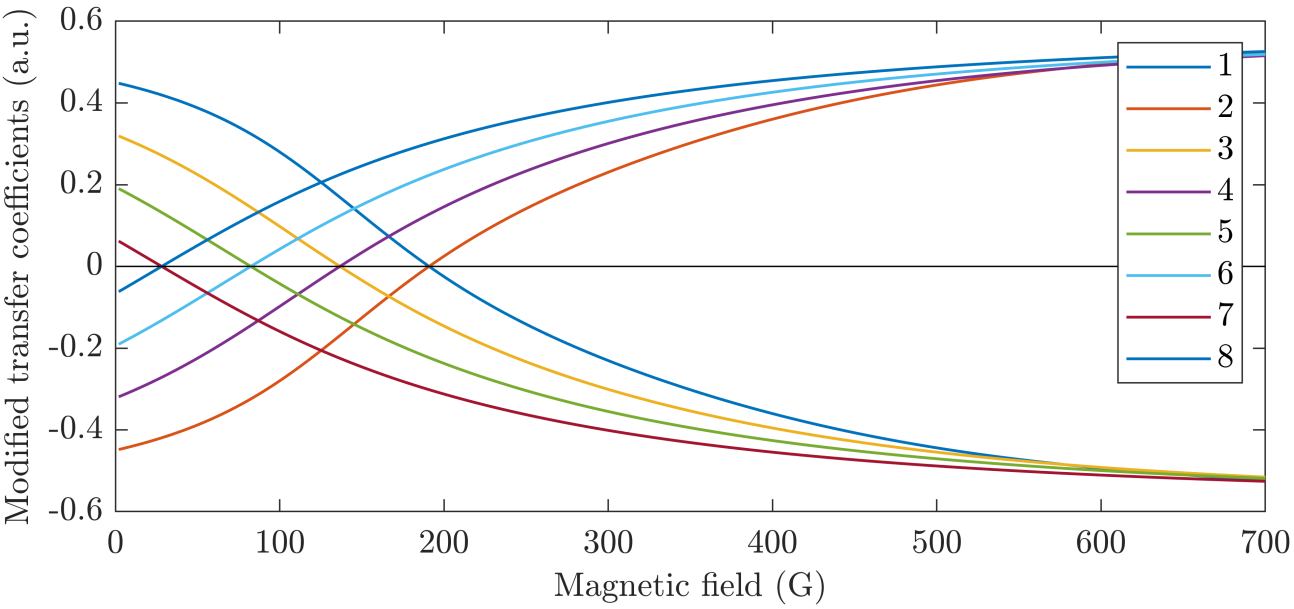

Figure 4.3: ^{40}K D_1 line π transition coefficients which have a cancellation. Cancellations are observed for $m = 7/2$, $m = 5/2$, $m = 3/2$ and $m = 1/2$. Numbering given in the inset is defined in Table 4.3.

Next we examine ^{85}Rb $5\ ^2S_{1/2} \rightarrow 5\ ^2P_{1/2}$ and $5\ ^2S_{1/2} \rightarrow 6\ ^2P_{1/2}$ π transitions. For this isotope the total atomic angular momentum magnitude is $F = 2$ for the lower levels of ground and excited states and $F = 3$ for the upper levels. Some transitions cancel for $m = -2$ and $m = -1$.

For this isotope we will also analyze those transitions which have maximum value as it was mentioned before. π transitions corresponding to the above-mentioned magnetic quantum numbers which do not cancel reach their maximum values for the magnetic-field values canceling the other transitions. On Figure 4.4 (a.1) and (b.1), modified transfer coefficients (i.e. $a[|\psi(F_e, m)\rangle, |\psi(F_g, m)\rangle, 0]$ quantities) are depicted for $m = -2$ and $m = -1$ for both $5\ ^2S_{1/2} \rightarrow 5\ ^2P_{1/2}$ and $5\ ^2S_{1/2} \rightarrow 6\ ^2P_{1/2}$ transitions. Lines numbered 5, 6, 7 and 8 have no cancellation and are nothing more than transition coefficients between ground and excited states, where $F_g \neq F_e$. As an illustration, the dashed line on Figure 4.4 (a.1) indicates that the intensity of transitions 1 and 2 is equal to zero for the same value of B. On Figure 4.4 (a.2) and (b.2), modified transfer coefficients squared are depicted in order to compare them with each other and with guiding atomic transition coefficient for which $m = -3$. To extend the previous illustration with the dashed line of Figure 4.4 (a.2), we draw it in the case of the modified transfer coefficients squared to show explicitly that the minimum of transitions 1 and 2 (point A) coincides with the maximum of transitions 5 and 6 (point B).

In Table 4.4 all B-field values which cancel transitions of ^{85}Rb D_1 line ($5\ ^2S_{1/2} \rightarrow 5\ ^2P_{1/2}$) and $5\ ^2S_{1/2} \rightarrow 6\ ^2P_{1/2}$ are calculated. One also can see that for these values of magnetic-field the transitions 5, 6, 7 and 8 (Table 4.5) reach their maximum value equal to the transfer coefficient 9 squared.

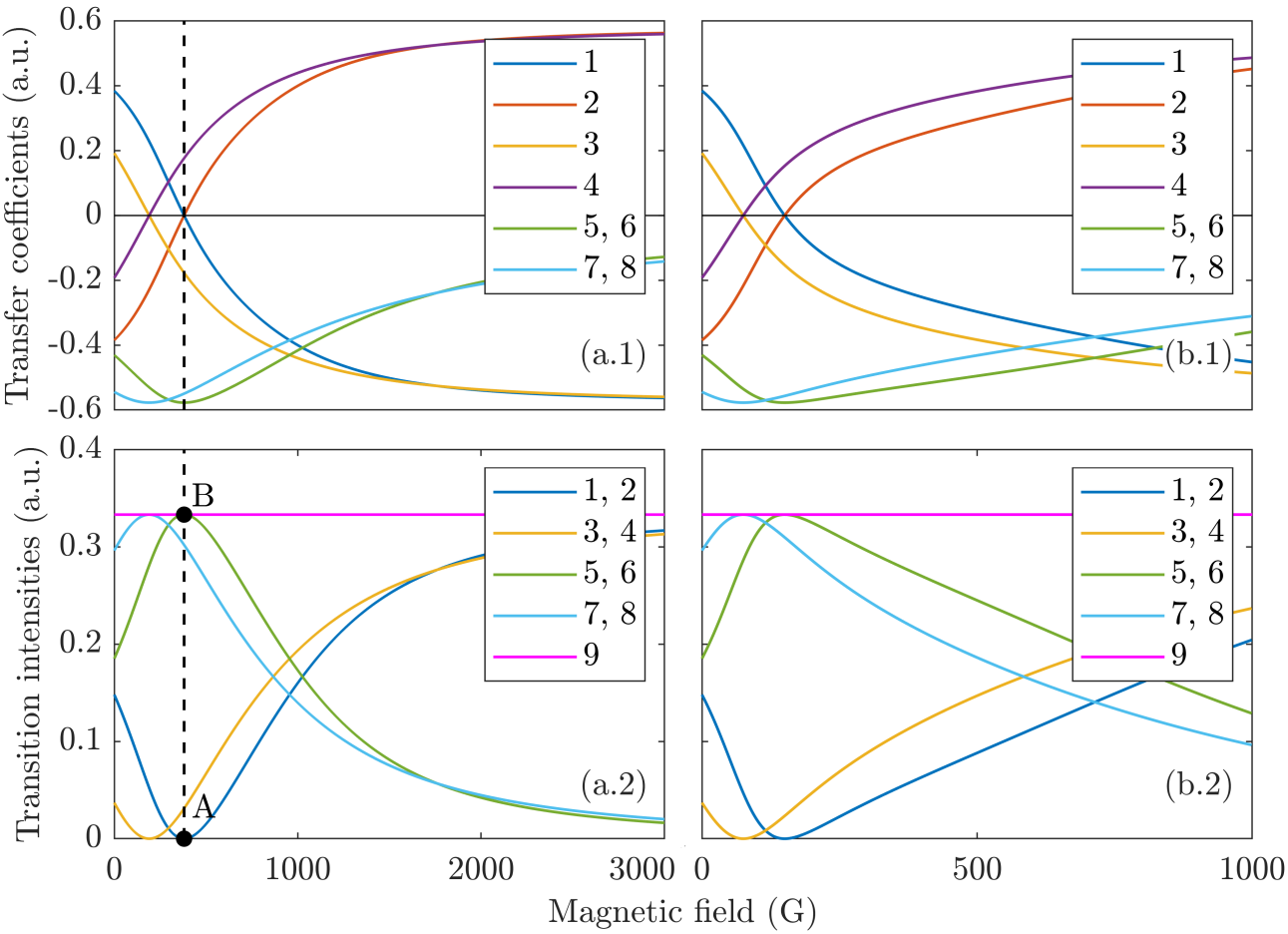

Figure 4.4: (a.1) ^{85}Rb D_1 line modified transfer coefficients for $m = -2$ and $m = -1$ π transitions. For this isotope four cancellations exist: 1, 2, 3 and 4. (a.2) ^{85}Rb D_1 line modified transfer coefficients squared for $m = -3, -2$ and -1. The vertical dashed line indicates the value $B = 380.73$ G which corresponds to the cancellation of the transitions 1, 2 (point A) and coincides with the maximum of transitions 5, 6 (point B). On sub-figures (b.1) and (b.2) for 5 $^2S_{1/2} \rightarrow 6\ ^2P_{1/2}$ transition modified transfer coefficients and modified transfer coefficients squared are depicted. Numbering 1-8 given in the inset are defined in Tables 4.4 and 4.5, guiding transition transfer coefficient squared 9 on sub-figures (a.2) and (b.2) corresponds to $m = -3$.

Table 4.4: B-field values canceling ^{85}Rb 5 $^2S_{1/2} \rightarrow 5\ ^2P_{1/2}$ and 5 $^2S_{1/2} \rightarrow 6\ ^2P_{1/2}$ π transitions with their uncertainties.

Isotope	Excited state	No.	F	m	B (G)	B^* (G)
^{85}Rb	5 $^2P_{1/2}$	1	1	-2	380.73(13)	380.7362466(29)
		2	2	-2	380.73(13)	380.7362466(29)
		3	1	-1	190.368(66)	190.3681233(15)
		4	2	-1	190.368(66)	190.3681233(15)
	6 $^2P_{1/2}$	1	1	-2	150.31(76)	150.31738954(20)
		2	2	-2	150.31(76)	150.31738954(20)
		3	1	-1	75.15(38)	75.15869477(10)
		4	2	-1	75.15(38)	75.15869477(10)

Table 4.5: B-field values maximizing ^{85}Rb $5\ ^2S_{1/2} \rightarrow 5\ ^2P_{1/2}$ and $5\ ^2S_{1/2} \rightarrow 6\ ^2P_{1/2}$ π transitions with their uncertainties.

Isotope	Excited state	No.	ΔF	m	B (G)	B^* (G)
^{85}Rb	$5\ ^2P_{1/2}$	5	-1	-2	380.73(13)	380.7362466(29)
		6	1	-2	380.73(13)	380.7362466(29)
		7	-1	-1	190.368(66)	190.3681233(15)
		8	1	-1	190.368(66)	190.3681233(15)
	$6\ ^2P_{1/2}$	5	-1	-2	150.31(76)	150.31738954(20)
		6	1	-2	150.31(76)	150.31738954(20)
		7	-1	-1	75.15(38)	75.15869477(10)
		8	1	-1	75.15(38)	75.15869477(10)

On Figure 4.5, on the left side $5\ ^2S_{1/2} \rightarrow 5\ ^2P_{1/2}$ and on the right side $5\ ^2S_{1/2} \rightarrow 6\ ^2P_{1/2}$ all possible π transition transfer coefficients and transition intensities of ^{87}Rb isotope for $m = -1$ value are depicted.

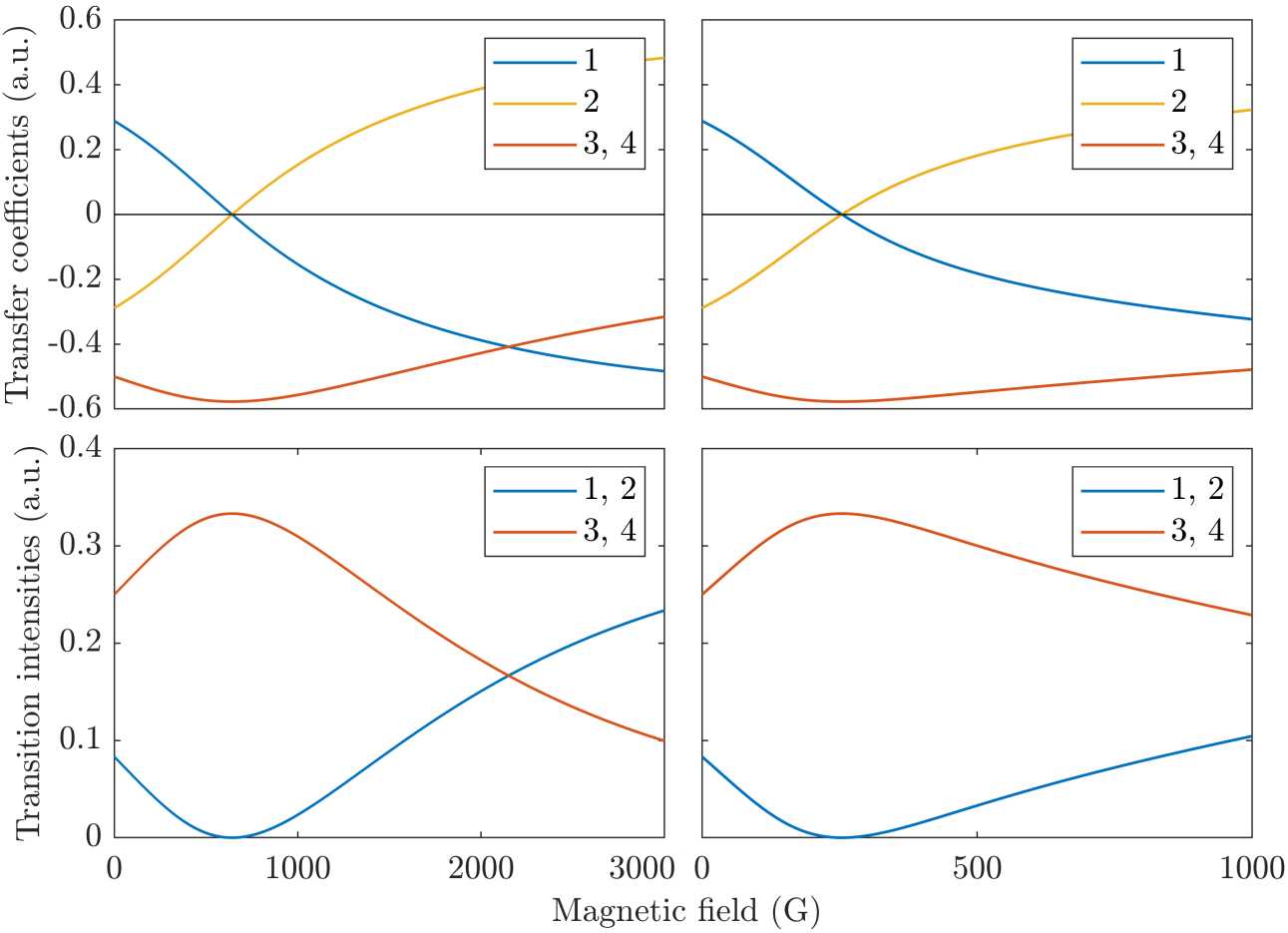

Figure 4.5: ^{87}Rb $5\ ^2S_{1/2} \rightarrow 5\ ^2P_{1/2}$ (left side) and $5\ ^2S_{1/2} \rightarrow 6\ ^2P_{1/2}$ (right side) π transition transfer coefficients and transition intensities for $m = -1$ magnetic quantum number.

The values for ^{87}Rb, for which the contribution of the magnetic field cancels π transitions for $m = -1$ is $B = 642.590(76)$ G for the $5\ ^2S_{1/2} \rightarrow 5\ ^2P_{1/2}$ and $B = 254.39(57)$ G for the

$5\ ^2S_{1/2} \rightarrow 6\ ^2P_{1/2}$. In Table 4.6 these values are written with corresponding ground and excited states F quantum number. Again, in column 7, B^* is calculated without taking into account the uncertainty on ε.

Table 4.6: Magnetic-field values canceling ^{87}Rb $5\ ^2S_{1/2} \rightarrow 5\ ^2P_{1/2}$ and $5\ ^2S_{1/2} \rightarrow 6\ ^2P_{1/2}$ π transitions.

Isotope	Excited state	No.	F	m	B (G)	B^* (G)
^{87}Rb	$5\ ^2P_{1/2}$	1	1	-1	642.590(76)	642.5904743(48)
		2	2	-1	642.590(76)	642.5904743(48)
	$6\ ^2P_{1/2}$	1	1	-1	254.39(57)	254.398160387(80)
		2	2	-1	254.39(57)	254.398160387(80)

Once again it is necessary to note, that for every isotope's canceling transition there is another one for the same value of magnetic quantum number m maximizing for exactly the same B-field value as it was mentioned in Section 4.3, Eq. (4.49).

For ^{133}Cs, the total atomic angular momentum magnitude is $F = 3$ for the lower levels of ground and excited states and $F = 4$ for the upper levels. Transition cancellations are observed for $m = -3$, $m = -2$ and $m = -1$. On Figure 4.6, modified transfer coefficients for all π transitions which have a cancellation are shown.

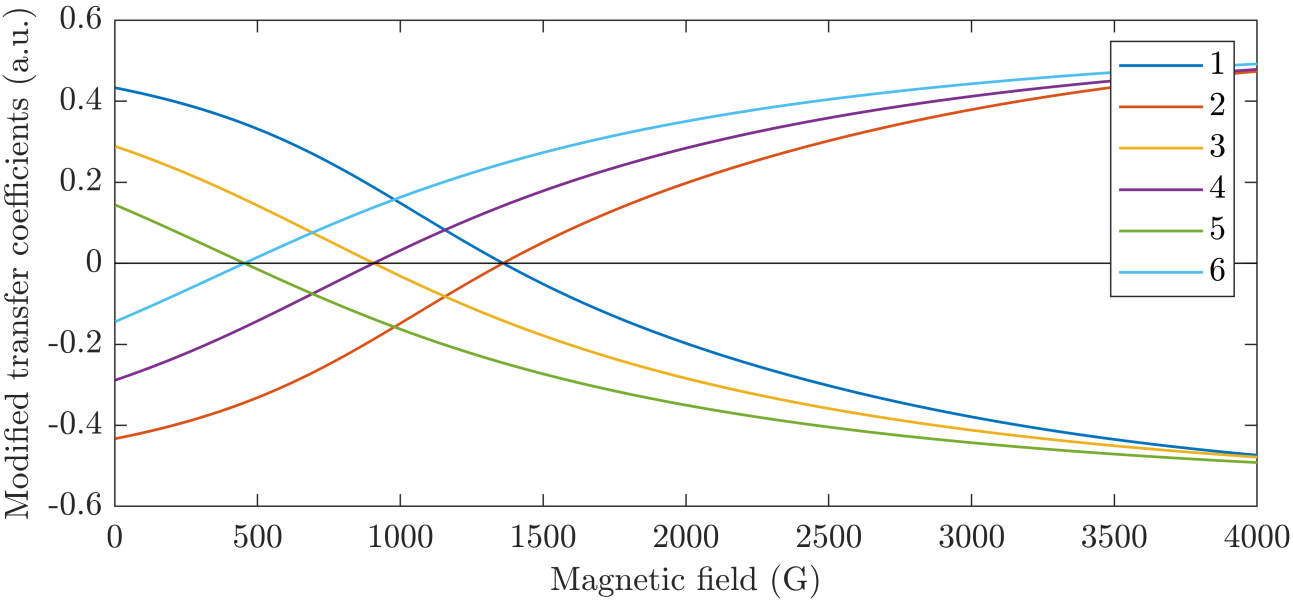

Figure 4.6: ^{133}Cs D_1 line π transition modified coefficients which have a cancellation. Cancellations are observed for $m = -3$, $m = -2$ and $m = -1$. Numbering given in the inset is defined in Table 4.7.

In Table 4.7 all B-field values which cancel transitions of ^{133}Cs D_1 line are calculated. Despite the fact that in general the uncertainty of the ground state energy has a smaller contribution on the uncertainty of the B-field value than the uncertainty of the excited one, the formula works much more better for ^{133}Cs isotope as the ground state energy is known precisely [see Table 4.1].

Table 4.7: B-field values canceling transitions of ^{133}Cs with their uncertainties.

Isotope	No.	F	m	B (G)	B^* (G)
^{133}Cs	1	3	-3	1359.237(26)	1359.2372467(92)
	2	4	-3	1359.237(26)	1359.2372467(92)
	3	3	-2	906.158(17)	906.1581644(61)
	4	4	-2	906.158(17)	906.1581644(61)
	5	3	-1	453.0790(84)	453.0790822(31)
	6	4	-1	453.0790(84)	453.0790822(31)

As an illustration of our calculations we have computed one spectrum for the value $B = 150.31739$ G that cancels the transition $|F_g = 2, m_g = -2\rangle \rightarrow |F_e = 2, m_e = -2\rangle$ between states $5\ ^2S_{1/2}$ and $6\ ^2P_{1/2}$, and two other spectra for the values $B = 125$ G and $B = 175$ G. The peak no. 1 is the one canceling for the mentioned exact value of B-field and according to the equations derived in the previous section, the peak no. 2 is maximizing for the same value of the magnetic-field [see Figure 4.7 for the numbering]. These spectra, depicted on the Figure 4.8, have been obtained by simulating a dSR experiment performed with a nanocell of length $l = 211$ nm at the temperature of 403 K. As it was mentioned before, the wavelength of ^{85}Rb $5\ ^2S_{1/2} \rightarrow 6\ ^2P_{1/2}$ transition is $\lambda = 422$ nm. The best coincidence between theory and experiment is reached when the nanocell length is the half length of the wavelength. The atomic density in the case of nanocell corresponding to 403 K is 10^{13} cm^{-3}. For the simulation we used a continuous wave 0.1 mW power laser. More detailed explanations and relations used to obtain these spectra can be found in the thesis of Klinger [70]. It is worth to mention that these spectra indicate clearly the probable experimental difficulty to determine the B-values which cancel the transitions considered in this chapter.

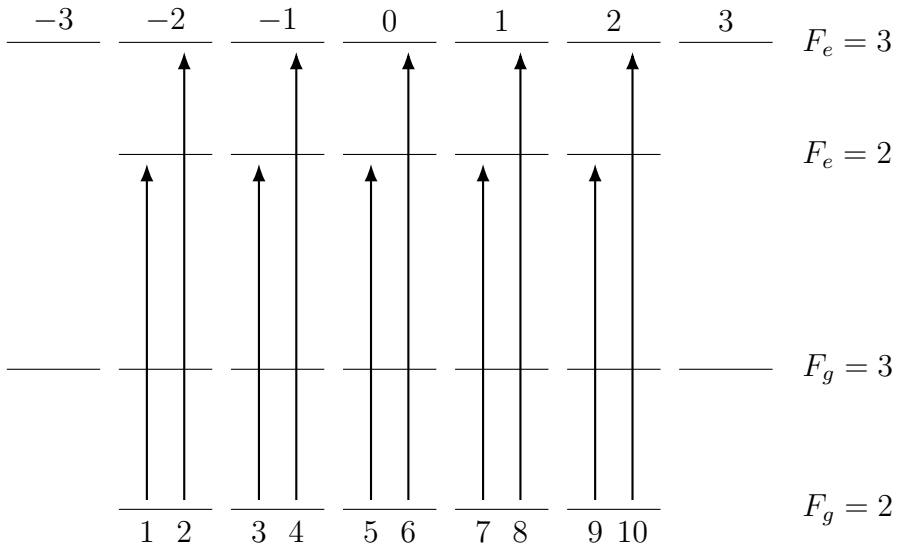

Figure 4.7: ^{85}Rb $5\ ^2S_{1/2} \rightarrow 6\ ^2P_{1/2}$ scheme in a magnetic field with all π transitions from $F_g = 2$ level to $F_e = 2$ and $F_e = 3$ levels.

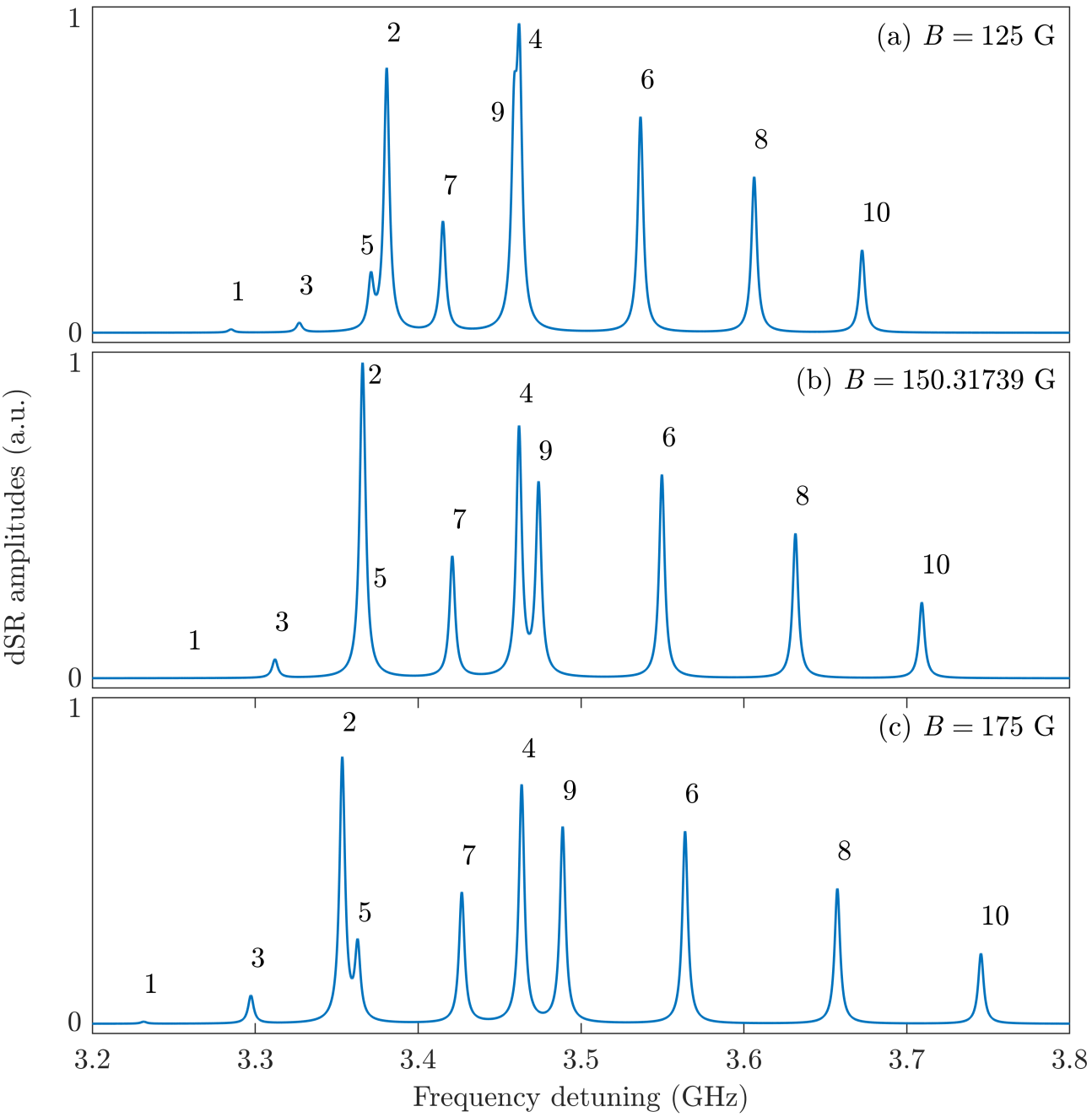

Figure 4.8: ^{85}Rb $5\,^2S_{1/2} \rightarrow 6\,^2P_{1/2}$ π transitions spectra in a magnetic field. (a) $B = 125$ G, (b) $B = 150.31739$ G, (c) $B = 175$ G. Atomic density = 10^{13} cm^{-3}, laser power = 0.1 mW, laser wavelength = 422 nm, nanocell length = 211 nm, temperature = 403 K.

4.5 Magnetic-field values canceling 87 and 85 rubidium $5\,^2S_{1/2} \rightarrow 5\,^2P_{3/2}$ and $5\,^2S_{1/2} \rightarrow 6\,^2P_{3/2}$ transitions

In this section the $5\,^2S_{1/2} \rightarrow 5\,^2P_{3/2}$ and $5\,^2S_{1/2} \rightarrow 6\,^2P_{3/2}$ transitions for both ^{87}Rb and ^{85}Rb isotopes are considered. As mentioned before, we will present only those transitions, and respectively modified transfer coefficients, which have a cancellation.

Indeed, transitions are canceled for extremely precise values of the magnetic-field. However,

when using a computer program, these values verifying $a^2[|\psi(F_e, m_e)\rangle\,;|\psi(F_g, m_g)\rangle\,;q] = 0$ will never be reached no matter the step of variation ΔB used. This situation will be even more evident in the case of 3×3 and 4×4 matrices, since in these cases, we can hardly hope to obtain simple and compact formulas, function of the variables of our model, and giving the value of the field B which cancels a transition. Only numerical values, also extremely precise, can be given and the change of sign of the quantity $a[|\psi(F_e, m_e)\rangle\,;|\psi(F_g, m_g)\rangle\,;q]$ ensures the nullity of its square.

It is very important to note that we also did a numerical simulation for 2×2 matrices. Analytically calculated values of magnetic-field and the values which are obtained by numerical simulation are in very good agreement. The adequacy of these two values is 10^{-12} and it means that we are completely allowed to use the same code for numerical simulation in the case of 3×3 or 4×4 block matrices in order to find extremely precise values of magnetic-field, which contribute to transition cancellations (eigenvalues of 3×3 and 4×4 matrices are given by Cardano and Ferrari's formulas [135], which in our case, do not seem to be possible to simplify. Consequently formulas, in the case of 3×3 and 4×4 matrices, for the B-field that cancel transitions, exist, however it is not sure that it is possible to write them in a short, compact form pages.).

4.5.1 Analysis of the ^{87}Rb transitions

We denote ζ the frequency difference between the ground states. For the excited states, notations are shown on Figure 4.9. For ^{87}Rb, from the ground state to the $5\ ^2P_{3/2}$ and $6\ ^2P_{3/2}$ excited states only ten π transitions have a cancellation, five for each of them.

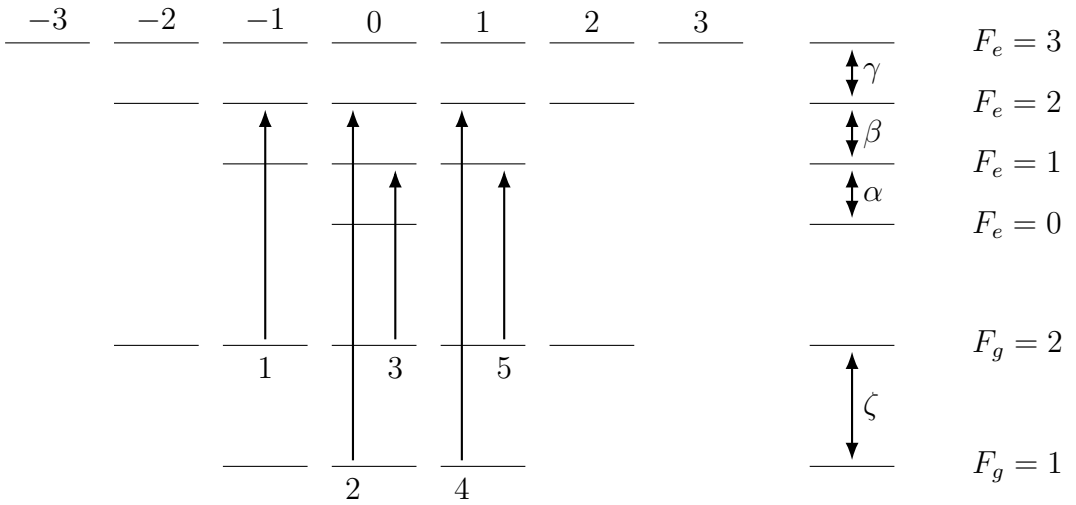

Figure 4.9: ^{87}Rb $5\ ^2S_{1/2} \rightarrow 5\ ^2P_{3/2}$ and $5\ ^2S_{1/2} \rightarrow 6\ ^2P_{3/2}$ scheme in a magnetic field with all π transitions which have a cancellation.

As already explained above, in this section we will not derive analytical formulas for the magnetic-field values which cancel transitions due to the complexity of calculations which involve 3×3 or 4×4 matrices. For the numerical calculations we used values from Table 4.8.

Here too, all excited state frequency differences have relatively big uncertainties compared with others quantities involved in the calculations. In fact, this results can serve to determine more precisely excited state frequency differences. One of the possible techniques is the selective reflection (SR) or/and transmission spectra. By making a fitting between theory and experiment it is possible to improve the following quantities: ε for the 5 $^2P_{1/2}$ and 6 $^2P_{1/2}$, and α, β, γ for the 5 $^2P_{3/2}$ and 6 $^2P_{3/2}$ excited states.

Table 4.8: Excited state frequency differences for ^{87}Rb and ^{85}Rb 5 $^2P_{3/2}$ and 6 $^2P_{3/2}$ states with their uncertainties.

Atom	Excited state	Frequency difference (MHz)	References
^{87}Rb	5 $^2P_{3/2}$	$\alpha = 72.2180(40)$	[153]
		$\beta = 156.9470(70)$	
		$\gamma = 266.6500(90)$	
	6 $^2P_{3/2}$	$\alpha = 23.744(28)$	[145]
		$\beta = 51.445(25)$	
		$\gamma = 87.050(23)$	
^{85}Rb	5 $^2P_{3/2}$	$\alpha' = 29.372(90)$	[133, 143]
		$\beta' = 63.401(61)$	
		$\gamma' = 120.640(68)$	
	6 $^2P_{3/2}$	$\alpha' = 9.802(25)$	[145]
		$\beta' = 20.850(24)$	
		$\gamma' = 39.265(23)$	

In Table 4.8 for ^{85}Rb α' is the frequency difference between $F_e = 2$ and $F_e = 1$ excited states, β' is the frequency difference between $F_e = 3$ and $F_e = 2$ excited states and γ' is the frequency difference between $F_e = 4$ and $F_e = 3$ excited states.

On Figures 4.10 and 4.11 are depicted all ^{87}Rb 5 $^2S_{1/2} \rightarrow 5\ ^2P_{3/2}$ and 5 $^2S_{1/2} \rightarrow 6\ ^2P_{3/2}$ π transitions which cancel for a certain value of the magnetic-field. For both of these transitions there are no cancellations for the same value of B-field, unlike $n\ ^2S_{1/2} \rightarrow k\ ^2P_{1/2}$ transitions.

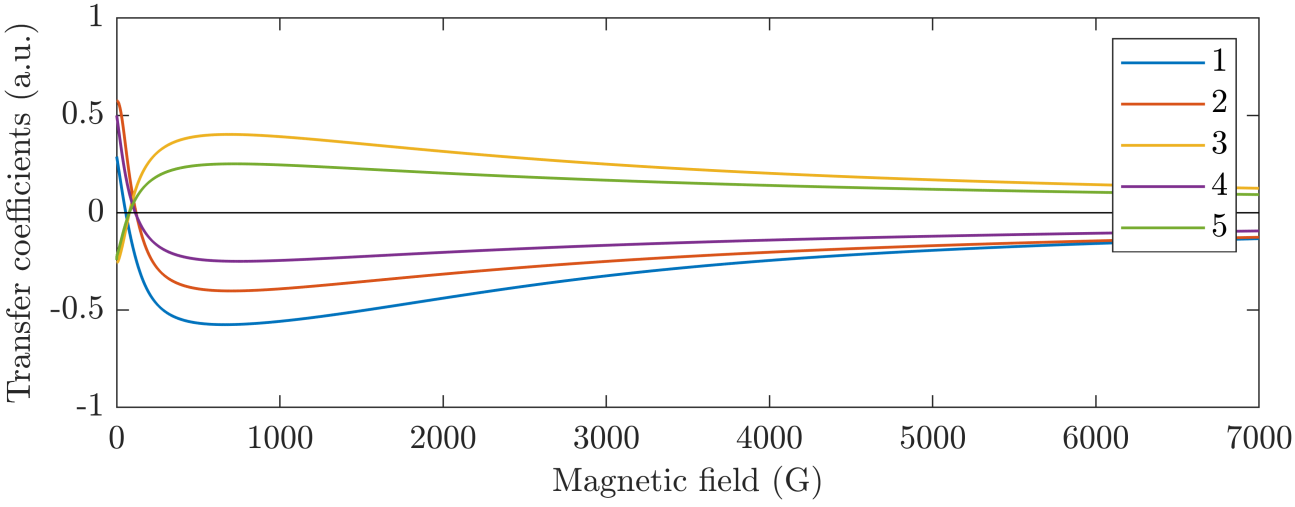

Figure 4.10: ^{87}Rb D_2 line π transfer coefficients which have a cancellation.

The transitions which have a cancellation are depicted on Figures 4.10, 4.11, 4.13, 4.14, 4.16 and 4.17. Started from 4000 G transfer coefficients become very small and for 7000 G the patterns of lines are very close to the asymptotic behavior.

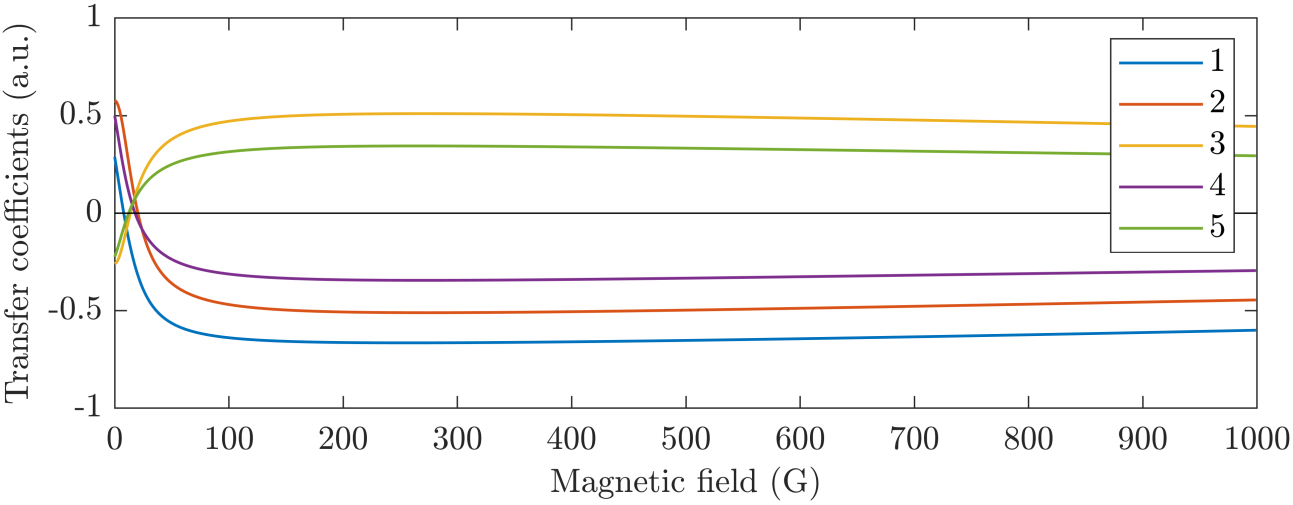

Figure 4.11: ^{87}Rb 5 $^2S_{1/2} \rightarrow$ 6 $^2P_{3/2}$ π transfer coefficients which have a cancellation.

In Tables 4.9 and 4.10 magnetic-field values which cancel 5 $^2S_{1/2} \rightarrow$ 5 $^2P_{3/2}$ and 5 $^2S_{1/2} \rightarrow$ 6 $^2P_{3/2}$ π transitions are given respectively. First column shows the numbering according to the scheme depicted on Figure 4.9, second and third columns show ground and excited level total atomic angular quantum number values respectively. Column 4 expresses magnetic quantum number value for the ground state. Column 5 was calculated using all the uncertainties of involved quantities. Column 6 expresses magnetic-field values without taking into account excited states uncertainties (i.e. we assume, that α, β and γ have no uncertainties), and column 7 shows on which frequency differences between excited states the uncertainty of magnetic-field value depends on according to Figure 4.9.

Table 4.9: Magnetic-field values canceling π transitions for ^{87}Rb D_2 line.

No.	F_g	F_e	m_g	B (G)	B^* (G)	ΔE_e
1	2	2	-1	55.6964(22)	55.69646550(39)	β, γ
2	1	2	0	118.7058(51)	118.70586363(82)	α, β, γ
3	2	1	0	77.5048(35)	77.50487199(54)	α, β, γ
4	1	2	1	114.2418(50)	114.24183482(79)	β, γ
5	2	1	1	77.2414(35)	77.24147013(54)	β, γ

Table 4.10: Magnetic-field values canceling ^{87}Rb 5 $^2S_{1/2} \rightarrow$ 6 $^2P_{3/2}$ π transitions.

No.	F_g	F_e	m_g	B (G)	B^* (G)	ΔE_e
1	2	2	-1	17.8789(60)	17.8789466978(55)	β, γ

Continued on next page

Table 4.10 – *Continued from previous page*

No.	F_g	F_e	m_g	B (G)	B^* (G)	ΔE_e
2	1	2	0	38.152(19)	38.152597093(12)	α, β, γ
3	2	1	0	24.724(13)	24.7247536874(76)	α, β, γ
4	1	2	1	36.224(15)	36.224262166(11)	β, γ
5	2	1	1	24.289(11)	24.2896121953(75)	β, γ

Below, on Figure 4.12 are shown all $5\ ^2S_{1/2} \rightarrow 5\ ^2P_{3/2}$ and $5\ ^2S_{1/2} \rightarrow 6\ ^2P_{3/2}$ σ^+ transitions, which have a cancellation. There are only 8 transitions for each one, and one of them, No. 3, is so-called forbidden. But due to the coupling of total atomic angular momenta (F) this transition becomes possible.

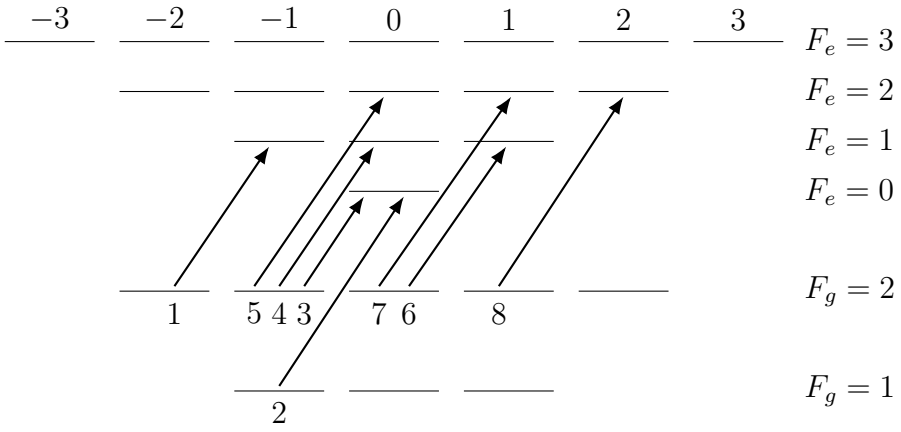

Figure 4.12: ^{87}Rb $5\ ^2S_{1/2} \rightarrow 5\ ^2P_{3/2}$ and $5\ ^2S_{1/2} \rightarrow 6\ ^2P_{3/2}$ scheme in a magnetic field with all σ^+ transitions which have a cancellation.

Figure 4.13 and Figure 4.14 demonstrate ^{87}Rb $5\ ^2S_{1/2} \rightarrow 5\ ^2P_{3/2}$ and $5\ ^2S_{1/2} \rightarrow 6\ ^2P_{3/2}$ σ^+ transfer coefficients which cancel for a certain value of the magnetic-field. Transfer coefficients are labeled accordingly with Figure 4.12.

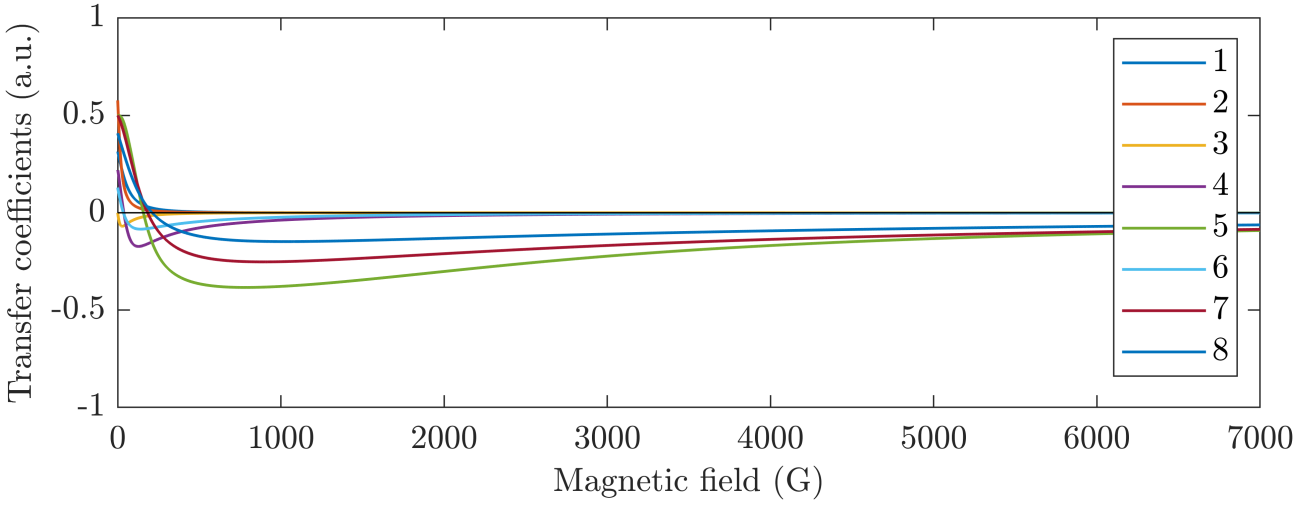

Figure 4.13: ^{87}Rb D_2 line σ^+ transfer coefficients which have a cancellation.

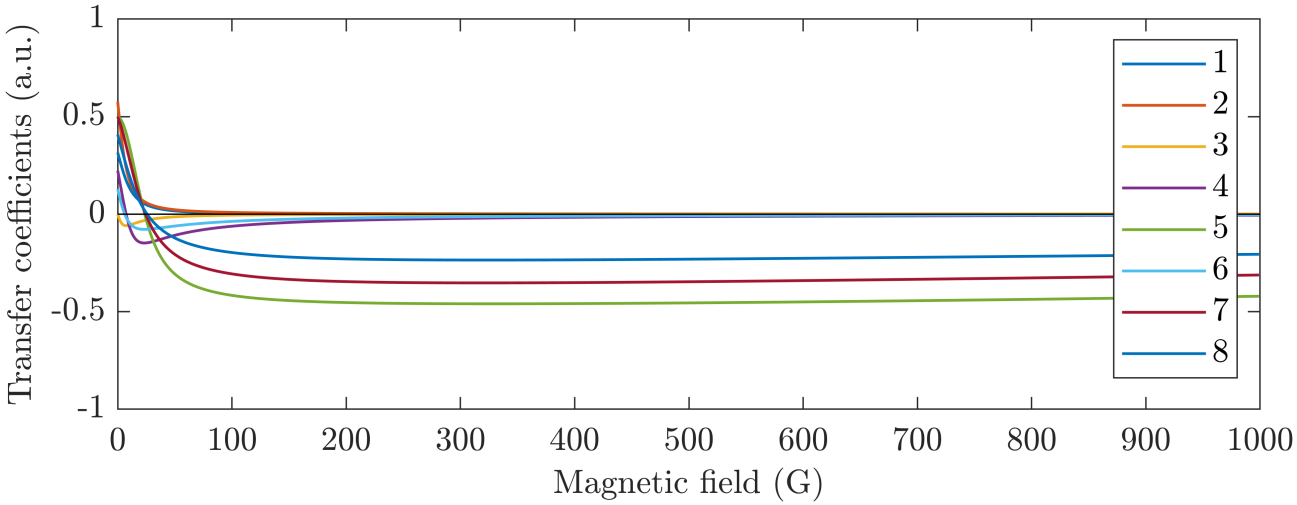

Figure 4.14: ^{87}Rb 5 $^2S_{1/2} \rightarrow 6\ ^2P_{3/2}$ σ^+ transfer coefficients which have a cancellation.

Table 4.11 indicates magnetic-field values which cancel certain σ^+ transitions ^{87}Rb D_2 line. Table 4.12 indicates magnetic-field values canceling ^{87}Rb 5 $^2S_{1/2} \rightarrow 6\ ^2P_{3/2}$ σ^+ transitions. Columns 5 (B) involve all the uncertainties of values used in the calculation. Columns 6 (B^*) show magnetic-field values without taking into account excited state uncertainties. In columns 7 are written on which frequency differences between excited states the uncertainty of magnetic-field value depends on according to Figure 4.12. Magnetic-field values, which cancel the $|F_g = 2, m_g = 1\rangle \rightarrow |F_e = 2, m_e = 2\rangle$ transitions [see No. 8 for each table], depend only on γ, the frequency difference between $F_e = 3$ and $F_e = 2$ levels.

Table 4.11: Magnetic-field values canceling σ^+ transitions for ^{87}Rb D_2 line.

No.	F_g	F_e	m_g	B (G)	B^* (G)	ΔE_e
1	2	1	-2	1792.8(1.2)	1792.854752(13)	β, γ
2	1	0	-1	1595.84(93)	1595.846039(12)	α, β, γ
3	2	0	-1	1762.3(1.7)	1762.305097(13)	α, β, γ
4	2	1	-1	37.7187(20)	37.71876912(27)	α, β, γ
5	2	2	-1	157.6244(63)	157.6244550(11)	α, β, γ
6	2	1	0	35.0323(19)	35.03235682(25)	β, γ
7	2	2	0	183.1469(71)	183.1469403(13)	β, γ
8	2	2	1	211.1182(80)	211.1182479(15)	γ

Table 4.12: Magnetic-field values canceling ^{87}Rb 5 $^2S_{1/2} \rightarrow 6\ ^2P_{3/2}$ σ^+ transitions.

No.	F_g	F_e	m_g	B (G)	B^* (G)	ΔE_e
1	2	1	-2	606(4)	606.26243494(19)	β, γ
2	1	0	-1	528(8)	528.89107942(16)	α, β, γ
3	2	0	-1	581(4)	581.79032289(18)	α, β, γ
4	2	1	-1	12.1773(77)	12.1773749366(36)	α, β, γ

Continued on next page

Table 4.12 – *Continued from previous page*

No.	F_g	F_e	m_g	B (G)	B^* (G)	ΔE_e
5	2	2	-1	50.263(19)	50.263197219(15)	α, β, γ
6	2	1	0	11.2105(63)	11.2105200388(35)	β, γ
7	2	2	0	57.089(18)	57.089445775(18)	β, γ
8	2	2	1	64.164(18)	64.164811472(20)	γ

For transitions 8, we were able to exhibit the following analytical formula (among all these transitions it is the only one where Hamiltonian matrices are of maximum 2×2 dimension):

$$B = -\frac{4\zeta\gamma\eta}{\mu_B \left(\eta + 3(g_I - g_S)\gamma\right)\left(\eta - (g_I - g_S)\gamma\right)}, \tag{4.50}$$

where we denoted $\eta = 3(g_I - g_S)\gamma - (3g_I - 2g_L - g_S)\zeta$. While comparing with the formula (4.47) obtained in the case of $n\ ^2S_{1/2} \to k\ ^2P_{1/2}$ transitions, one can note a huge difference between them. Obviously, Hamiltonian matrix for the ground state remains the same while for the excited state the matrix becomes more complicated. One of the reasons is the reference of the excited state's zero-field energy. Different total electronic angular momentum quantum numbers describing the excited state for $m = -2$ value play a role which completely changes diagonal and non-diagonal elements of the matrix. Also unperturbed transfer coefficients $a(F_e, m_e; F_g, m_g; q)$ undergo a significant change as σ^+ transition needs to be considered. We see, that the study of $n\ ^2S_{1/2} \to k\ ^2P_{3/2}$ transitions remains an interesting problem. The formula (4.50) provides a B-value for the cancellation $B = 211.1182479(15)$ G for the D_2 line and $B = 64.164811472(20)$ G for the $5\ ^2S_{1/2} \to 6\ ^2P_{3/2}$ transition, showing the theory to be in perfect agreement with the numerical simulation.

Figure 4.15 shows the only three cases of ^{87}Rb $5\ ^2S_{1/2} \to 5\ ^2P_{3/2}$ and $5\ ^2S_{1/2} \to 6\ ^2P_{3/2}$ σ^- transitions which cancel for a certain value of magnetic-field.

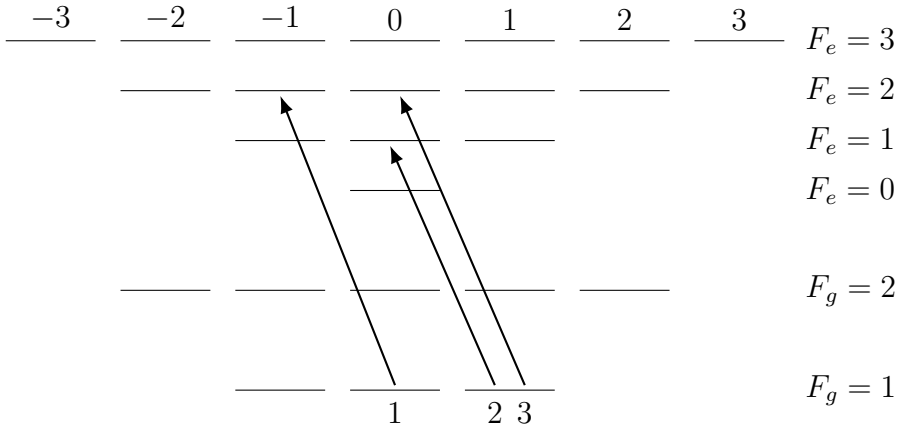

Figure 4.15: ^{87}Rb all $5\ ^2S_{1/2} \to 5\ ^2P_{3/2}$ and $5\ ^2S_{1/2} \to 6\ ^2P_{3/2}$ σ^- transitions scheme in a magnetic field which have a cancellation.

All ^{87}Rb $5\ ^2S_{1/2} \to 5\ ^2P_{3/2}$ and $5\ ^2S_{1/2} \to 6\ ^2P_{3/2}$ σ^- transition transfer coefficients, which

have a cancellation are depicted on Figure 4.16 and Figure 4.17 respectively. Curves on the figures are labeled in accordance with Figure 4.15.

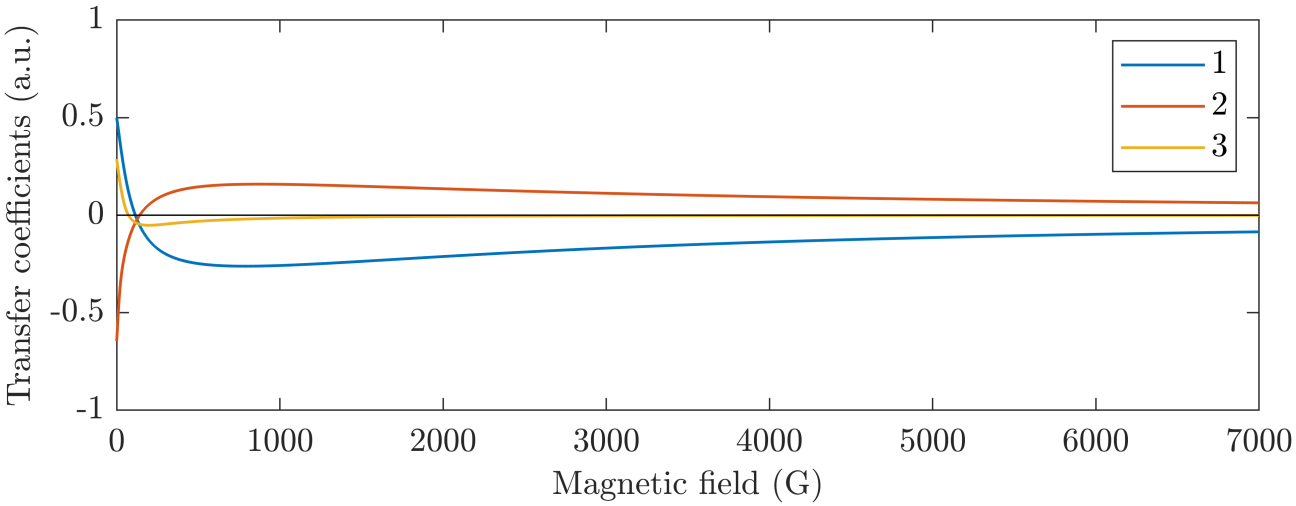

Figure 4.16: ^{87}Rb D_2 line σ^- transfer coefficients which have a cancellation.

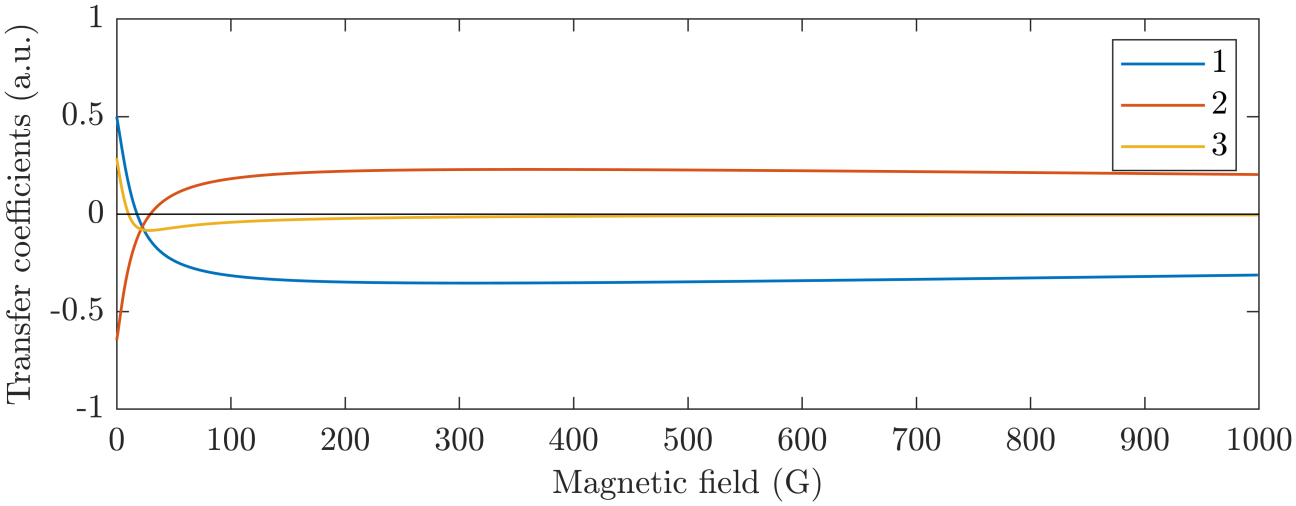

Figure 4.17: ^{87}Rb 5 $^2S_{1/2} \rightarrow$ 6 $^2P_{3/2}$ σ^- transfer coefficients which have a cancellation.

In Tables 4.13 and 4.14 ^{87}Rb all possible 5 $^2S_{1/2} \rightarrow$ 5 $^2P_{3/2}$ and 5 $^2S_{1/2} \rightarrow$ 6 $^2P_{3/2}$ σ^- transition cancellations are expressed.

Table 4.13: Magnetic-field values canceling σ^- transitions for ^{87}Rb D_2 line.

No.	F_g	F_e	m_g	B (G)	B^* (G)	ΔE_e
1	1	2	0	114.3072(50)	114.30723113(80)	β, γ
2	1	1	1	140.8256(71)	140.82560775(98)	α, β, γ
3	1	2	1	71.9264(47)	71.92641933(50)	α, β, γ

Table 4.14: Magnetic-field values canceling ^{87}Rb 5 $^2S_{1/2} \rightarrow 6\ ^2P_{3/2}$ σ^- transitions.

No.	F_g	F_e	m_g	B (G)	B^* (G)	ΔE_e
1	1	2	0	36.226(15)	36.226299830(11)	β, γ
2	1	1	1	44.053(32)	44.053383584(14)	α, β, γ
3	1	2	1	22.932(18)	22.9322893243(71)	α, β, γ

4.5.2 Analysis of the ^{85}Rb transitions

Hereafter we will examine ^{85}Rb 5 $^2S_{1/2} \rightarrow 5\ ^2P_{3/2}$ and 5 $^2S_{1/2} \rightarrow 6\ ^2P_{3/2}$ π, σ^+ and σ^- transfer coefficients within magnetic field. We will consider only transitions which have a cancellation. ^{85}Rb is a much more complicated system than ^{87}Rb, with large total atomic angular momentum (F). The structure scheme of ^{85}Rb 5 $^2S_{1/2} \rightarrow 5\ ^2P_{3/2}$ and 5 $^2S_{1/2} \rightarrow 6\ ^2P_{3/2}$ transitions is depicted on Figure. 4.18.

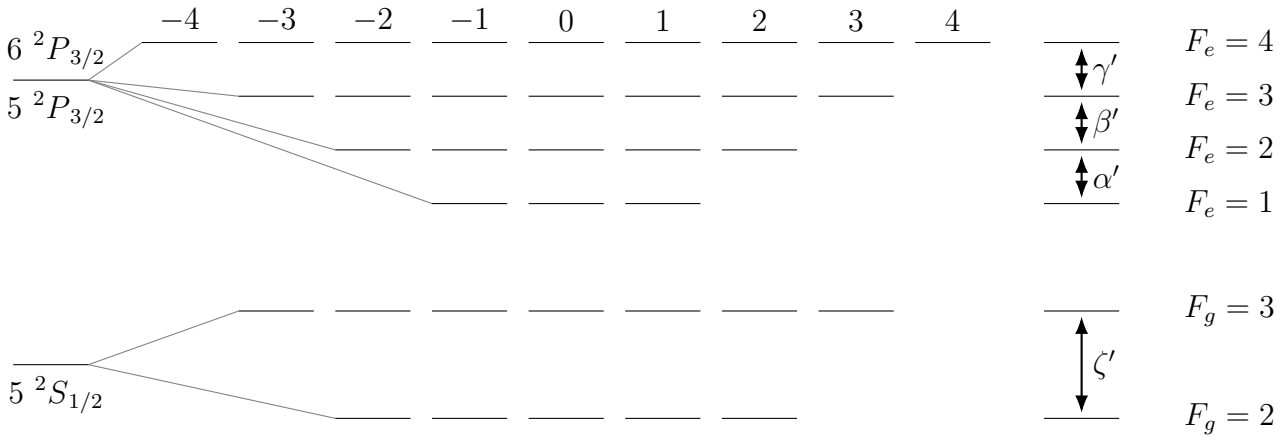

Figure 4.18: ^{85}Rb 5 $^2S_{1/2} \rightarrow 5\ ^2P_{3/2}$ and 5 $^2S_{1/2} \rightarrow 6\ ^2P_{3/2}$ transitions structure scheme in a magnetic field.

We will not show any scheme or transfer coefficients concerning π, σ^+ or σ^- transitions, because distinguishing one line from another would be very hard. We will only give tables where magnetic-field values which cancel certain transitions are indicated. As one can notice, for ^{85}Rb 5 $^2P_{3/2}$ and 6 $^2P_{3/2}$ excited states, the frequency differences are smaller than in the case of ^{87}Rb. For some cases we obtain analytical formulas similar to (4.47) and (4.50), where the value of B-field canceling transitions mostly depends on excited and ground state frequency differences (i.e. α', β', γ' and ζ'). Because of that the values of B-field which cancel certain transitions are generally smaller than the B-field values obtained in the case of ^{87}Rb.

Tables 4.15 and 4.16 include all magnetic-field values which cancel certain π transitions. Attentive readers may notice that some values of magnetic-field that cancel certain transitions are quite, comparatively, high (> 5686 G). And accordingly, the uncertainties of these values are big too. There are no such results for ^{87}Rb 5 $^2S_{1/2} \rightarrow 5\ ^2P_{3/2}$ and 5 $^2S_{1/2} \rightarrow 6\ ^2P_{3/2}$ transitions.

Table 4.15: B-field values canceling ^{85}Rb D_2 line π transitions.

F_g	F_e	m_g	B (G)	B^* (G)	ΔE_e
3	3	-2	31.977(23)	31.97774839(22)	β', γ'
2	2	-1	6.565(17)	6.565192522(44)	α', β', γ'
2	3	-1	48.463(58)	48.46368819(33)	α', β', γ'
2	4	-1	5686(29)	5686.364269(49)	α', β', γ'
3	2	-1	35.228(43)	35.22828802(24)	α', β', γ'
3	3	-1	12.811(11)	12.811030753(85)	α', β', γ'
2	3	0	47.491(54)	47.49141288(32)	α', β', γ'
2	4	0	6013(29)	6012.951766(52)	α', β', γ'
3	2	0	35.218(43)	35.21852774(24)	α', β', γ'
2	3	1	46.336(49)	46.33622671(31)	α', β', γ'
2	4	1	6345(29)	6345.448972(54)	α', β', γ'
3	2	1	34.945(40)	34.94502121(24)	α', β', γ'
2	3	2	45.099(42)	45.09972813(31)	β', γ'
2	4	2	6681(30)	6681.226747(57)	β', γ'
3	2	2	34.689(33)	34.68962622(24)	β', γ'

Table 4.16: Magnetic-field values canceling ^{85}Rb 5 $^2S_{1/2} \rightarrow$ 6 $^2P_{3/2}$ π transitions.

F_g	F_e	m_g	B (G)	B^* (G)	ΔE_e
3	3	-2	10.3069(82)	10.3069257317(79)	β', γ'
2	2	-1	2.1781(46)	2.1781258679(16)	α', β', γ'
2	3	-1	15.733(18)	15.733434029(12)	α', β', γ'
2	4	-1	6017(27)	6017.225484(16)	α', β', γ'
3	2	-1	11.353(14)	11.3538322950(87)	α', β', γ'
3	3	-1	4.1561(37)	4.1561596068(32)	α', β', γ'
2	3	0	15.296(17)	15.296627412(12)	α', β', γ'
2	4	0	6367(30)	6367.765683(17)	α', β', γ'
3	2	0	11.268(14)	11.2682145868(88)	α', β', γ'
2	3	1	14.769(16)	14.796304738(12)	α', β', γ'
2	4	1	6726(33)	6726.356956(18)	α', β', γ'
3	2	1	11.089(13)	11.08932124359(87)	α', β', γ'
2	3	2	14.269(15)	14.269650745(11)	β', γ'
2	4	2	7090(36)	7090.515803(19)	β', γ'
3	2	2	10.909(12)	10.9098105059(87)	β', γ'

Tables 4.17 and 4.18 include all magnetic-field values up to 10000 G which cancel certain ^{85}Rb 5 $^2S_{1/2} \rightarrow$ 5 $^2P_{3/2}$ and 5 $^2S_{1/2} \rightarrow$ 6 $^2P_{3/2}$ σ^+ transitions.

Table 4.17: B-field values canceling ^{85}Rb D_2 line σ^+ transitions.

F_g	F_e	m_g	B (G)	B^* (G)	ΔE_e
3	2	-3	278.3(1.4)	278.3151250(19)	β', γ'
2	1	-2	180.9(1.5)	180.9519212(13)	α', β', γ'
3	1	-2	254.1(1.3)	254.1070281(17)	α', β', γ'
3	2	-2	16.798(26)	16.79814373(12)	α', β', γ'
3	3	-2	62.626(59)	62.62663916(42)	α', β', γ'
2	1	-1	156.9(1.6)	156.9842182(11)	α', β', γ'
3	1	-1	231.6(1.3)	231.6749004(16)	α', β', γ'
3	2	-1	15.983(23)	15.98380527(11)	α', β', γ'
3	3	-1	72.575(61)	72.57573219(49)	α', β', γ'
2	1	0	137.2(1.6)	137.21112478(91)	α', β', γ'
3	1	0	211.1(1.3)	211.1105805(15)	α', β', γ'
3	2	0	15.337(20)	15.33734519(11)	α', β', γ'
3	3	0	83.643(63)	83.64378929(57)	α', β', γ'
3	2	1	14.808(18)	14.80813301(10)	β', γ'
3	3	1	96.085(66)	96.08519850(66)	β', γ'
3	3	2	110.162(71)	110.16208826(76)	γ'

Table 4.18: B-field values canceling ^{85}Rb $5\ ^2S_{1/2} \rightarrow 6\ ^2P_{3/2}$ σ^+ transitions.

F_g	F_e	m_g	B (G)	B^* (G)	ΔE_e
3	2	-3	93.67(48)	93.677445672(70)	β', γ'
2	1	-2	59.84(46)	59.841534398(47)	α', β', γ'
3	1	-2	84.76(46)	84.761785943(65)	α', β', γ'
3	2	-2	5.4915(84)	5.4915494036(42)	α', β', γ'
3	3	-2	20.189(19)	20.189735198(15)	α', β', γ'
2	1	-1	52.69(48)	52.687400374(41)	α', β', γ'
3	1	-1	76.78(44)	76.787359782(59)	α', β', γ'
3	2	-1	5.1947(76)	5.1947367200(40)	α', β', γ'
3	3	-1	23.036(20)	23.036018017(18)	α', β', γ'
2	1	0	46.62(48)	46.624063888(36)	α', β', γ'
3	1	0	69.65(42)	69.651160862(54)	α', β', γ'
3	2	0	4.9572(70)	4.9572750343(38)	α', β', γ'
3	3	0	26.064(20)	26.064610199(21)	α', β', γ'
3	2	1	4.7610(65)	4.7610264016(37)	β', γ'
3	3	1	29.313(20)	29.313263093(24)	β', γ'
3	3	2	32.813(20)	32.813410682(27)	γ'

In order to reduce uncertainties of the involved parameters, the first step is to try to measure more precisely the values of magnetic-field which cancel these transitions. The second step includes in itself the measurement of magnetic-field values for those transitions which uncertainties depends on only one frequency difference (e.g. last line of Tables 4.17 and 4.18).

Consequently, by measuring different magnetic-field values which cancel certain transitions, it is possible to decrease the uncertainties of excited state frequency differences. It is important to note, that the values written on last lines of the tables cancel $|F_g = 3, m = 2\rangle \rightarrow |F_e = 3, m = 3\rangle$ transition and its uncertainty depends only on excited state $F_e = 3$ and $F_e = 4$ frequency difference (γ') [see Figure 4.18].

Tables 4.19 and 4.20 include all the magnetic-field values that cancel certain ^{85}Rb 5 $^2S_{1/2} \rightarrow$ 5 $^2P_{3/2}$ and 5 $^2S_{1/2} \rightarrow$ 6 $^2P_{3/2}$ σ^- transitions.

Table 4.19: B-field values canceling ^{85}Rb D_2 line σ^- transitions.

F_g	F_e	m_g	B (G)	B^* (G)	ΔE_e
2	3	-1	46.630(40)	46.63046914(32)	β', γ'
2	4	-1	4718(20)	4718.168407(41)	β', γ'
2	2	0	50.440(68)	50.44005212(34)	α', β', γ'
2	3	0	32.361(41)	32.36112827(22)	α', β', γ'
			4354(19)	4354.588882(38)	
2	2	1	51.930(93)	51.93093445(35)	α', β', γ'
2	3	1	29.726(51)	29.72652541(20)	α', β', γ'
			4005(19)	4004.977769(35)	
2	2	2	52.27(12)	52.27464320(36)	α', β', γ'
2	3	2	27.764(58)	27.76483242(19)	α', β', γ'
			3669(21)	3669.632908(32)	

Table 4.20: B-field values canceling ^{85}Rb 5 $^2S_{1/2} \rightarrow$ 6 $^2P_{3/2}$ σ^- transitions.

F_g	F_e	m_g	B (G)	B^* (G)	ΔE_e
2	3	-1	14.939(14)	14.939707247(12)	β', γ'
2	4	-1	5028(24)	5028.533960(13)	β', γ'
2	2	0	16.100(22)	16.100382502(13)	α', β', γ'
2	3	0	10.383(14)	10.3833071342(80)	α', β', γ'
			4661(22)	4661.474736(12)	
2	2	1	16.511(27)	16.511161122(13)	α', β', γ'
2	3	1	9.459(16)	9.45921227700(74)	α', β', γ'
			4308(19)	4308.0783929(12)	
2	2	2	16.582(32)	16.582004270(14)	α', β', γ'
2	3	2	8.769(18)	8.7690392145(69)	α', β', γ'
			3968(20)	3968.442808(10)	

One can notice that in both tables rows 4, 6 and 8 have two magnetic-field values canceling one transition. Determination of an explicit formula giving these magnetic-field values, if possible, could help to understand why these transitions are canceled twice.

4.6 Experimental feasibility analysis

Calculations for the cancellation of transitions in a magnetic field in the framework of the proposed model were carried out based on physical constants and the values of the basic quantities characterizing the atomic system under consideration, available from the literature [see Tables 4.1 and 4.8]. In the case of a proper experimental implementation, an accurate measurement of the magnetic field corresponding to the canceling of the optical transition will make it possible to determine exact values of the physical parameters, in particular excited state frequency differences ε in the case of $n\,^2S_{1/2} \to k\,^2P_{1/2}$ transitions and α, β and γ in the case of $n\,^2S_{1/2} \to k\,^2P_{3/2}$ transitions, the only physical constants determined so far with least precision. Carefully elaborated experimental configuration and extremely high accuracy in measuring the applied magnetic field are required to achieve this goal, which makes the task ambitious. Let us briefly analyze the requirements to experimental setup and its characteristics needed to attain transition cancellation, which can be used, in particular, for accurate calibration of magnetometers and refinement of the values of physical constants involved in the processes under study.

First, in thermal atomic vapor, the hyperfine transitions, and especially, transitions between the magnetic sublevels of hyperfine states are Doppler-broadened and overlapped. To work with a chosen individual transition, it has to be frequency-separated from the neighboring ones. This can be done with the use of high-resolution spectroscopic techniques providing sub-Doppler or Doppler-free frequency resolution, in particular, monokinetic atomic beam [154,155] or nanocell [105, 110] spectroscopy. Moreover, the tuning range of a single-frequency cw laser should be sufficiently large to follow the frequency shift of the chosen transition in a B-field. These requirements are easy to fulfill with the use of non-expensive diode lasers and Rb vapor nanocells with $\approx \lambda/2$ thickness in SR configuration providing $\approx$ 40 MHz linewidth [109], or in the fluorescence configuration providing $\approx$ 60 MHz linewidth [93, 156]. These widths are sufficient for the complete separation of individual transitions, and hence the study of the cancellation, for magnetic fields above $\approx$ 100 G. Noteworthy, both of these techniques provide a linear response of the atomic medium [109, 156], unlike the widely used sub-Doppler technique of saturated absorption spectroscopy. The use of nanocells is advantageous also for a guaranteed uniformity of the applied magnetic field thanks to extremely small size of the interaction region [112, 157].

Another important point is detection sensitivity. The precision of transition cancellation is physically limited by a noise level. Here the figure of merit is a signal-to-noise ratio (SNR). The level of typical SR signal varies within $\approx$ 5 % from the incident light signal. In contrast, the fluorescence signal has a zero off-resonance background. Conventional signal acquisition and processing techniques allow reliable detection of signal with SNR up to 10000. For particular cases of SR and fluorescence measurements, the estimate for the magnitude of canceled transition is $\sim$ 0.1 % of the initial value.

Furthermore, the signal magnitude can be affected by the accuracy of setting and maintaining a given thickness of the nanocell in the interaction region. This problem is easily solved by controlling the radiation beam diameter and precise positioning of the beam with

micro-controlled translation stage.

The main limitation are expected to come from the precision of application and measurement of B-field values. We should clearly distinguish two aspects: i) the accuracy of magnitude and direction of the applied B-field needed to cancel the transition, and ii) the precision of measurement of this field. We believe the most appropriate solution combining magnetic field control with its measurement may be the use of optical compensation magnetometry [13, 158]. The essence of the method is as follows. The interaction region, i.e. the vapor nanocell, is mounted into a system of calibrated Helmholtz coils (three mutually perpendicular pairs). Coil currents are scanned according to a special algorithm controlled by the studied transition signal. Using the method of successive approximations, a magnetic-field value corresponding to the minimum of the atomic signal is achieved, and from the corresponding current values of coil currents a canceling field value is determined. With the use of this method, control and measurement of a B-field with ≈ 1 mG accuracy is experimentally feasible.

Last but not least, in the course of the measurements the laser radiation frequency should be stabilized on the transition under study. This can be done by implementing a feedback-based tunable locking of radiation frequency to an atomic resonance providing ~ 2 MHz accuracy [113], realized on an auxiliary setup with the second nanocell.

The above analysis shows that the expected realistic accuracy of the application and measurement of the B-field in the experiment is still far from the precision of the calculated values given in the tables of Sections 4.4 and 4.5. However, it should be noted that it is possible to decrease the uncertainties of excited state frequency differences by measuring the cancellation B-field values for different transitions, for which the uncertainties depend on one frequency difference (e.g. last line of Tables 4.17 and 4.18).

Another possibility is the indirect measurement of the B-field values canceling transitions, which in the case of $n\,^2S_{1/2} \to k\,^2P_{1/2}$ transitions is possible. As for small peaks the signal-to-noise ratio is smaller than for higher peaks, it is profitable to measure peaks with bigger intensity. Thus the option is to measure those transitions which are maximizing for a B-field value. If we can measure precisely the magnetic-field magnitude for which the transition intensity is maximum, it will mean that pair-transition cancellation value is found. Obviously, the graph of the derivative of the intensity with respect to the magnetic field should be calculated in the neighborhood of the maximum value, despite the fact that the change of transition intensity can be very smooth, as the change of sign of the slope of the derivative will give precisely the value for which it crosses the B-axis, thus will give the B-field value for which the pair-transitions reach their minimum.

Besides a more accurate determination of physical quantities, the obtained results can be used for practical applications, in particular, for magnetometry and optical information. Continuous detection of an atomic signal while moving the nanocell across highly non-uniform magnetic field will allow a high-contrast optical mapping of a B-field. On the other hand, modulation of the magnetic field around the transition cancellation point will allow to modulate the amplitude of the optical atomic signal that carries optical information.

As a final remark, let us note that not all the B-field values canceling transitions can be of

interest for particular practical tasks. There is yet another figure of merit that is the rate of variation of transition probability with the B-field around the cancellation value. The higher this rate, the more accurately one can determine the canceling B-field value.

4.7 Conclusion

Summarizing, we have developed a precise model to calculate intensities of all the optical transitions between magnetic sublevels of hyperfine levels, excited with π, σ^+ and σ^- polarized light, for $n\ ^2S_{1/2} \rightarrow k\ ^2P_{1/2,\,3/2}$ transitions of alkali-metal atoms. We determined a unique formula for $n\ ^2S_{1/2} \rightarrow k\ ^2P_{1/2}$ transitions, expressing magnetic-field values for which some π transition intensities become zero and the intensity of some others become maximum simultaneously. $n\ ^2S_{1/2} \rightarrow k\ ^2P_{1/2}$ transitions do not cancel for σ^+ and σ^- polarization. Our analytical and numerical calculations have revealed complete canceling of some individual transitions at precisely determined values of the B-field that can serve for very sensitive magnetometers calibration. Some standards should exist and these values are good standards for atomic systems: they do not depend on any external condition or parameter.

We have calculated all the transition-canceling B values using two different methods. In the first method, all the parameters are kept with their uncertainties. The obtained magnetic-field values are given in tables, and obviously the precision is strongly affected by the uncertainty of the excited state frequency differences. In the second method, the excited state frequency differences were used without their uncertainties, while other parameters were used with their uncertainties (Tables 4.2, 4.3, 4.7, 4.9, 4.10, 4.11, 4.12, 4.13 and 4.14 column 6, 4.4 and 4.6 column 7, and 4.15, 4.16, 4.17, 4.18, 4.19 and 4.20 column 5). These columns clearly indicate that the uncertainties on the B-field values arise mainly from the excited state frequency differences.

We believe the appropriate experimental realization will allow reducing the uncertainties of some physical parameters, in particular the values of frequency difference between the upper states that are currently determined with a least accuracy. In addition, we have outlined other applications, notably in optical magnetometry and optical information, where the obtained results can be used.

The results obtained in this chapter are published in references [33], [34] and [36].

Conclusion and Outlook

To conclude, the main results of this thesis, expressing the relevance of the subject, scientific novelty and practical importance, could be formulated in the following way.

In the second chapter we theoretically demonstrate the possibility of atomic population transfer in a M-type system interacting with four Gaussian pulses, using non-stationary numerical solutions of time-dependent quantum Liouville equation. It is shown that the transition frequency scanning technique allows us to completely transfer the population very efficiently, without precisely knowing the resonant frequency of the given transition. Then very simple implementation of reversible atomic Toffoli and Fredkin gates are demonstrated by using near-resonant pulsed laser fields of Gaussian shape. Due to the fact that these gates are universal, the obtained results could serve as a basis for logic circuits construction based on alkali-metal vapors. The choice of such a system is due to the fact that it allows us to make a three-bit devices and gates. On the other hand, M-type system could be implemented using the electronic terms or magnetic sublevels of the alkali atom.

In the third chapter we provide a simple experiment to record the fluorescence spectra of rubidium atomic vapor D_2 line in a transient regime. In addition, we developed a theoretical model, which describes all the processes in the atomic vapor cell, and the results of the numerical simulation are in very good agreement with the experimental results. The experiment and fitting with the theory allow us to determine important parameters, such as the relaxation rate of the ground energy levels to the equilibrium isotropic state. Except of it we are able to determine the diffusion coefficient of the buffered alkali atom vapor cell and the corresponding collisional cross section. Based on this and upcoming research we hope to be able to determine appropriate temporal conditions for efficient heralded control of atomic population in a multilevel system, by implementing a frequency-modulated cw laser as an effective source of controllable pulsed radiation.

In the fourth chapter we consider optical $n\ ^2S_{1/2} \rightarrow k\ ^2P_{1/2}$ transition cancellations between magnetic sublevels analytically. We obtained a unique formula expressing magnetic-field values canceling these transitions. In addition, we analyzed all stable and long-lived alkali-metal isotopes. For more complicated cases, i.e. $5\,^2S_{1/2} \rightarrow 5\,^2P_{3/2}$ and $5\,^2S_{1/2} \rightarrow 6\,^2P_{3/2}$ transitions of ^{85}Rb and ^{87}Rb isotopes, we obtained these values by numerical simulation. Analytical formula could be used to decrease uncertainty of the physical quantities involved in the calculations, such as energy difference between excited states, Bohr magneton, Landé factors. Vice versa, if these quantities will be known more precisely, the magnetic field values could be improved. Another point is that these values can serve as a good tool to calibrate precisely wide-range

magnetometers (from 5 G up to 7000 G). To provide the experiment, that is to be able to measure precisely magnetic field values canceling transitions we need to use high-resolution spectroscopic techniques providing sub-Doppler or Doppler-free frequency resolution, of course the perfectly adequate ingredient for carrying out the experiments is the nanocell.

Acknowledgements

I would like to express my deepest gratitude to my supervisors Prof. Claude Leroy and Dr. Emil Gazazyan for their scientific support, for productive discussions, for the motivation during complicated periods of my PhD study: without their support, this thesis would not have been possible.

I am particularly thankful to Profs. Aram Papoyan and Gayane Grigoryan for their numerous fruitful discussions, advice and assistance in the work. I would like also to thank all the co-workers and staff of the Laboratoire Interdisciplinaire Carnot de Bourgogne of University of Burgundy and Institute for Physical Research of National Academy of Sciences for their assistance and attitude.

I am grateful to my family for their support, encouragement, patience and understanding during the years of my PhD studies. In addition, my friends supported me a lot during these years, for which I am thankful to them.

The main financial support for this thesis came from the Graduate School EUR EIPHI of UBFC. I would like to acknowledge them for funding No. CO.17049.PAC.AN. I would like also to acknowledge financial supports from Armenian General Benevolent Union (AGBU, International Scholarship) and PHC OSMOSE 2020 (Project code: 44548QD). This research was sponsored in part by the NATO Science for Peace and Security Programme under grant G5794.

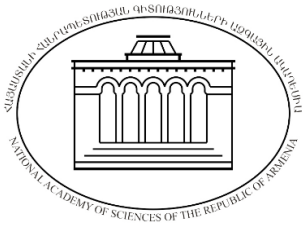

Bibliography

[1] D. A. Van Baak, "Resonant Faraday rotation as a probe of atomic dispersion," *Am. J. Phys.*, vol. 64, no. 6, pp. 724–735, 1996. [Online]. Available: https://doi.org/10.1119/1.18356

[2] R. Drampyan, A. D. Greentree, and A. V. Durrant, "Two field nonlinear Faraday rotation in rubidium vapor in a Doppler-free geometry," *Opt. Commun.*, vol. 276, no. 2, pp. 251 – 260, 2007. [Online]. Available: http://www.sciencedirect.com/science/article/pii/S0030401807004294

[3] M. Auzinsh, D. Budker, and S. M. Rochester, *Optically Polarized Atoms: Understanding Light-Atom Interactions*. Oxford University Press, 2010.

[4] J. Alnis, K. Blushs, M. Auzinsh, S. Kennedy, N. Shafer-Ray, and E. R. I. Abraham, "The Hanle effect and level crossing spectroscopy in Rb vapour under strong laser excitation," *J. Phys. B: At. Mol. Opt. Phys.*, vol. 36, no. 6, pp. 1161–1173, Feb 2003. [Online]. Available: https://doi.org/10.1088/0953-4075/36/6/307

[5] E. Breschi and A. Weis, "Ground-state Hanle effect based on atomic alignment," *Phys. Rev. A*, vol. 86, p. 053427, Nov 2012. [Online]. Available: https://link.aps.org/doi/10.1103/PhysRevA.86.053427

[6] R. H. Dicke, "The Effect of Collisions upon the Doppler Width of Spectral Lines," *Phys. Rev.*, vol. 89, pp. 472–473, Jan 1953. [Online]. Available: https://link.aps.org/doi/10.1103/PhysRev.89.472

[7] O. Firstenberg, M. Shuker, A. Ben-Kish, D. R. Fredkin, N. Davidson, and A. Ron, "Theory of Dicke narrowing in coherent population trapping," *Phys. Rev. A*, vol. 76, p. 013818, Jul 2007. [Online]. Available: https://link.aps.org/doi/10.1103/PhysRevA.76.013818

[8] S. Brandt, A. Nagel, R. Wynands, and D. Meschede, "Buffer-gas-induced linewidth reduction of coherent dark resonances to below 50 Hz," *Phys. Rev. A*, vol. 56, pp. R1063–R1066, Aug 1997. [Online]. Available: https://link.aps.org/doi/10.1103/PhysRevA.56.R1063

[9] E. E. Mikhailov, V. A. Sautenkov, Y. V. Rostovtsev, and G. R. Welch, "Absorption resonance and large negative delay in rubidium vapor with a buffer gas," *J.*

Opt. Soc. Am. B, vol. 21, no. 2, pp. 425–428, Feb 2004. [Online]. Available: http://josab.osa.org/abstract.cfm?URI=josab-21-2-425

[10] E. E. Mikhailov, I. Novikova, Y. V. Rostovtsev, and G. R. Welch, "Buffer-gas-induced absorption resonances in Rb vapor," *Phys. Rev. A*, vol. 70, p. 033806, Sep 2004. [Online]. Available: https://link.aps.org/doi/10.1103/PhysRevA.70.033806

[11] K. Dieckmann, R. J. C. Spreeuw, M. Weidemüller, and J. T. M. Walraven, "Two-dimensional magneto-optical trap as a source of slow atoms," *Phys. Rev. A*, vol. 58, pp. 3891–3895, Nov 1998. [Online]. Available: https://link.aps.org/doi/10.1103/PhysRevA.58.3891

[12] D. Budker, L. Hollberg, D. F. Kimball, J. Kitching, S. Pustelny, and V. V. Yashchuk, "Microwave transitions and nonlinear magneto-optical rotation in anti-relaxation-coated cells," *Phys. Rev. A*, vol. 71, p. 012903, Jan 2005. [Online]. Available: https://link.aps.org/doi/10.1103/PhysRevA.71.012903

[13] A. Papoyan, S. Shmavonyan, A. Khanbekyan, K. Khanbekyan, C. Marinelli, and E. Mariotti, "Magnetic-field-compensation optical vector magnetometer," *Appl. Opt.*, vol. 55, no. 4, pp. 892–895, Feb 2016. [Online]. Available: http://ao.osa.org/abstract.cfm?URI=ao-55-4-892

[14] S. Glasgow, P. Meystre, M. Wilkens, and E. M. Wright, "Theory of an atomic beam splitter based on velocity-tuned resonances," *Phys. Rev. A*, vol. 43, pp. 2455–2463, Mar 1991. [Online]. Available: https://link.aps.org/doi/10.1103/PhysRevA.43.2455

[15] A. Z. Muradyan, A. A. Poghosyan, and P. R. Berman, "Theory of a compound large-angle atom beam splitter," *Phys. Rev. A*, vol. 68, p. 033604, Sep 2003. [Online]. Available: https://link.aps.org/doi/10.1103/PhysRevA.68.033604

[16] K.-K. Park, T.-M. Zhao, J.-C. Lee, Y.-T. Chough, and Y.-H. Kim, "Coherent and dynamic beam splitting based on light storage in cold atoms," *Sci. Rep.*, vol. 6, p. 34279, Sep 2016. [Online]. Available: https://doi.org/10.1038/srep34279

[17] M. L. Ter-Mikhaelyan, "Simple atomic systems in resonant laser fields," *PHYS-USP*, vol. 40, pp. 1195–1238, 1997. [Online]. Available: https://doi.org/10.1070/pu1997v040n12abeh000318

[18] A. V. Bogachev, S. G. Garanin, A. M. Dudov, V. A. Eroshenko, S. M. Kulikov, G. T. Mikaelian, V. A. Panarin, V. O. Pautov, A. V. Rus, and S. A. Sukharev, "Diode-pumped caesium vapour laser with closed-cycle laser-active medium circulation," *Quantum Elec.*, vol. 42, no. 2, pp. 95–98, Feb 2012. [Online]. Available: https://doi.org/10.1070/qe2012v042n02abeh014734

[19] A. I. Parkhomenko and A. M. Shalagin, "Transversely diode-pumped alkali metal vapour laser," *Quantum Elec.*, vol. 45, no. 9, pp. 797–806, Sep 2015. [Online]. Available: https://doi.org/10.1070/qe2015v045n09abeh015802

[20] M. O. Scully and M. Fleischhauer, "High-sensitivity magnetometer based on index-enhanced media," *Phys. Rev. Lett.*, vol. 69, pp. 1360–1363, Aug 1992. [Online]. Available: https://link.aps.org/doi/10.1103/PhysRevLett.69.1360

[21] M. Fleischhauer and M. O. Scully, "Quantum sensitivity limits of an optical magnetometer based on atomic phase coherence," *Phys. Rev. A*, vol. 49, pp. 1973–1986, Mar 1994. [Online]. Available: https://link.aps.org/doi/10.1103/PhysRevA.49.1973

[22] D. Budker and M. Romalis, "Optical magnetometry," *Nat. Phys.*, vol. 3, no. 4, pp. 227–234, 2007. [Online]. Available: https://doi.org/10.1038/nphys566

[23] R. Mhaskar, S. Knappe, and J. Kitching, "A low-power, high-sensitivity micromachined optical magnetometer," *Appl. Phys. Lett.*, vol. 101, no. 24, p. 241105, 2012. [Online]. Available: https://doi.org/10.1063/1.4770361

[24] M. Hosseini, B. Sparkes, G. Campbell, P. Lam, and B. Buchler, "High efficiency coherent optical memory with warm rubidium vapour," *Nat. Commun.*, vol. 2, p. 174, Feb 2011. [Online]. Available: https://doi.org/10.1038/ncomms1175

[25] Y.-W. Cho, G. T. Campbell, J. L. Everett, J. Bernu, D. B. Higginbottom, M. T. Cao, J. Geng, N. P. Robins, P. K. Lam, and B. C. Buchler, "Highly efficient optical quantum memory with long coherence time in cold atoms," *Optica*, vol. 3, no. 1, pp. 100–107, Jan 2016. [Online]. Available: http://www.osapublishing.org/optica/abstract.cfm?URI=optica-3-1-100

[26] R. B. Li, L. Deng, and E. W. Hagley, "Fast, all-optical logic gates and transistor functionalities using a room-temperature atomic controlled Kerr gate," *Phys. Rev. A*, vol. 90, p. 063806, Dec 2014. [Online]. Available: https://link.aps.org/doi/10.1103/PhysRevA.90.063806

[27] R. J. Knize, "Optical NOR gate using cesium vapor," *Opt. Lett.*, vol. 17, no. 4, pp. 244–246, Feb 1992. [Online]. Available: http://ol.osa.org/abstract.cfm?URI=ol-17-4-244

[28] A. Sargsyan, A. Papoyan, I. G. Hughes, C. S. Adams, and D. Sarkisyan, "Selective reflection from an Rb layer with a thickness below $\lambda/12$ and applications," *Opt. Lett.*, vol. 42, no. 8, pp. 1476–1479, Apr 2017. [Online]. Available: http://ol.osa.org/abstract.cfm?URI=ol-42-8-1476

[29] A. Sargsyan, A. Amiryan, Y. Pashayan-Leroy, C. Leroy, A. Papoyan, and D. Sarkisyan, "Approach to quantitative spectroscopy of atomic vapor in optical nanocells," *Opt. Lett.*, vol. 44, no. 22, pp. 5533–5536, Nov 2019. [Online]. Available: http://ol.osa.org/abstract.cfm?URI=ol-44-22-5533

[30] T. Cutler, W. Hamlyn, J. Renger, K. Whittaker, D. Pizzey, I. Hughes, V. Sandoghdar, and C. Adams, "Nanostructured Alkali-Metal Vapor Cells," *Phys. Rev. Appl.*, vol. 14, p. 034054, Sep 2020. [Online]. Available: https://link.aps.org/doi/10.1103/PhysRevApplied.14.034054

[31] A. Y. Aleksanyan and E. A. Gazazyan, "Realization of the Programmable Logical Atomic Gate," *J. Contemp. Phys.*, vol. 53, pp. 205–211, Jul 2018. [Online]. Available: https://doi.org/10.3103/S1068337218030040

[32] A. Aleksanyan, S. Shmavonyan, E. Gazazyan, A. Khanbekyan, H. Azizbekyan, M. Movsisyan, and A. Papoyan, "Fluorescence of rubidium vapor in a transient interaction regime," *J. Opt. Soc. Am. B*, vol. 37, no. 1, pp. 203–210, Jan 2020. [Online]. Available: http://josab.osa.org/abstract.cfm?URI=josab-37-1-203

[33] A. Aleksanyan, R. Momier, E. Gazazyan, A. Papoyan, and C. Leroy, "Transition cancellations of ^{87}Rb and ^{85}Rb atoms in a magnetic field," *J. Opt. Soc. Am. B*, vol. 37, no. 11, pp. 3504–3514, Nov 2020. [Online]. Available: http://josab.osa.org/abstract.cfm?URI=josab-37-11-3504

[34] R. Momier, A. Aleksanyan, E. Gazazyan, A. Papoyan, and C. Leroy, "New standard magnetic field values determined by cancellations of ^{85}Rb and ^{87}Rb atomic vapors $5\,^2S_{1/2} \rightarrow 6\,^2P_{1/2,3/2}$ transitions," *J. Quant. Spectrosc. Radiat. Transfer*, vol. 257, p. 107371, Dec 2020. [Online]. Available: http://www.sciencedirect.com/science/article/pii/S0022407320306312

[35] A. Y. Aleksanyan, "Effective Full Population Transfer in M-System Using Scanning Technique," *J. Contemp. Phys.*, vol. 56, pp. 6–12, Apr 2021. [Online]. Available: https://doi.org/10.3103/S1068337221010035

[36] A. Aleksanyan, R. Momier, E. Gazazyan, A. Papoyan, and C. Leroy, "Cancellation of D_1 line transitions of alkali-metal atoms by magnetic-field values," *Phys. Rev. A*, vol. 105, p. 042810, Apr 2022. [Online]. Available: https://link.aps.org/doi/10.1103/PhysRevA.105.042810

[37] A. M. Turing, "On Computable Numbers, with an Application to the Entscheidungsproblem," *Proc. Lond. Math. Soc.*, vol. s2-42, no. 1, pp. 230–265, 1937. [Online]. Available: https://londmathsoc.onlinelibrary.wiley.com/doi/abs/10.1112/plms/s2-42.1.230

[38] A. Church, "An Unsolvable Problem of Elementary Number Theory," *Am. J. Math.*, vol. 58, no. 2, pp. 345–363, 1936. [Online]. Available: http://www.jstor.org/stable/2371045

[39] R. Landauer, "Irreversibility and Heat Generation in the Computing Process," *IBM J. Res. Dev.*, vol. 5, no. 3, pp. 183–191, 1961. [Online]. Available: http://dx.doi.org/10.1147/rd.53.0183

[40] T. Toffoli, *Reversible computing.* In: de Bakker J., van Leeuwen J. (eds) Automata, Languages and Programming. ICALP 1980. Lecture Notes in Computer Science, vol 85. Springer, Berlin, Heidelberg., 1980. [Online]. Available: https://doi.org/10.1007/3-540-10003-2_104

[41] K. A. Valiev, "Quantum computers and quantum computations," *Physics-Uspekhi*, vol. 48, no. 1, pp. 1–36, Jan 2005. [Online]. Available: https://doi.org/10.1070%2Fpu2005v048n01abeh002024

[42] Y. Wang, J. Li, S. Zhang, K. Su, Y. Zhou, K. Liao, S. Du, H. Yan, and S.-L. Zhu, "Efficient quantum memory for single-photon polarization qubits," *Nature Photonics*, vol. 13, no. 5, pp. 346–351, May 2019. [Online]. Available: https://doi.org/10.1038/s41566-019-0368-8

[43] J. Guo, X. Feng, P. Yang, Z. Yu, L. Q. Chen, C.-H. Yuan, and W. Zhang, "High-performance Raman quantum memory with optimal control in room temperature atoms," *Nat. Commun.*, vol. 10, no. 1, p. 148, Jan 2019. [Online]. Available: https://doi.org/10.1038/s41467-018-08118-5

[44] R. A. Akhmedzhanov, A. A. Bondartsev, L. A. Gushchin, and I. V. Zelensky, "Effective regime of electromagnetically induced transparency in a Pr^3+:LaF_3 crystal," *JETP Lett.*, vol. 94, no. 7, pp. 544–548, Dec 2019. [Online]. Available: https://doi.org/10.1134/S0021364011190027

[45] K. Bergmann, H. Theuer, and B. W. Shore, "Coherent population transfer among quantum states of atoms and molecules," *Rev. Mod. Phys.*, vol. 70, pp. 1003–1025, Jul 1998. [Online]. Available: https://link.aps.org/doi/10.1103/RevModPhys.70.1003

[46] P. Král, I. Thanopulos, and M. Shapiro, "Colloquium: Coherently controlled adiabatic passage," *Rev. Mod. Phys.*, vol. 79, pp. 53–77, Jan 2007. [Online]. Available: https://link.aps.org/doi/10.1103/RevModPhys.79.53

[47] I. V. Bargatin, B. A. Grishanin, and V. N. Zadkov, "Entangled quantum states of atomic systems," *Physics-Uspekhi*, vol. 44, no. 6, pp. 597–616, Jun 2001. [Online]. Available: https://doi.org/10.1070%2Fpu2001v044n06abeh000940

[48] H. J. Kimble, "The quantum internet," *Nature*, vol. 453, no. 7198, pp. 1023–1030, Jun 2008. [Online]. Available: https://doi.org/10.1038/nature07127

[49] L. Li, Y. O. Dudin, and A. Kuzmich, "Entanglement between light and an optical atomic excitation," *Nature*, vol. 498, no. 7455, pp. 466–469, Jun 2013. [Online]. Available: https://doi.org/10.1038/nature12227

[50] M. Fleischhauer, A. Imamoglu, and J. P. Marangos, "Electromagnetically induced transparency: Optics in coherent media," *Rev. Mod. Phys.*, vol. 77, pp. 633–673, Jul 2005. [Online]. Available: https://link.aps.org/doi/10.1103/RevModPhys.77.633

[51] M. D. Lukin, "*Colloquium*: Trapping and manipulating photon states in atomic ensembles," *Rev. Mod. Phys.*, vol. 75, pp. 457–472, Apr 2003. [Online]. Available: https://link.aps.org/doi/10.1103/RevModPhys.75.457

[52] I. Novikova, R. Walsworth, and Y. Xiao, "Electromagnetically induced transparency-based slow and stored light in warm atoms," *Laser Photonics Rev.*, vol. 6, no. 3, pp. 333–353, 2012. [Online]. Available: https://onlinelibrary.wiley.com/doi/abs/10.1002/lpor.201100021

[53] J. Klein, F. Beil, and T. Halfmann, "Robust Population Transfer by Stimulated Raman Adiabatic Passage in a Pr^{3+}:Y_2SiO_5 Crystal," *Phys. Rev. Lett.*, vol. 99, p. 113003, Sep 2007. [Online]. Available: https://link.aps.org/doi/10.1103/PhysRevLett.99.113003

[54] J. Preskill, *Lecture Notes for Physics 229: Quantum Information and Computation.* California Institute of Technology, 1998. [Online]. Available: http://www2.fiit.stuba.sk/~kvasnicka/QuantumComputing/PreskilTextbook_all.pdf

[55] E. A. Gazazyan, G. G. Grigoryan, V. O. Chaltykyan, and D. Schraft, "Implementation of all-optical Toffoli gate in Λ-systems," *J. Contemp. Phys.*, vol. 47, no. 5, pp. 216–221, Oct 2012. [Online]. Available: https://doi.org/10.3103/S1068337212050040

[56] G. Grigoryan, E. Gazazyan, V. Chaltykyan, and O. Tikhova, "Adiabatic control of atomic population and distortion-free propagation of short laser pulses in multilevel media," *Laser Phys.*, vol. 24, no. 3, p. 035301, Feb 2014. [Online]. Available: https://doi.org/10.1088%2F1054-660x%2F24%2F3%2F035301

[57] E. A. Gazazyan and G. G. Grigoryan, "Influence of multiphoton detunings from resonance on adiabatic processes in a five-level system," *J. Exp. Theor. Phys.*, vol. 124, no. 4, pp. 540–545, 2017. [Online]. Available: https://doi.org/10.1134/S1063776117030128

[58] E. A. Gazazyan and G. G. Grigoryan, "Influence of self-phase modulation on coherent effects in five-level system," *J. Contemp. Phys.*, vol. 51, no. 3, pp. 244–249, Jul 2016. [Online]. Available: https://doi.org/10.3103/S1068337216030063

[59] N. V. Vitanov, T. Halfmann, B. W. Shore, and K. Bergmann, "LASER-INDUCED POPULATION TRANSFER BY ADIABATIC PASSAGE TECHNIQUES," *Annu. Rev. Phys. Chem.*, vol. 52, no. 1, pp. 763–809, 2001. [Online]. Available: https://doi.org/10.1146/annurev.physchem.52.1.763

[60] B. W. Shore, "Picturing stimulated Raman adiabatic passage: a STIRAP tutorial," *Adv. Opt. Photon.*, vol. 9, no. 3, pp. 563–719, Sep 2017. [Online]. Available: http://aop.osa.org/abstract.cfm?URI=aop-9-3-563

[61] G. Grigoryan, V. Chaltykyan, E. Gazazyan, and O. Tikhova, *All-optical four-bit Toffoli gate with possible implementation in solids.* Proc. SPIE 8772, Nonlinear Optics and Applications VII, 87721N, 2013. [Online]. Available: https://doi.org/10.1117/12.2017148

[62] K. Blum, *Density Matrix Theory and Applications*. Berlin: Springer, 2012. [Online]. Available: https://www.springer.com/gp/book/9783642205606

[63] H.-P. Breuer and F. Petruccione, *The Theory of Open Quantum Systems*. Oxford University Press, 2002. [Online]. Available: https://global.oup.com/academic/product/the-theory-of-open-quantum-systems-9780198520634

[64] D. Manzano, "A short introduction to the Lindblad master equation," *AIP Adv.*, vol. 10, no. 2, p. 025106, 2020. [Online]. Available: https://doi.org/10.1063/1.5115323

[65] M. Reed and B. Simon, *Methods of Modern Mathematical Physics. I: Functional Analysis*. Academic Press, 1972. [Online]. Available: https://www.sciencedirect.com/book/9780125850018/methods-of-modern-mathematical-physics

[66] M. Reed and B. Simon, *Methods of Modern Mathematical Physics. II: Fourier Analysis, Self-Adjointness*. Academic Press, 1975. [Online]. Available: https://www.elsevier.com/books/ii-fourier-analysis-self-adjointness/reed/978-0-08-092537-0

[67] A. A. Markov and N. M. Nagorny, *The Theory of Algorithms*. Springer Netherlands, 1988. [Online]. Available: https://www.springer.com/gp/book/9789027727732

[68] C. Cohen-Tannoudji, J. Dupont-Roc, and G. Grynberg, *Atom-Photon Interactions: Basic Processes and Applications*. Wiley-VCH, 1998. [Online]. Available: https://www.wiley.com/en-us/Atom+Photon+Interactions%3A+Basic+Processes+and+Applications-p-9780471293361

[69] C. Aslangul, *Mécanique quantique 2 : Développements et applications à basse énergie*. De Boeck Supérieur, 2008. [Online]. Available: https://www.deboecksuperieur.com/ouvrage/9782807315594-mecanique-quantique-2

[70] E. Klinger, "Selective reflection spectroscopy of alkali vapors confined in nanocells and emerging sensing applications," *Thèse, Université Bourgogne Franche-Comté; Institute for Physical Research (Ashtarak)*, Sep 2019. [Online]. Available: https://tel.archives-ouvertes.fr/tel-02317761

[71] A. Rangelov, N. Vitanov, and B. Shore, "Rapid adiabatic passage without level crossing," *Opt. Commun.*, vol. 283, no. 7, pp. 1346–1350, 2010. [Online]. Available: https://www.sciencedirect.com/science/article/pii/S0030401809012619

[72] V. Malinovsky and J. Krause, "General theory of population transfer by adiabatic rapid passage with intense, chirped laser pulses," *Eur. Phys. J. D*, vol. 14, no. 2, pp. 147–155, 2001. [Online]. Available: https://doi.org/10.1007/s100530170212

[73] G. Grigoryan, "Self-consistent theory of selective reflection," *Opt. Mem. Neural Netw.*, vol. 18, no. 1, pp. 34–39, Mar 2009. [Online]. Available: https://doi.org/10.3103/S1060992X0901007X

[74] D. Steck, "Cesium D line data," Jan 2019. [Online]. Available: https://steck.us/alkalidata/

[75] E. B. Alexandrov, M. Auzinsh, D. Budker, D. F. Kimball, S. M. Rochester, and V. V. Yashchuk, "Dynamic effects in nonlinear magneto-optics of atoms and molecules: review," *J. Opt. Soc. Am. B*, vol. 22, no. 1, pp. 7–20, Jan 2005. [Online]. Available: http://josab.osa.org/abstract.cfm?URI=josab-22-1-7

[76] D. E. Thornton, G. T. Phillips, and G. P. Perram, "Velocity changing collisions in the laser saturation spectra of ^{87}Rb D_2 F"= 2," *Opt. Commun.*, vol. 284, no. 12, pp. 2890 – 2894, 2011. [Online]. Available: http://www.sciencedirect.com/science/article/pii/S0030401811002240

[77] F. E. Becerra, R. T. Willis, S. L. Rolston, H. J. Carmichael, and L. A. Orozco, "Nondegenerate four-wave mixing in rubidium vapor: Transient regime," *Phys. Rev. A*, vol. 82, p. 043833, Oct 2010. [Online]. Available: https://link.aps.org/doi/10.1103/PhysRevA.82.043833

[78] S. A. Khripunov, D. A. Radnatarov, S. M. Kobtsev, V. I. Yudin, A. V. Taichenachev, M. Y. Basalaev, M. V. Balabas, V. A. Andryushkov, and I. D. Popkov, "Transient processes under dynamic excitation of a coherent population trapping resonance," *Quantum. Elec.*, vol. 46, no. 7, pp. 668–671, Jul 2016. [Online]. Available: https://doi.org/10.1070%2Fqel15992

[79] V. I. Yudin, A. V. Taichenachev, M. Y. Basalaev, and D. V. Kovalenko, "Dynamic regime of coherent population trapping and optimization of frequency modulation parameters in atomic clocks," *Opt. Express*, vol. 25, no. 3, pp. 2742–2751, Feb 2017. [Online]. Available: http://www.opticsexpress.org/abstract.cfm?URI=oe-25-3-2742

[80] H.-R. Noh, "Analytical Solutions of Temporal Evolution of Populations in Optically-Pumped Atoms with Circularly Polarized Light," *Symmetry*, vol. 8, p. 17, Mar 2016. [Online]. Available: https://www.mdpi.com/2073-8994/8/3/17

[81] Z. D. Grujić, M. Mijailović, D. Arsenović, A. Kovačević, M. Nikolić, and B. M. Jelenković, "Dark Raman resonances due to Ramsey interference in vacuum vapor cells," *Phys. Rev. A*, vol. 78, p. 063816, Dec 2008. [Online]. Available: https://link.aps.org/doi/10.1103/PhysRevA.78.063816

[82] D. Steck, "Rubidium 85 D line data," Jan 2019. [Online]. Available: https://steck.us/alkalidata/

[83] D. Steck, "Rubidium 87 D line data," Jan 2019. [Online]. Available: https://steck.us/alkalidata/

[84] W. Happer, "Optical Pumping," *Rev. Mod. Phys.*, vol. 44, pp. 169–249, Apr 1972. [Online]. Available: https://link.aps.org/doi/10.1103/RevModPhys.44.169

[85] H. M. Gibbs and R. J. Hull, "Spin-Exchange Cross Sections for Rb^{87}-Rb^{87} and Rb^{87}-Cs^{133} Collisions," *Phys. Rev.*, vol. 153, pp. 132–151, Jan 1967. [Online]. Available: https://link.aps.org/doi/10.1103/PhysRev.153.132

[86] M. Gharavipour, C. Affolderbach, F. Gruet, I. S. Radojičić, A. J. Krmpot, B. M. Jelenković, and G. Mileti, "Optically-detected spin-echo method for relaxation times measurements in a Rb atomic vapor," *New J. Phys.*, vol. 19, no. 6, p. 063027, Jun 2017. [Online]. Available: https://doi.org/10.1088%2F1367-2630%2Faa73c2

[87] W. Franzen, "Spin Relaxation of Optically Aligned Rubidium Vapor," *Phys. Rev.*, vol. 115, pp. 850–856, Aug 1959. [Online]. Available: https://link.aps.org/doi/10.1103/PhysRev.115.850

[88] D. J. Croucher and J. L. Clark, "Total collision cross sections and van der Waals constants for alkali atom interactions with atoms and non-reactive diatomic molecules at thermal energies," *J. Phys. B: At. Mol. Phys.*, vol. 2, no. 5, pp. 603–623, May 1969. [Online]. Available: https://doi.org/10.1088%2F0022-3700%2F2%2F5%2F313

[89] A. Corney, *Atomic and Laser Spectroscopy*. Oxford University, 2006. [Online]. Available: https://global.oup.com/academic/product/atomic-and-laser-spectroscopy-9780199211456

[90] M. A. Rosenberry, J. P. Reyes, D. Tupa, and T. J. Gay, "Radiation trapping in rubidium optical pumping at low buffer-gas pressures," *Phys. Rev. A*, vol. 75, p. 023401, Feb 2007. [Online]. Available: https://link.aps.org/doi/10.1103/PhysRevA.75.023401

[91] F. Bowman, *Introduction to Bessel functions*. Dover, New York, 1958. [Online]. Available: http://cds.cern.ch/record/107935

[92] J. Matúška, "An efficient and accurate method to calculate diffusion coefficient of structured particles. A first case study of Pb diffusion in rare gases," *Acta Chim. Slov.*, vol. 9, no. 2, pp. 158–162, Oct 2016. [Online]. Available: https://content.sciendo.com/view/journals/acs/9/2/article-p158.xml

[93] G. Hakhumyan, A. Sargsyan, C. Leroy, Y. Pashayan-Leroy, A. Papoyan, and D. Sarkisyan, "Essential features of optical processes in neon-buffered submicron-thin Rb vapor cell," *Opt. Express*, vol. 18, no. 14, pp. 14 577–14 585, Jul 2010. [Online]. Available: http://www.opticsexpress.org/abstract.cfm?URI=oe-18-14-14577

[94] A. A. Sargsyan, A. Y. Aleksanyan, S. A. Petrosyan, E. A. Gazazyan, A. V. Papoyan, and H. V. Astsatryan, "Prediction of Atomic Ground State Relaxation Rate from Fluorescence Spectra Using Machine Learning," *J. Contemp. Phys.*, vol. 56, no. 4, pp. 285–290, Oct 2021. [Online]. Available: https://doi.org/10.3103/S1068337221040137

[95] C. J. Pethick and H. Smith, *Bose–Einstein Condensation in Dilute Gases*, 2nd ed. Cambridge University

Press, 2008. [Online]. Available: https://www.cambridge.org/core/books/boseeinstein-condensation-in-dilute-gases/CC439EAD70D78E47E9AF536DA7B203EC

[96] R. Legaie, C. J. Picken, and J. D. Pritchard, "Sub-kilohertz excitation lasers for quantum information processing with Rydberg atoms," *J. Opt. Soc. Am. B*, vol. 35, no. 4, pp. 892–898, Apr 2018. [Online]. Available: http://josab.osa.org/abstract.cfm?URI=josab-35-4-892

[97] S. V. Pappu, "Information storage using alkali halide crystals," *Contemp. Phys.*, vol. 26, no. 5, pp. 479–497, 1985. [Online]. Available: https://doi.org/10.1080/00107518508210985

[98] G. A. Muradyan and A. Z. Muradyan, "Theory of adiabatic variation of critical temperature of the bose-einstein condensation of an ideal gas in optical lattice," *J. Contemp. Phys.*, vol. 42, no. 3, pp. 94–100, Mar 2007. [Online]. Available: https://doi.org/10.3103/S1068337207030034

[99] G. A. Muradyan and A. Z. Muradyan, "Quasiclassical approximation for the resonant kapitza–dirac scattering," *J. Contemp. Phys.*, vol. 52, no. 3, pp. 195–200, Jul 2017. [Online]. Available: https://doi.org/10.3103/S1068337217030021

[100] N. Wilson, P. Light, A. Luiten, and C. Perrella, "Ultrastable Optical Magnetometry," *Phys. Rev. Appl.*, vol. 11, p. 044034, Apr 2019. [Online]. Available: https://link.aps.org/doi/10.1103/PhysRevApplied.11.044034

[101] T. J. V. Francis, R. R. Suna, P. K. Madhu, N. K. Viswanathan, and G. Rajalakshmi, "Ultra-sensitive single-beam atom-optical magnetometer using weak measurement method," *AIP Adv.*, vol. 9, no. 6, p. 065113, 2019. [Online]. Available: https://doi.org/10.1063/1.5090581

[102] C. So, "Zeeman-tunable Modulation Transfer Spectroscopy," *Masters thesis, Durham University*, 2020. [Online]. Available: http://etheses.dur.ac.uk/13481/

[103] L. Weller, K. S. Kleinbach, M. A. Zentile, S. Knappe, C. S. Adams, and I. G. Hughes, "Absolute absorption and dispersion of a rubidium vapour in the hyperfine Paschen–Back regime," *J. Phys. B: At. Mol. Opt. Phys.*, vol. 45, no. 21, p. 215005, Oct 2012. [Online]. Available: https://doi.org/10.1088%2F0953-4075%2F45%2F21%2F215005

[104] P. Tremblay, A. Michaud, M. Levesque, S. Thériault, M. Breton, J. Beaubien, and N. Cyr, "Absorption profiles of alkali-metal D lines in the presence of a static magnetic field," *Phys. Rev. A*, vol. 42, pp. 2766–2773, Sep 1990. [Online]. Available: https://link.aps.org/doi/10.1103/PhysRevA.42.2766

[105] N. Papageorgiou, A. Weis, V. A. Sautenkov, D. Bloch, and M. Ducloy, "High-resolution selective reflection spectroscopy in intermediate magnetic fields," *Appl. Phys. B*, vol. 59, no. 2, pp. 123–126, Aug 1994. [Online]. Available: https://doi.org/10.1007/BF01081162

[106] A. Sargsyan, G. Hakhumyan, A. Papoyan, D. Sarkisyan, A. Atvars, and M. Auzinsh, "A novel approach to quantitative spectroscopy of atoms in a magnetic field and applications based on an atomic vapor cell with $L = \lambda$," *Appl. Phys. Lett.*, vol. 93, no. 2, p. 021119, 2008. [Online]. Available: https://doi.org/10.1063/1.2960346

[107] A. Sargsyan, G. Hakhumyan, C. Leroy, Y. Pashayan-Leroy, A. Papoyan, D. Sarkisyan, and M. Auzinsh, "Hyperfine Paschen–Back regime in alkali metal atoms: consistency of two theoretical considerations and experiment," *J. Opt. Soc. Am. B*, vol. 31, no. 5, pp. 1046–1053, May 2014. [Online]. Available: http://josab.osa.org/abstract.cfm?URI=josab-31-5-1046

[108] A. Sargsyan, E. Klinger, A. Tonoyan, C. Leroy, and D. Sarkisyan, "Hyperfine Paschen–Back regime of potassium D_2 line observed by Doppler-free spectroscopy," *J. Phys. B: At. Mol. Opt. Phys.*, vol. 51, no. 14, p. 145001, Jun 2018. [Online]. Available: https://doi.org/10.1088%2F1361-6455%2Faac735

[109] A. Sargsyan, E. Klinger, Y. Pashayan-Leroy, C. Leroy, A. Papoyan, and D. Sarkisyan, "Selective reflection from Rb vapor in half- and quarter-wave cells: Features and possible applications," *JETP Lett.*, vol. 104, no. 4, pp. 224–230, Aug 2016. [Online]. Available: https://doi.org/10.1134/S002136401616013X

[110] G. Hakhumyan, C. Leroy, R. Mirzoyan, Y. Pashayan-Leroy, and D. Sarkisyan, "Study of "forbidden" atomic transitions on D_2 line using Rb nano-cell placed in external magnetic field," *Eur. Phys. J. D*, vol. 66, no. 5, p. 119, May 2012. [Online]. Available: https://doi.org/10.1140/epjd/e2012-20687-2

[111] K. A. Khanbekyan, E. Mariotti, A. A. Khanbekyan, L. Moi, and A. M. Khanbekyan, "Sub-doppler spectroscopy of sodium vapor in an ultrathin cell," *Opt. Spectrosc.*, vol. 120, no. 5, pp. 701–705, May 2016. [Online]. Available: https://doi.org/10.1134/S0030400X16050143

[112] A. Sargsyan, E. Klinger, G. Hakhumyan, A. Tonoyan, A. Papoyan, C. Leroy, and D. Sarkisyan, "Decoupling of hyperfine structure of Cs D_1 line in strong magnetic field studied by selective reflection from a nanocell," *J. Opt. Soc. Am. B*, vol. 34, no. 4, pp. 776–784, Apr 2017. [Online]. Available: http://josab.osa.org/abstract.cfm?URI=josab-34-4-776

[113] A. V. Papoyan, G. G. Grigoryan, S. V. Shmavonyan, D. Sarkisyan, J. Guéna, M. Lintz, and M. A. Bouchiat, "New feature in selective reflection with a highly parallel window: phase-tunable homodyne detection of the radiated atomic field," *Eur. Phys. J. D*, vol. 30, no. 2, pp. 265–273, Aug 2004. [Online]. Available: https://doi.org/10.1140/epjd/e2004-00088-0

[114] E. Klinger, A. Sargsyan, A. Tonoyan, G. Hakhumyan, A. Papoyan, C. Leroy, and D. Sarkisyan, "Magnetic field-induced modification of selection rules for Rb D_2 line

monitored by selective reflection from a vapor nanocell," *Eur. Phys. J. D*, vol. 71, no. 8, p. 216, Aug 2017. [Online]. Available: https://doi.org/10.1140/epjd/e2017-80291-6

[115] E. Klinger, H. Azizbekyan, A. Sargsyan, C. Leroy, D. Sarkisyan, and A. Papoyan, "Proof of the feasibility of a nanocell-based wide-range optical magnetometer," *Appl. Opt.*, vol. 59, no. 8, pp. 2231–2237, Mar 2020. [Online]. Available: http://ao.osa.org/abstract.cfm?URI=ao-59-8-2231

[116] G. Dutier, S. Saltiel, D. Bloch, and M. Ducloy, "Revisiting optical spectroscopy in a thin vapor cell: mixing of reflection and transmission as a Fabry–Perot microcavity effect," *J. Opt. Soc. Am. B*, vol. 20, no. 5, pp. 793–800, May 2003. [Online]. Available: http://josab.osa.org/abstract.cfm?URI=josab-20-5-793

[117] L. Windholz and M. Musso, "Zeeman- and Paschen-Back-effect of the hyperfine structure of the sodium D_2-line," *Z. Phys. D: At. Mol. Cl.*, vol. 8, pp. 239–249, Sep 1988. [Online]. Available: https://doi.org/10.1007/BF01436947

[118] M. V. Balabas, D. Budker, J. Kitching, P. D. D. Schwindt, and J. E. Stalnaker, "Magnetometry with millimeter-scale antirelaxation-coated alkali-metal vapor cells," *J. Opt. Soc. Am. B*, vol. 23, no. 6, pp. 1001–1006, Jun 2006. [Online]. Available: http://josab.osa.org/abstract.cfm?URI=josab-23-6-1001

[119] E. P. Corsini, T. Karaulanov, M. Balabas, and D. Budker, "Hyperfine frequency shift and Zeeman relaxation in alkali-metal-vapor cells with antirelaxation alkene coating," *Phys. Rev. A*, vol. 87, p. 022901, Feb 2013. [Online]. Available: https://link.aps.org/doi/10.1103/PhysRevA.87.022901

[120] M. Abe, R. Itoyama, Y. Komiyama, T. Ito, T. Mashimo, and S. Tojo, "Quantitative investigation of the Zeeman and Paschen-Back effects of the hyperfine structure during the rubidium $5\,^2S_{1/2} \rightarrow 5\,^2D_{5/2}$ two-photon transition," *Phys. Rev. A*, vol. 99, p. 053420, May 2019. [Online]. Available: https://link.aps.org/doi/10.1103/PhysRevA.99.053420

[121] D. J. Reed, N. Šibalić, D. J. Whiting, J. M. Kondo, C. S. Adams, and K. J. Weatherill, "Low-drift Zeeman shifted atomic frequency reference," *OSA Contin.*, vol. 1, no. 1, pp. 4–12, Sep 2018. [Online]. Available: http://www.osapublishing.org/osac/abstract.cfm?URI=osac-1-1-4

[122] A. Sargsyan, A. Tonoyan, G. Hakhumyan, and D. Sarkisyan, "Magnetically Induced Anomalous Dichroism of Atomic Transitions of the Cesium D_2 Line," *JETP Lett.*, vol. 106, no. 11, pp. 700–705, Dec 2017. [Online]. Available: https://doi.org/10.1134/S0021364017230126

[123] A. Tonoyan, A. Sargsyan, E. Klinger, G. Hakhumyan, C. Leroy, M. Auzinsh, A. Papoyan, and D. Sarkisyan, "Circular dichroism of magnetically induced transitions for D_2 lines of alkali atoms," *EPL*, vol. 121, no. 5, p. 53001, 2018. [Online]. Available: https://doi.org/10.1209/0295-5075/121/53001

[124] M. Weissbluth, *Atoms and Molecules.* Academic Press, 1978. [Online]. Available: https://www.elsevier.com/books/atoms-and-molecules/weissbluth/978-0-12-744450-5

[125] C. Cohen-Tannoudji, B. Diu, and F. Laloë, *Quantum Mechanics I.* Wiley-VCH, 1977. [Online]. Available: https://bit.ly/3nrz62G

[126] L. Labzowsky, I. Goidenko, and P. Pyykkö, "Estimates of the bound-state QED contributions to the g-factor of valence ns electrons in alkali metal atoms," *Phys. Lett. A*, vol. 258, no. 1, pp. 31 – 37, 1999. [Online]. Available: http://www.sciencedirect.com/science/article/pii/S0375960199003357

[127] E. Eriksen, "Foldy-Wouthuysen Transformation. Exact Solution with Generalization to the Two-Particle Problem," *Phys. Rev.*, vol. 111, pp. 1011–1016, Aug 1958. [Online]. Available: https://link.aps.org/doi/10.1103/PhysRev.111.1011

[128] E. Aleksandrov, M. Chaika, and G. Khvostenko, *Interference of Atomic States.* Springer-Verlag, New York, 1993. [Online]. Available: https://www.springer.com/gp/book/9783642844447

[129] E. Biémont, *Spectroscopie atomique. Instrumentation et structures atomiques.* Materials Science, 2006. [Online]. Available: https://bit.ly/3pZxzTa

[130] D. A. Varshalovich, A. N. Moskalev, and V. K. Khersonskii, *Quantum Theory of Angular Momentum.* World Scientific, 1988. [Online]. Available: https://www.worldscientific.com/doi/abs/10.1142/0270

[131] M. Rotenberg, R. Bivins, N. Metropolis, and J. Wooten Jr, *The* 3-J *and* 6-J *Symbols.* Technology Press, M.I.T., Cambridge, 1959. [Online]. Available: https://mitpress.mit.edu/books/3-j-and-6-j-symbols

[132] H. A. Bethe and E. E. Salpeter, *Quantum Mechanics of One- and Two-Electron Atoms.* Springer, Berlin, Heidelberg, 1957. [Online]. Available: https://link.springer.com/book/10.1007/978-3-662-12869-5

[133] E. Arimondo, M. Inguscio, and P. Violino, "Experimental determinations of the hyperfine structure in the alkali atoms," *Rev. Mod. Phys.*, vol. 49, pp. 31–75, Jan 1977. [Online]. Available: https://link.aps.org/doi/10.1103/RevModPhys.49.31

[134] E. de Clercq, M. de Labachellerie, G. Avila, P. Cerez, and T. M., "Laser diode optically pumped caesium beam," *J. Phys. France*, vol. 45, pp. 239–247, Feb 1984. [Online]. Available: https://doi.org/10.1051/jphys:01984004502023900

[135] K. Fujii, "A Modern Introduction to Cardano and Ferrari Formulas in the Algebraic Equations," *arXiv: Quantum Physics*, 2003. [Online]. Available: https://arxiv.org/abs/quant-ph/0311102v2

[136] A. Sargsyan, G. Hakhumyan, A. Papoyan, and D. Sarkisyan, "Alkali Metal Atoms in Strong Magnetic Fields: "Guiding" Atomic Transitions Foretell the Characteristics of All Transitions of the D_1 Line," *JETP Lett.*, vol. 101, pp. 303–307, 2015. [Online]. Available: https://doi.org/10.1134/S0021364015050148

[137] D. Steck, "Sodium D line data," Nov 2019. [Online]. Available: https://steck.us/alkalidata/

[138] D. Das and V. Natarajan, "High-precision measurement of hyperfine structure in the D lines of alkali atoms," *J. Phys. B: At. Mol. Opt. Phys.*, vol. 41, no. 3, p. 035001, Jan 2008. [Online]. Available: https://doi.org/10.1088%2F0953-4075%2F41%2F3%2F035001

[139] W. A. van Wijngaarden and J. Li, "Measurement of hyperfine structure of sodium $^3P_{1/2,3/2}$ states using optical spectroscopy," *Z. Phys. D: At. Mol. Cl.*, vol. 32, pp. 67–71, Mar 1994. [Online]. Available: https://doi.org/10.1007/BF01425925

[140] S. Falke, E. Tiemann, C. Lisdat, H. Schnatz, and G. Grosche, "Transition frequencies of the D lines of ^{39}K, ^{40}K, and ^{41}K measured with a femtosecond laser frequency comb," *Phys. Rev. A*, vol. 74, p. 032503, Sep 2006. [Online]. Available: https://link.aps.org/doi/10.1103/PhysRevA.74.032503

[141] T. Tiecke, "Properties of Potassium," https://tobiastiecke.nl/, Jun 2019.

[142] D. Budker, D. F. Kimball, S. M. Rochester, V. V. Yashchuk, and M. Zolotorev, "Sensitive magnetometry based on nonlinear magneto-optical rotation," *Phys. Rev. A*, vol. 62, p. 043403, Sep 2000. [Online]. Available: https://link.aps.org/doi/10.1103/PhysRevA.62.043403

[143] A. Banerjee, D. Das, and V. Natarajan, "Absolute frequency measurements of the D_1 lines in ^{39}K, ^{85}Rb, and ^{87}Rb with $\sim$ 0.1 ppb uncertainty," *EPL*, vol. 65, pp. 172–178, Jan 2004. [Online]. Available: https://doi.org/10.1209%2Fepl%2Fi2003-10069-3

[144] G. P. Barwood, P. Gill, and W. R. C. Rowley, "Frequency Measurements on Optically Narrowed Rb-Stabilised Laser Diodes at 780 nm and 795 nm," *Appl. Phys. B*, vol. 53, pp. 142–147, 1991. [Online]. Available: https://rdcu.be/b27Hu

[145] C. Glaser, F. Karlewski, J. Kluge, J. Grimmel, M. Kaiser, A. Günther, H. Hattermann, M. Krutzik, and J. Fortágh, "Absolute frequency measurement of rubidium $5S - 6P$ transitions," *Phys. Rev. A*, vol. 102, p. 012804, Jul 2020. [Online]. Available: https://link.aps.org/doi/10.1103/PhysRevA.102.012804

[146] S. Bize, Y. Sortais, M. S. Santos, C. Mandache, A. Clairon, and C. Salomon, "High-accuracy measurement of the ^{87}Rb ground-state hyperfine splitting in an atomic fountain," *EPL*, vol. 45, no. 5, pp. 558–564, Mar 1999. [Online]. Available: https://iopscience.iop.org/article/10.1209/epl/i1999-00203-9

[147] T. Udem, J. Reichert, R. Holzwarth, and T. W. Hänsch, "Absolute Optical Frequency Measurement of the Cesium D_1 Line with a Mode-Locked Laser," *Phys. Rev. Lett.*, vol. 82, pp. 3568–3571, May 1999. [Online]. Available: https://link.aps.org/doi/10.1103/PhysRevLett.82.3568

[148] R. J. Rafac and C. E. Tanner, "Measurement of the ^{133}Cs $6p^2\,P_{1/2}$ state hyperfine structure," *Phys. Rev. A*, vol. 56, pp. 1027–1030, Jul 1997. [Online]. Available: https://link.aps.org/doi/10.1103/PhysRevA.56.1027

[149] P. J. Mohr, D. B. Newell, and B. N. Taylor, "CODATA Recommended Values of the Fundamental Physical Constants: 2014," *J. Phys. Chem. Ref. Data*, vol. 45, no. 4, p. 043102, 2016. [Online]. Available: https://doi.org/10.1063/1.4954402

[150] E. Tiesinga, P. Mohr, D. Newell, and T. B., "The 2018 CODATA recommended values of the fundamental physical constants 2020," 2020. [Online]. Available: http://physics.nist.gov/constants

[151] M. Phillips, "The Effect of Nuclear Motion on Atomic Magnetic Moments," *Phys. Rev.*, vol. 76, pp. 1803–1804, Dec 1949. [Online]. Available: https://link.aps.org/doi/10.1103/PhysRev.76.180

[152] G. Audi, A. Wapstra, and C. Thibault, "The Ame2003 atomic mass evaluation: (II). Tables, graphs and references," *Nucl. Phys. A*, vol. 729, no. 1, pp. 337 – 676, 2003, The 2003 NUBASE and Atomic Mass Evaluations. [Online]. Available: http://www.sciencedirect.com/science/article/pii/S0375947403018098

[153] J. Ye, S. Swartz, P. Jungner, and J. L. Hall, "Hyperfine structure and absolute frequency of the ^{87}Rb $5P_{3/2}$ state," *Opt. Lett.*, vol. 21, no. 16, pp. 1280–1282, Aug 1996. [Online]. Available: http://ol.osa.org/abstract.cfm?URI=ol-21-16-1280

[154] E. Peik, M. Ben Dahan, I. Bouchoule, Y. Castin, and C. Salomon, "Bloch oscillations of atoms, adiabatic rapid passage, and monokinetic atomic beams," *Phys. Rev. A*, vol. 55, pp. 2989–3001, Apr 1997. [Online]. Available: https://link.aps.org/doi/10.1103/PhysRevA.55.2989

[155] P. Pillet, J. Yu, J. Djemaa, and P. Nosbaum, "Transverse magneto-optical compression of a frequency-chirping slowed cesium atomic beam," *AIP Conf. Proc.*, vol. 290, no. 1, pp. 73–75, 1993. [Online]. Available: https://aip.scitation.org/doi/abs/10.1063/1.45082

[156] E. A. Gazazyan, A. V. Papoyan, D. Sarkisyan, and A. Weis, "Laser frequency stabilization using selective reflection from a vapor cell with a half-wavelength thickness," *Laser Phys. Lett.*, vol. 4, no. 11, pp. 801–808, Nov 2007. [Online]. Available: https://doi.org/10.1002%2Flapl.200710063

[157] A. Sargsyan, G. Hakhumyan, C. Leroy, Y. Pashayan-Leroy, A. Papoyan, and D. Sarkisyan, "Hyperfine Paschen–Back regime realized in Rb nanocell," *Opt.*

Lett., vol. 37, no. 8, pp. 1379–1381, Apr 2012. [Online]. Available: http://ol.osa.org/abstract.cfm?URI=ol-37-8-1379

[158] H. Azizbekyan, S. Shmavonyan, A. Khanbekyan, M. Movsisyan, and A. Papoyan, "High-speed optical three-axis vector magnetometry based on nonlinear Hanle effect in rubidium vapor," *Opt. Eng.*, vol. 56, no. 7, pp. 1 – 7, 2017. [Online]. Available: https://doi.org/10.1117/1.OE.56.7.074104

Atomic Transitions and Population Control by Laser Frequency Scanning Speed and Magnetic Field

Abstract

In this thesis the influence of laser radiation and external uniform magnetic field on alkali-metal atomic vapor is studied. We focused on three topics. In the first part, we examined atomic population control in an M-type system to demonstrate that such systems can serve as universal three-bit logical devices. The second part concerns an experiment of atomic spectroscopy. From the fluorescence spectra recorded for stationary, transient and non-stationary interaction regimes, we were able to extract important parameter values which are the relaxation rate of the lower energy levels to the equilibrium isotropic state, the diffusion coefficient in a buffered vapor cell, and the corresponding collisional cross section. In addition, optimal temporal conditions are obtained to provide efficient control of the atomic population. In the last chapter, an interesting application of a magnetic field interacting with alkali-metal atoms is presented. Theoretically and numerically, the transitions between magnetic sublevels of alkaline atoms in the Zeeman and Paschen-Back regimes are examined. We obtained magnetic-field values canceling transitions which only depend on the fundamental physical and atomic constants. These values in the case of an appropriate experimental determination can serve as standards of magnetometry.

Keywords: *alkali vapor; spectroscopy; atomic gate; fluorescence; magnetometry*

Transitions Atomiques et Contrôle de la Population par Fréquence de Balayage Laser et Champ Magnétique

Résumé

Dans cette thèse, l'influence du rayonnement laser et du champ magnétique externe uniforme sur la vapeur atomique de métal alcalin est étudiée. Nous nous sommes concentrés sur trois sujets. Dans la première partie, nous avons examiné le contrôle de la population atomique dans un système de type M pour démontrer que de tels systèmes peuvent servir de dispositifs logiques universels à trois bits. La deuxième partie concerne une expérience de spectroscopie atomique. A partir des spectres de fluorescence enregistrés pour les régimes d'interaction stationnaires, transitoires et non stationnaires, nous avons pu extraire des valeurs de paramètres importantes qui sont le taux de relaxation des niveaux d'énergie inférieurs à l'état isotrope d'équilibre, le coefficient de diffusion dans une cellule avec gaz tampon, et la section efficace de collision correspondante. De plus, des conditions temporelles optimales sont obtenues pour fournir un contrôle efficace de la population atomique. Dans le dernier chapitre, une application intéressante d'un champ magnétique interagissant avec des atomes de métaux alcalins est présentée. Théoriquement et numériquement, les transitions entre les sous-niveaux magnétiques des atomes alcalins dans les régimes Zeeman et Paschen-Back sont examinées. Nous avons obtenu des valeurs de champ magnétique annulant les transitions qui ne dépendent que des constantes physiques et atomiques fondamentales. Ces valeurs dans le cas d'une détermination expérimentale appropriée peuvent servir d'étalons de magnétométrie.

Mots clefs : *vapeurs alcalines ; spectroscopie ; porte atomique ; fluorescence ; magnétométrie*